Surface and Tip-Enhanced Infrared Spectroscopy in Life Science: Approaching the Single-Molecule Limit

---

vorgelegt von
Emanuel PFITZNER

im Fachbereich Physik der Freien Universität Berlin eingereichte Dissertation zur Erlangung des Grades eines Doktors der Naturwissenschaften (Dr. rer. nat.)

Berlin 2018

Erster Gutachter: Prof. Dr. Joachim Heberle

Zweiter Gutachter: Prof. Dr. Paul Fumagalli

Tag der Disputation: 17. April 2019

Abstract

Infrared (IR) spectroscopy is one of the most powerful tools in life science. It delivers molecular information about structure and functionality in a non-invasive manner. However, its sensitivity and spatial resolution remain insufficient for interrogating single biomolecules. Surface and tip-enhanced spectroscopy exploit nanoscopic localization of both the probing light and the sample to address these shortcomings. Diffraction limited surface-enhanced methods offer high enhancement factors for ensembles of molecules even in aqueous environments but typically come along with high costs of production. Tip-enhanced methods provide even higher sensitivities down to hundreds of molecules and nanometric spatial resolution but are so far slow and require dry samples.

I present in this work several routes towards single-molecule IR spectroscopy using both approaches. A cost effective and reproducible method for preparation of surface-enhanced infrared absorption spectroscopy substrates was developed. These resonant disc antenna arrays allowed the microspectroscopic characterization of sub-fmol ($< 10^{-15}$ mol or $\sim 10^9$ molecules) of active membrane proteins. Their applicability to a variety of biologically important environments highlights their relevance for spectroscopy in life science. However, surface-enhanced techniques lack spatial resolution necessary for single-molecule detection and localization.

Therefore, I have designed a scattering-type scanning near-field optical microscope (*s*SNOM) for IR nanoimaging and spectroscopy. A lateral resolution of 30 nm was achieved on protein loaded membrane patches pushing the sensitivity beyond zmol ($< 10^{-21}$ mol or $\sim$600 molecules). The imaging speed was improved by a factor of 20 compared to conventional setups enabling μs time-resolved studies on biomolecules. The obvious combination of resonant substrates and *s*SNOM yielded no appreciable enhancement of sensitivity and calls for alternative strategies.

As an application to life science, whole cell nanoimaging and spectroscopy of the archeon *Halobacterium salinarum* was accomplished from which a homogeneous protein density within the cell wall could be inferred. Adapting a total internal reflection illumination scheme provided first experimental evidence towards *s*SNOM in aqueous environments. Those experiments lay the foundation for the analysis of complex membrane systems in living cells.

The *s*SNOM setup was modified to record the locally deposited heat via the anomalous Nernst effect to expand the scope of tip-enhanced methods. The domain wall within a ferromagnetic micro device was localized as a proof of principle. This method cannot only be applied to antiferromagnetic systems but bears great potential for near-field IR spectroscopy.

In conclusion, I believe that these results pave the way towards single-molecule IR spectroscopy by combining surface-, tip-enhancement and novel spectroscopic readouts.

List of Abbreviations

AFM	atomic force microscope
ANE	anomalous Nernst effect
AOI	angle of incidence
ATR	attenuated total reflection
Au	gold
bR	bacteriorhodopsin
CaF_2	calcium difluoride
CD	chemical deposition
cryo	cryogenic
DAA	disc antenna array
DDM	n-dodecyl β-D-maltoside
DFG	difference frequency generation
DFT	density functional theory
DLW	direct laser writing
DMSO	dimethylsulfoxide
DNA	deoxyribonucleic acid
DW	domain wall
EBL	electron beam lithography
E. coli	*Escherichia coli*
EF	enhancement factor
EM	electro-magnetic
EMF	electromotive force
FDTD	finite-difference time-domain
FIB	focused ion beam
FT	Fourier-transform
FTIR	Fourier-transform infrared
H. salinarum	*Halobacterium salinarum*
HeNe	helium-neon
IF	interferogram
IR	infrared
LIA	lock-in amplifier
LIL	laser interference lithography
MCT	mercury-cadmium-telluride
MFM	magnetic force microscopy
MHDA	16-mercaptohexadecanoic acid

MOKE	magneto-optical Kerr effect
NA	numerical aperture
nano-FTIR	nano-FTIR
NSL	nano-stencil lithography
***Np*SRII**	sensory rhodopsin II from *Natromonas pharaonis*
NSOM	near-field scanning optical microscope
OAP	off-axis parabolic mirror
OPD	optical path difference
PDMS	poly(dimethyliloxane)
PEM	photo-elastic modulator
PIR	plasmonic internal reflection
PM	purple membrane
PML	perfectly matched layer
PMMA	poly(methyl methacrylate)
PVD	physical vapor deposition
rcf	relative centrifugal force
RNA	ribonucleic acid
SAM	self-assembled monolayer
SEIRA	surface-enhanced infrared absorption
SEIRAS	surface-enhanced infrared absorption spectroscopy
SEM	scanning electron microscope
SERS	surface-enhanced Raman scattering
Si	silicon
S-layer	surface layer
SNOM	scanning near-field optical microscope
SNR	signal-to-noise ratio
SPM	scanning probe microscopy
***s*SNOM**	scattering-type scanning near-field optical microscope
STM	scanning tunneling microscope
TEM	transmission electron microscope
TERS	tip-enhanced Raman scattering
TIR	total internal reflection
Tris	2-amino-2-hydroxymethyl-propane-1,3-diol
TSAu	template-stripped Au
TTL	transistor-transistor-logic
QCL	quantum cascade laser
ZnSe	zinc selenide
4-MBA	4-mercaptobenzoic acid

Contents

1

Introduction

Almost all processes in living organisms depend on proteins – molecular machines, catalyzing various reactions essential for life on earth. Among these, membrane proteins take an outstanding role. They are responsible for transport of ions, solutes, organic molecules, nutrients and signals across membranes. Understanding the fundamental biological processes coupled to the proteins action is the key to design novel drugs and therapies against diseases, since most drug targets are membrane (bound) proteins.[1] This requires information about the structural arrangement of the involved proteins and cofactors on an atomic level during their catalytic action. Particularly observing single molecules offering valuable kinetic and structural information about processes even within living cells.[2,3]

1.1 Infrared Spectroscopy on Proteins

Methods like X-ray diffraction,[4] neutron diffraction[5] or transmission electron microscope (TEM)[6] can deliver 3D electron density distributions (nuclear density distributions for neutron diffraction) of highest spatial resolution beyond two Å ($2\text{x}10^{-10}$ m). Despite the effort of acquiring dynamic structural information by ultrafast crystallography[7,8] or time-resolved electron microscopy,[9,10] these methods need to be performed under hostile conditions. In contrast, infrared (IR) absorption spectroscopy can deliver structural information of proteins in a label-free manner via sensing their molecular vibrations at ambient conditions. In addition to its sensitivity towards the secondary structure of proteins,[11] protonation states of specific side groups, redox states of cofactors, hydrogen bonding of specific moieties or the local electric fields, protein samples can be studied in their native aqueous environment and with sub-ps ($<$ 10^{-15} s) temporal resolution.[12,13]

Inherent drawbacks of IR absorption spectroscopy are the low cross section ($\sigma_{abs} \sim 10^{-18}$ cm^2 per molecule)[14] and lateral resolution restricted to more than few microns.[15] The former demands for large amounts of sample (typcially 10-100 μg,[12] 50 ng for microspectroscopy[16]), the latter restricts the observation of heterogeneous structures in IR microspectroscopy to the micrometer regime. However, the above mentioned processes take place on a molecular level and, thus, require ideally lateral resolution and sensitivity allowing single-molecule detection. Two methods which can improve both the lateral resolution and sensitivity, will be introduced in the following: surface-enhanced infrared absorption spectroscopy (SEIRAS) and tip-enhanced infrared spectroscopy.

1.2 Surface-Enhanced Infrared Absorption Spectroscopy

In 1980 Hartstein et al.[17] found that thin layers of silver or gold enhance the apparent IR absorption signal of monolayers of organic compounds by a factor of ~ 20 which was later called SEIRAS (in analogy to surface-enhanced Raman scattering (SERS)). Since then, SEIRAS yielded deep insight into chemical and biological processes on surfaces as well as static and dynamic information about self-assembled monolayers (SAMs) of various organic (macro-)molecules.[18–25] Yet, single-molecule detection, as proven for SERS[26] or tip-enhanced Raman scattering (TERS)[27] was not achieved until today.

The origin of the enhancement of molecular vibrations is thought to be electro-magnetic (EM) near-fields located at the surface of the SEIRAS structures.[28] To understand this, one needs to consider the nature of EM radiation. A polychromatic light field $\mathbf{E}(\mathbf{r})$ at a spatial coordinate $\mathbf{r}$ can be described by a set of waves[29]

$$\mathbf{E}(\mathrm{r}) = \int_{-\infty}^{\infty} \tilde{\mathbf{E}}_{\mathbf{k}} e^{i\mathbf{k}\cdot\mathbf{r}} d\mathbf{k}\,. \tag{1.1}$$

with $\tilde{\mathbf{E}}_{\mathbf{k}}$ their complex amplitudes and $\mathbf{k}$ the corresponding wave vectors. For the far-field, $\mathbf{k}$ is a real quantity with magnitude $k = \sqrt{k^2{}_x + k^2{}_y + k^2{}_z} = 2\pi n/\lambda$. In this case $\mathbf{E}(\mathrm{r})$ can be described by a set of propagating plane waves. For the near-field (e.g. in z-direction) $k^2 < k^2{}_x + k^2{}_y$, which requires k_z to have an imaginary component. From Equation 1.1 one can see that this yields an exponentially decaying wave (an evanescent wave) which can not propagate in free space. Instead it is fixed to the interface at which it is generated and decays exponentially from there. The increased wave vectors $k_{x,y}$ imply the involvement of higher spatial frequencies and thereby a stronger confinement of the light field; in some cases far beyond the 'diffraction limit' (see Sec. 1.3). The near-field, however, can interact with its surrounding and can report about that interaction to the far-field. In the case of SEIRAS the near-field creating structure might be a metallic resonant antenna, a percolated metal film or dielectric structure. Within this picture it can be understood that the degree of localization determines the strength of the vibrational enhancement (see Sec. 2.2).[30]

A side effect of the evanescent waves localization at an interface is, that only molecules in the close vicinity (typically one to tens of nm) are sensed by the near-field.[31,32] Although the enhanced light confinement and the enhanced sensitivity towards monolayers of small molecules, it still copes with the disadvantage of spurious lateral resolution. The following section will introduce an alternative method to approach this challenge.

1.3 Tip-Enhanced Infrared Spectroscopy

The resolving power of a microscope is inherently limited by the wave properties of the used radiation which can be photons, electrons, atoms or any other particle. For an optical microscopy, Ernst Abbe put forward a general criterion which determines the maximal achievable lateral resolution Δ[33]

$$\Delta x_i = \frac{\lambda}{2n\sin(\alpha)}. \tag{1.2}$$

n is the index of refraction of the material between the lens and the sample, α the half angle of acceptance of the used objective and λ the wavelength of the used radiation. For air ($n = 1$) and a maximum angle of acceptance of 90° this yields a lateral resolution in the order of $\Delta x_i = \lambda/2$.

An alternative description arises from combining Heisenberg's uncertainty principle and the decomposition of any electric field above (Eqn. 1.1).[34] Heisenberg's uncertainty principle relates spatial uncertainty Δx_i with a known momentum $p_i = hk_i/2\pi$ by

$$\Delta x_i |p_i| \geqslant \frac{h}{2\pi}. \tag{1.3}$$

Using that relationship, the spatial uncertainty of a photon can be approximated by

$$\Delta x_i \geqslant \frac{1}{|k_i|} = \frac{\lambda}{2\pi n}. \tag{1.4}$$

One can readily see that the 'diffraction-limit' scales linearly with the wavelength. In particular IR microspectroscopy suffers from this fundamental circumstance and limits the lateral resolution to several microns.[15] This hinders the investigation of molecular processes in life science which typically requires a resolution beyond the length scale of cells, i.e. in the sub-micron regime.

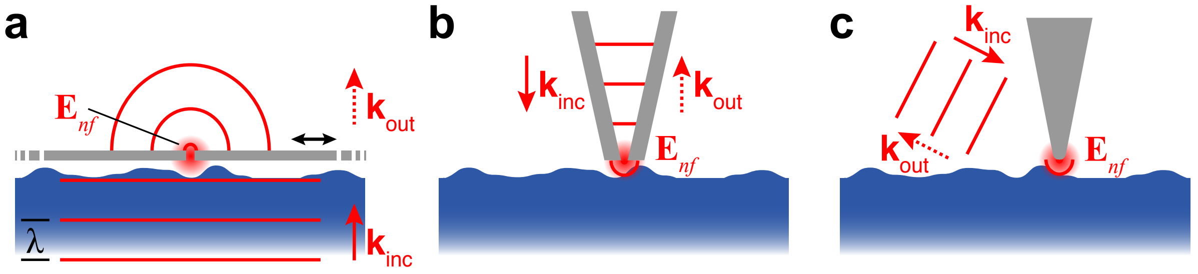

Figure 1.1 **(a)** Ultramicroscope suggested by E. H. Synge (1928).[35] **(b)** Schematic setup of a typical aperture SNOM or **(c)** *s*SNOM.

E.H. Synge was the first to conceptually suggest an 'ultra-microscope' in 1928 (Fig. 1.1a).[35] A sub-wavelength aperture (gray) should be scanned by the help of 'piezo-electricity' across a sample (blue) in order to create a raster scanned image with a lateral resolution beyond the 'diffraction-limit'.[36] It took almost 50 years until such a SNOM could be experimentally demonstrated at GHz frequencies[37] and another ten years to transfer this knowledge to the visible regime.[38] Pohl et al. could demonstrate a lateral resolution of $\lambda/20$ by scanning an aluminum or silver coated quartz rod, carrying a sub-wavelength aperture on its end (Fig. 1.1b), over a lithographic grating sample. Replacing the scanned sub-wavelength aperture by a sub-wavelength scattering probe (Fig. 1.1c), easily pushed the lateral resolution to the nm ($10^{-}9$ m) regime which corresponds to $\sim \lambda/200$.[39,40]

The last two decades witnessed a rapid evolution of various SNOMs utilizing an ultra broad range of radiation from the visible to the THz. The bottom illumination of Zenhausern et al.[39] was replaced by a side illumination scheme. A resolution of $\lambda/3000$ using THz radiation was reported 2008.[41] Recently, Mastel et al. demonstrated a resolution of 5 nm with light of 10 μm wavelength using ultrasharp tungsten tips with a radius of 3 nm.[42]

Notably, IR *s*SNOM could be successfully transferred to life science.[43–47] In selected experiments the lateral resolution of tens of nm and sensitivity was sufficient to detect single complexes of ferritin,[44] hundreds of individual membrane proteins[45] and thousands of single molecules of 16-mercaptohexadecanoic acid (MHDA) constituted in a SAM.[14] Particularly, the ability to record IR spectra over the whole mid-IR regime (500 cm^{-1} - 4000 cm^{-1} or 2.5 μm - 20 μm) of a nanoscopic spot of $\sim$ 10x10x10 nm^3 is appealing due to its wealth of chemical information encoded in these spectra. However, attempts to observe biological samples, especially single molecules, in an aqueous environment still remain a major challenge.[48]

1.4 Scope of This Work

The aim of this work is to elaborate new techniques, which pave the way to enable single molecule vibrational spectroscopy on proteins – preferably in aqueous environments. As outlined above, I will present and test two concepts: enhancing vibrational modes by SEIRAS with sensitivity for fmol (10^{-15}) of proteins in aqueous environments. My home-built *s*SNOM with imaging and nanospectroscopy capability will be discussed on exemplary biological samples (e.g. whole archeal cells, Fig. 1.2a). To ultimately enhance the EM field, a combination of both, substrate enhancement and tip enhancement, will be evaluated (Fig. 1.2b).

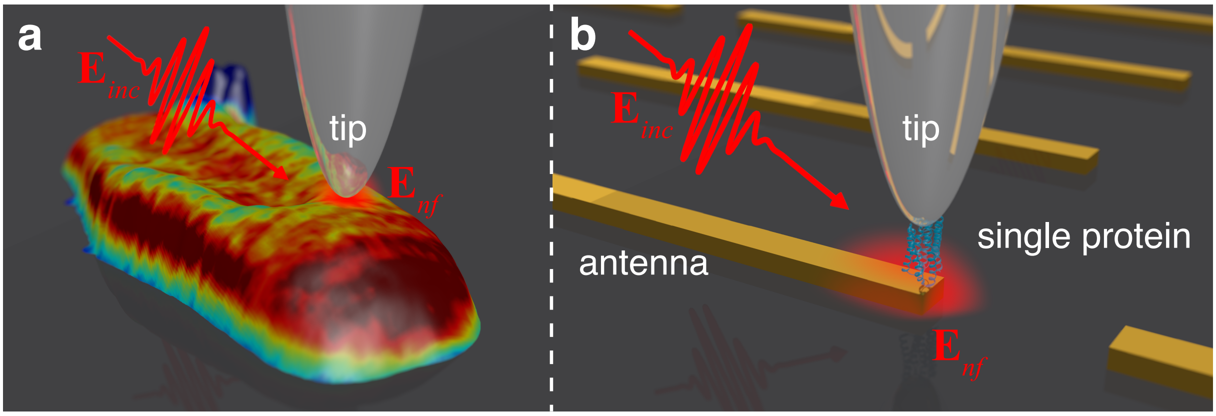

Figure 1.2 **(a)** Near-field IR spectroscopy of a single archeal cell. **(b)** Antenna enhanced near-field IR spectroscopy of a single protein.

Finally, I will introduce a conceptually new method for imaging magnetic domains in (anti)ferromagnetic thin films. Besides its great potential in magnetic microscopy, this method might be applicable as alternative sensing scheme for near-field vibrational nanospectroscopy.

2

Methods and Theory

2.1 Vibrational Spectroscopy

Every material is composed of molecules which themselves consist of atoms bound to each other in one, for each molecule unique configuration. Each of these configurations leads to a unique set of vibrational modes. Vibrational spectroscopy takes advantage of exciting these modes and, thus, yields molecular specific spectral fingerprints. Two widely used techniques are

- Infrared absorption spectroscopy
- Raman Spectroscopy

of which the former relies on absorption of IR photons whereas the latter one on inelastic scattering of photons typically in the ultraviolet to visible range.

2.1.1 The Harmonic Oscillator

In a classical picture one can imagine the atoms being point masses m_i connected via springs with spring constants k_{ij}. In the simplest case of a diatomic molecule, the equation of motion can be solved by the one dimensional harmonic oscillator (Fig. 2.1a, red trace). For an adequate description, the quantum mechanical time-independent Schrödinger's equation for a harmonic oscillator needs to be solved

$$\widehat{H}\Psi \;=\; \left(\frac{\widehat{p}^2}{2m} + V(r)\right)\Psi \;=\; \frac{\hbar^2}{2\mu}\frac{d^2\Psi}{dr^2} + \frac{k_{12}}{\mu}\frac{1}{2}(r-r_0)^2\Psi \;=\; E\Psi \tag{2.1}$$

with $\widehat{H}$ the Hamiltonian, $\widehat{p}$ the momentum operator, $V(r)$ the potential energy, r the two atoms distance, $\mu = \frac{m_1 m_2}{m_1+m_2}$ the reduced mass of the two atoms, k_{12} the bond strength and Ψ the systems wave function with its corresponding energy E. Eigenvalues for the energy are

$$E = \left(v + \frac{1}{2}\right)\hbar\omega \tag{2.2}$$

where v is the vibrational quantum number and $\omega = \sqrt{\frac{k_{12}}{\mu}}$ the corresponding angular frequency. A transition from one state to another is only allowed for $\Delta v = \pm 1$ typical for dipole transitions. It is common in vibrational spectroscopy to express the frequency ω as wavenumber $\tilde{\nu}$ in units of cm^{-1}

$$\tilde{\nu} = \frac{1}{2\pi c}\sqrt{\frac{k_{12}}{\mu}}. \tag{2.3}$$

Thus, knowing k_{12} for a diatomic molecule the frequency of its molecular stretching vibration within the harmonic approximation can be determined.

An empirical energy vs core-core distance dependency was given by Morse (cf. Fig. 2.1a, black trace)

$$V(r) = V_0(1 - e^{-a(r-r_0)})^2 \tag{2.4}$$

with V_0 the dissociation energy, a the steepness of the potential and r_0 the resting core-core-distance. Solving Schrödinger's equation with this potential energy yields the energy eigenvalues

$$E = (v + \frac{1}{2})\hbar\omega - (v + \frac{1}{2})^2 \frac{\hbar^2\omega^2}{4V_0}. \tag{2.5}$$

Here the angular frequency becomes $\omega = a\sqrt{2V_0/\mu}$. The energy difference between two vibrational levels is not constant anymore and decreases with increasing vibrational quantum number eventually leading to dissociation of the molecule.

The time-independent Schrödinger equation becomes analytically non-solvable for molecules which consist of more than two atoms. Still, one can state that a N-atomic molecule exhibits $3N$ degrees of freedom (three for each atom) of which three are translation and three rotation (2 for linear molecules) of the whole molecule. Since translation and rotation of the whole molecule do not describe an vibration, $3N - 6$ vibrational degrees of freedom (3N-5 for linear molecules) are left. These degrees of freedom translate into the same number of vibrational normal modes with normal coordinates Q_i. Figure 2.1b illustrates four exemplary modes. Here, conventionally ν describes a stretching (ν_s symmetric, ν_{as} anti-symmetric), δ deformation (e.g. bending) and ω wagging vibrations.

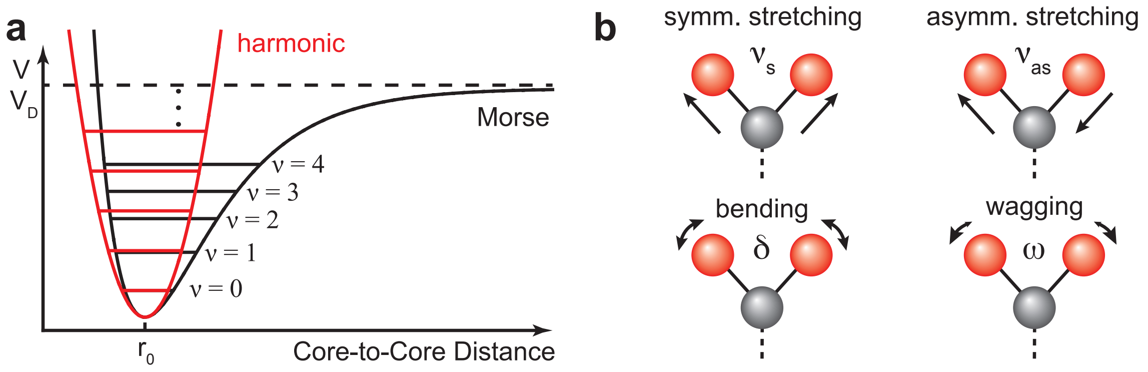

Figure 2.1 (a) 1-dimensional harmonic potential as approximation for a core-to-core distance Morse potential (V_0: dissociation Energy, r_0 mean core-to-core distance). Vibrational energy levels are indicated by vertical lines. **(b)** Exemplary molecular vibrational modes: ν_s symmetric stretching, ν_a asymmetric stretching, δ deformation and ω wagging.

Exciting a molecular vibration by absorption of a photon with energy $E_{photon} = \hbar\omega = \Delta E$ can be described by a transition between the two vibrational states ψ_i and ψ_j. The probability of this transition is proportional to $|\mathbf{M}_{i,j} \cdot \mathbf{E}|^2$ where $\mathbf{M}_{i,j} = \int\int \psi_i(\mathbf{x})^* \, \mu \, \psi_j(\mathbf{x}')dx^3dx'^3$ is the transition dipole moment and μ the dipole operator. Within the harmonic approximation μ can be expanded by a Taylor series as $\mu = \mu_0 + \sum_{i=1}^{3N-6} \frac{\partial \mu}{\partial Q_i} Q_i$. This results in an important implication for a vibrational transition to be IR active: the dipole moment needs to change along the normal coordinate Q_i. Furthermore it can be shown that $\Delta v = i - j = \pm 1$ within the harmonic approximation. That implies that no harmonics can be observed in an IR absorption spectrum.

2.1.2 Vibrational Modes in Biological Systems

The major constituents of living cells or tissue are organic polymers (proteins, ribonucleic acid (RNA), deoxyribonucleic acid (DNA), sugars etc.) in an aqueous environment which are separated into compartments by lipid bilayers. Proteins act as nanomachines fulfilling various tasks for each cells living cycle. Their repeating structural elements are a linear sequence of amino acids of which 20 naturally exist. These are linked via peptide bonds. The amino acid sequence is called primary structure which determines the 3D organization of the natively folded polypeptide (secondary and tertiary structure) upon interaction with water (for water-soluble proteins) or the lipid molecules of the biomembrane (for integral membrane proteins). The peptides themselves as well as their 3D arrangement give rise to several specific absorption bands in the infrared spectral range which are indicated in Figure 2.2 (red trace): amide A (ν(N-H)), amide B (Fermi-resonance between ν(N-H) of amide A and amide II), amide I (ν(C=O)), amide II (out-of-phase δ(N-H) & ν(C-N)) and amide III (in-phase δ(N-H) & ν(C-N)).[12] In a typical 3D fold of a protein, most carbonyls are hydrogen bonded to the amines which result in different secondary structure patterns like α-helices or (anti-)parallel β sheets. Due to the high sensitivity of the ν(C=O) towards its environment, the amide I is most indicative to the proteins secondary structure. The native aqueous environment adds strong absorption bands at similar frequencies (Fig. 2.2, red line) to the spectrum which makes sophisticated techniques necessary for IR spectroscopy on proteins.

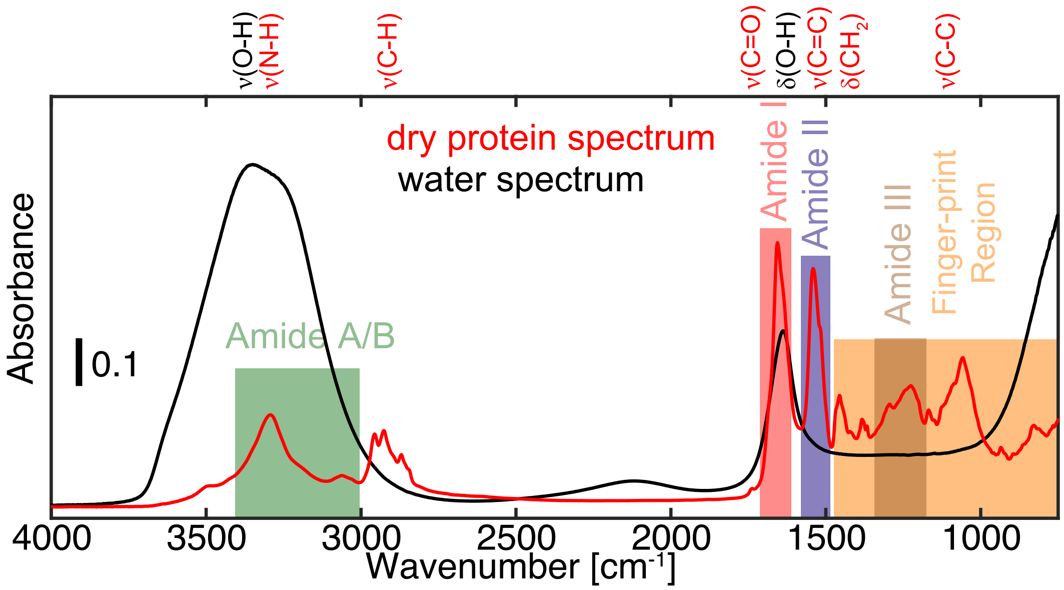

Figure 2.2 Representative ATR-FTIR absorption spectra of liquid water (black) and a dried protein film (red). Relevant vibrational modes of biologically systems are indicated above the spectrum.

2.1.3 The Absorbance

The absorbance A of a material is defined as $A = -\log_{10}\left(\frac{I}{I_0}\right)$ where I denotes the intensity transmitted through the sample and I_0 the intensity of the source without the sample of interest in the beam path. In such experiments care must be taken that only absorption processes contribute to I (i.e. excluding luminescence, scattering, interference etc.). Analogously to the transmission experiment, an absorbance can be defined in a reflection experiment[49]

$$A = -\log_{10}\left(\frac{R}{R_0}\right) \tag{2.6}$$

where the reflectance R of the sample after a modification is referenced to the reflectance R_0 of the latter before this treatment.

2.1.4 Fourier-Transform Infrared Absorption Spectroscopy

FTIR absorption spectroscopy is a versatile tool for characterization and identification of matter in all states in a label-free manner. In the following the working principle and core features of FTIR will be discussed as it is of fundamental importance for the understanding of the construction of an interferometric spectrometer (see Sec. 3.5) and details of the FTIR spectra as presented in this thesis.

FTIR spectroscopy is a technique relying on interference of light. A typical schematic setup of a symmetric Michelson interferometer is shown in Figure 2.3a. The emission of a blackbody radiator (globar, silicon carbide rod heated to ~ 1500 K) is split by a beamsplitter and send to a static and a movable mirror, respectively. The reflected beams are recombined at the beamsplitter and send to an detector. The movable mirror can be linearly displaced to introduce different optical path difference (OPD) – or retardations – $z = 2d$ between the two rays. In a simplified situation the source emits only one wavelength λ with intensity I_λ which constructively or destructively interfere for progressive retardations shown in Figure 2.3b. It is to be noted that detectors for visible to mid-IR can only measure the intensity $\tilde{I} \propto |E|^2$ of light at bandwidths up to GHz which acts as a lowpass-filter and disables phase detection. $\tilde{I}(z)$ for continuous retardation z can be written as

$$\tilde{I}_{mono}(z) = \frac{I_\lambda}{2}\left(1 + \cos(2\pi \frac{z}{\lambda})\right). \tag{2.7}$$

which can be generalized for polychromatic sources with a spectral intensity of $I(\tilde{\nu})$ by integration over all frequencies to

$$\tilde{I}(z) = \int_{-\infty}^{\infty} \frac{I(\tilde{\nu})}{2}\left(1 + \cos(2\pi z\tilde{\nu})\right) d\tilde{\nu}. \tag{2.8}$$

with $\tilde{\nu}$ being the wavenumber. Equation 2.8 is called a cosine Fourier-transform (FT) and applying the inverse FT yields:

$$I(\tilde{\nu}) = \int_{-\infty}^{\infty} \frac{\tilde{I}(z)}{2}\left(1 + \cos(2\pi z\tilde{\nu})\right) dz. \tag{2.9}$$

In the following the constant term will be neglected such that the spectrum $B(\tilde{\nu})$ can be computed from the modulated signal $S(z)$ – or interferogram (IF) – measured at the detector by

$$B(\tilde{\nu}) = \int_{-\infty}^{\infty} S(z)\cos(2\pi z\tilde{\nu})dz. \tag{2.10}$$

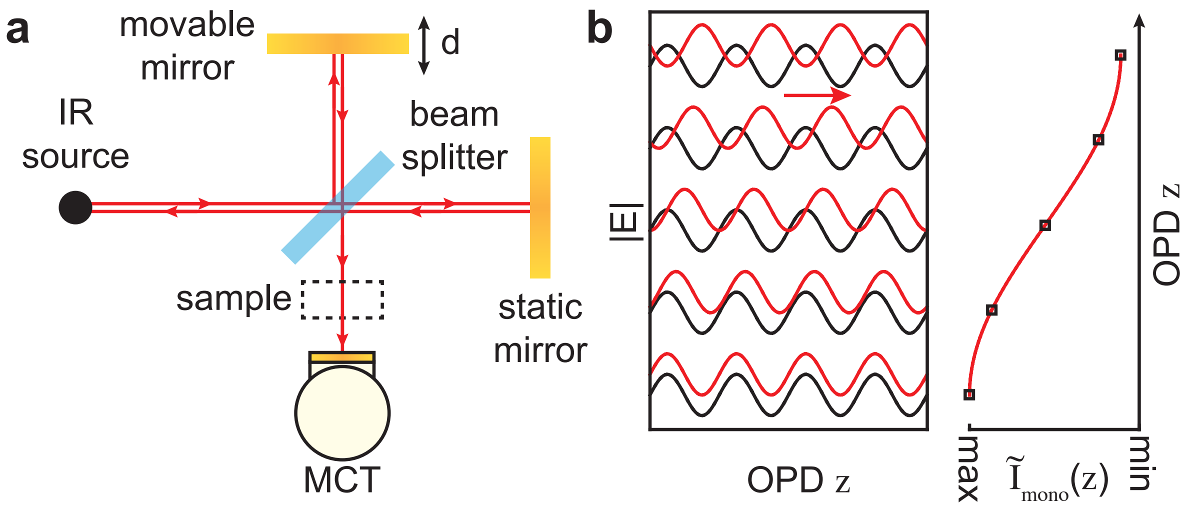

Figure 2.3 **(a)** Schematic setup of an FTIR spectrometer using an MCT detector. **(b)** A monochromatic wave interfering with itself shifted by varying OPDs z.

One can easily see from equation 2.10 that an accurate spectrum $B(\tilde{\nu})$ can only be calculated if the integration is performed from $-\infty$ to ∞. In a real experiment the traveling range of the mirror is limited to $2d_{max} = z_{max}$ which one can consider by introducing a retardation-dependent boxcar function $D_{z_{max}}(z) = \Theta(z + z_{max})\Theta(-z + z_{max})$ with $\Theta(z)$ the Heaviside step function.

$$B(\tilde{\nu}) = \int_{-\infty}^{\infty} D_{z_{max}}(z)S(z)\cos(2\pi z\tilde{\nu})dz. \tag{2.11}$$

Finite Retardation The consequences of and finite retardation length becomes obvious if we take spectra $B(\tilde{\nu})$ with a finite spectral composition: let us consider the case where $B(\tilde{\nu})$ consists of only a single spectral component $B_0\delta(\tilde{\nu} - \tilde{\nu}_0)$, with δ the Dirac delta distribution. Performing a FT, multiplying with a boxcar function and inversely applying the FT yields a sinc-function as shown in Figure 2.4a which introduces broadening and artificial side lobes to spectral sharp features. Thus, the spectral resolution $\Delta\tilde{\nu}$ is limited by the maximum retardation z_{max} by $\Delta\tilde{\nu} = \frac{1}{z_{max}}$ (Fig. 2.4b). The lower z_{max} is chosen the broader each spectral feature becomes.

Apodization The folding theorem for FTs states that a multiplication of two functions in the Fourier space is the same as folding them in real space. This theorem can be readily applied here to easily understand qualitatively the effect of the finite IF length: the real spectrum gets folded with the sinc function. To minimize artificial band shapes and side lobes introduced by the finite IF length one typically multiplies the IF with a so called apodization function $w(z)$ which smoothly decays the IF to 0 at either end. One commonly used apodization function which will be used in this work is the empirically derived 4-term Blackman-Harris apodization which aims for minimization of the sidelobes (see Sec. A.7). Figure 2.4 **(c)** displays the FT of this apodization function. Indeed the sidelobes are drastically reduced which is accompanied by a decreased spectral resolution.

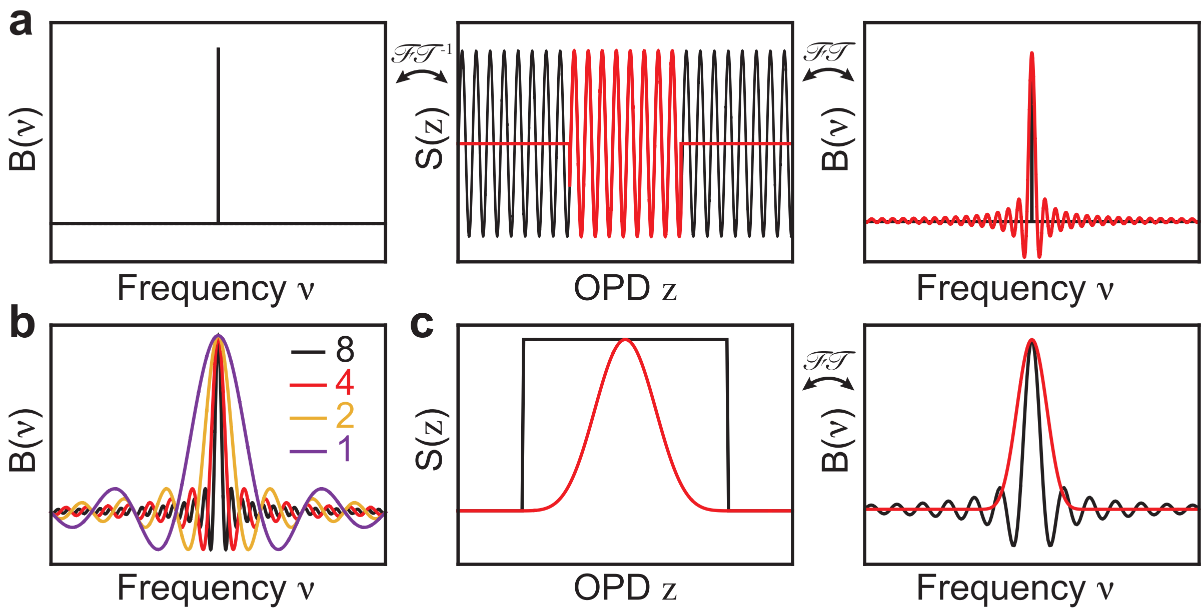

Figure 2.4 **(a)** Spectrum comprising one single frequency (left panel) along with its inverse FT (middle panel, black). After multiplying with a boxcar function of finite length (middle panel, red) and FT (right panel, red) the Dirac delta distribution is convolved by a sinc function. **(b)** Dirac delta distributed spectra of decreasing bandwidths in terms of multiples of z_{max}. **(c)** 4-term Blackman-Harris window function (left panel, red) compared to a boxcar window (left panel, black) and their FT (right panel).

Effect of Discrete Sampling Intervals Up to now the IF was assumed to be continuously acquired. In a real experimental setup the IF needs to be sampled with a finite number of equidistantly spaced points. To achieve a constant spacing a visible laser is coupled parallel to the IR beam and detected by a separate photodiode. While the traveling mirror moves, a sinusoidal interference pattern of the visible laser is detected (Fig. 2.5a). The zero-crossings of the laser interference mark positions of equal distance of $\Delta = \lambda/2$. Thus, the zero-crossings are used as positions to sample the simultaneously acquired IR IF. Nyquists theorem tells that discretization of the IF has the implication that the highest detectable wavenumber will be limited to $\tilde{\nu}_{max} = 1/2\Delta$ which is 15802.38 cm^{-1} (in air) if the red line of a helium-neon (HeNe) laser is used.

Zerofilling By both the finite sampling length and the discrete sampling intervals the number of points in the resulting spectrum is limited and it might look pixelated. A elegant way to interpolate the spectrum is to simply append a set of zeros to the apodized IF before FT. By this procedure no information is added but the resultant spectrum looks smoother. One can imagine this procedure as interpolation of the spectrum by higher frequency cosine terms. Typically the amount of zerofilling is given by the zerofilling factor which determines the number of points of the IF after zerofilling compared to the raw IF.

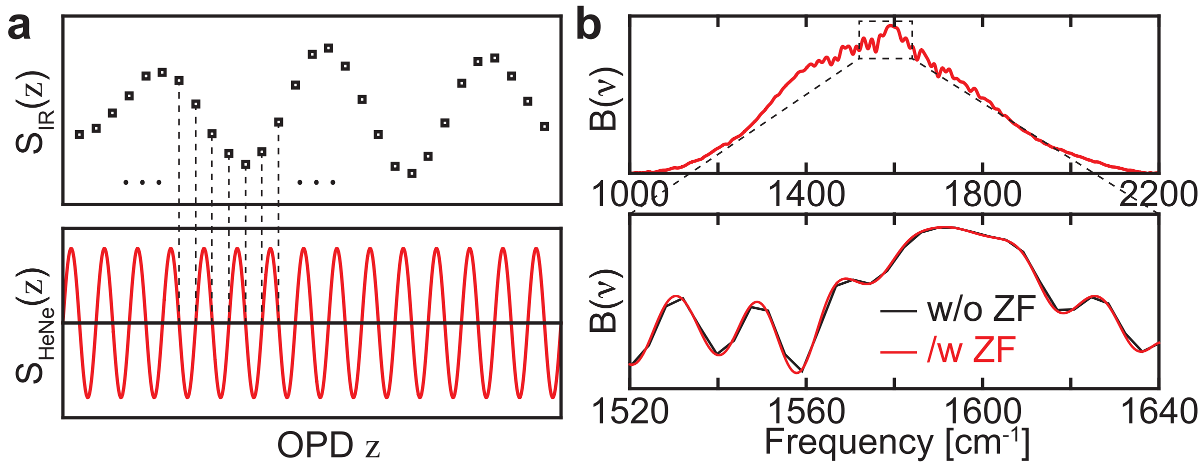

Figure 2.5 (a) IR and HeNe-IF. The IR IF is sampled at the inflection points (zero-crossings) of the HeNe-IF. **(b)** Resulting spectrum after FT with and without zerofilling (ZF, zerofilling factor 8).

Phase Correction By imperfections in the beamsplitter characteristics, detector response, electronic filters etc. but also by variation of the absolute sampling position of the IR IF a non-zero phase can be introduced in the interferogram which results in a spectrum after Fourier-transform that is in general a complex quantity (Fig. 2.6a). As depicted in Fig. 2.6 the phase typically varies slowly with frequency. To compensate for these imperfections it is a common practice to perform phase-correction on the spectra or interferograms. This section will follow the procedure proposed by Mertz.[50] The original IF is apodized by a much narrower window function as required, thus, yielding a smooth version of the complex spectrum $S_{\mathrm{PC}}(\tilde{\nu}) = Abs\{S_{\mathrm{PC}}(\tilde{\nu})\}e^{iArg\{S_{PC}(\tilde{\nu})\}}$. From the low resolution spectrum the phase $\Phi_{\mathrm{PC}} = Arg\{S_{\mathrm{PC}}(\tilde{\nu})\}$ can be easily calculated. This phase Φ_{PC} is then substracted from the spectrally high resolved spectrum $S(\tilde{\nu})$ (i.e. unapodized, cf. Fig. 2.6b, lower panel). Inverse FT yields a phase corrected version of the original IF (Fig. 2.6b, upper panel). When comparing the phase-corrected to the original IF one important detail appears: the formerly asymmetric IF becomes symmetric. This will be used in the data processing to align individual IFs and to eliminate phase baselines in Section 4.2. However, care

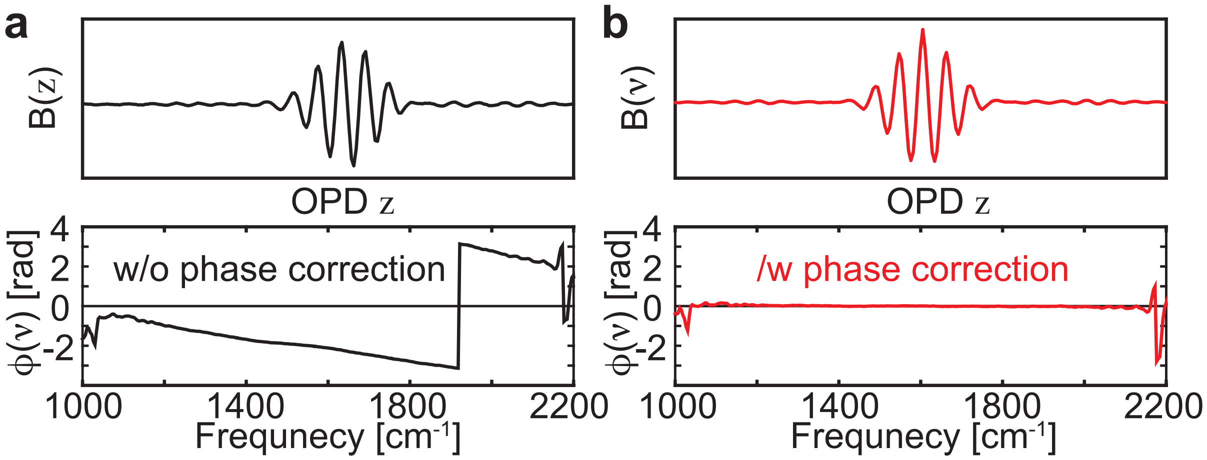

Figure 2.6 IF and phase spectrum before **(a)** and after **(b)** phase correction following the Mertz method.[50]

must be taken to chose the resolution of the phase correction spectrum sufficiently low, not to reduce any meaningful vibrational information encoded in the high resolution phase spectrum.

Asymmetric complex IF and its FT The following sections will show how FTIR can be combined with near-field nanospectroscopy (see Sec. 2.3.2 & Sec. 3.5.2). Typically an asymmetric interferometer is used in which the vibrational information of the sample is stored only in one side of the IF in the form of the free induction decay of the excited oscillators.[46,51] Thus, it is sufficient to use only the sample related side of the IF for reconstruction of the spectrum. This is done via an asymmetric apodization function which decays within the center burst to the reference side of the IF and according to the full spectral length on the sample side. It is important to apply first a phase correction to properly find the IF centerburst.

The discrete FT will yield a spectrum, which contains useful information up to its Nyquist frequency $\tilde{\nu}_\mathrm{s}/2$ (half the sampling frequency) and would appear mirrored and complex conjugated at frequencies $\tilde{\nu}_\mathrm{max}/2 < \tilde{\nu} < \tilde{\nu}_\mathrm{s}$. In the later presented scheme the interferogram is recorded as the complex output of the lock-in amplifier (LIA). Due to phase noise, the FT of it will not be symmetric with respect to its complex conjugate as just stated. However, since the interferogram is a result of the detection of photons it is ideally a real quantity. For real time-domain signals $x(t) \in \mathbb{R}$ one can state

$$\begin{aligned} \mathfrak{Re}\left\{\mathcal{F}(x(t))(\omega)\right\} &= \quad \mathfrak{Re}\left\{\mathcal{F}(x(t))(-\omega)\right\} \\ \mathfrak{Im}\left\{\mathcal{F}(x(t))(\omega)\right\} &= -\mathfrak{Im}\left\{\mathcal{F}(x(t))(-\omega)\right\}. \end{aligned} \tag{2.12}$$

To make the resulting spectrum symmetric and, thus, origin of a real quantity, it can be averaged with its mirrored and complex conjugated spectrum. This procedure cancels noise introduced via the phase during acquisition of the interferogram and will be applied to all spectra recorded with the nano-FTIR method (see Sec. 2.3.2, Sec. 3.5 & Sec. 4.2).

2.2 Surface-Enhanced Infrared Absorption Spectroscopy (SEIRAS)

Two mechanisms are to be discussed responsible for the absorbance signal enhancement SEIRAS: the electromagnetic and the chemical mechanism.

The former relies on the interaction of the metal film with closeby molecules via the optical near-field induced by the incident radiation. The reflected spectrum of the gold film is modulated by the oscillators situated in close vicinity of the metal surface and, thus, enhanced. The near-field decays rapidly in the order of nanometers[52,53] to tens of nanometers away from the surface.[31,32,54] Various studies in which the experiments correlated well with numerical simulations suggest the electromagnetic mechanism being dominant in the signal enhancement.[31,49,54–57] Figure 2.7c shows an exemplary electric field distribution $\frac{|\mathbf{E}_{\text{Loc}}|}{|\mathbf{E_0}|}$ at an wavelength of 5 μm calculated by finite-difference time-domain (FDTD) (see 2.2.4). Since the absorption is proportional to $\frac{|\mathbf{E}_{\text{Loc}}|}{|\mathbf{E_0}|}^2$ and, thus, to the enhancement factor (EF), a relative field enhancement of ~ 25 corresponds well with the typically experienced EFs in the order of 100.[58]

The chemical mechanism is far less clear. Generally a chemical bond between a molecule and the metal film (e.g. sulfur-gold bond) changes the electronic structure and thereby the transition-dipole-moment of the adsorbed molecule.[59] The energy of the metals Fermi level and molecular orbits need to match for an enhancement to occur. This could explain enhancement in rare cases in the order of 10.[60]

Taking a closer look on the electromagnetic enhancement, one can describe antenna or particle as a resonator (cavity) which supports electromagnetic cavity modes. Major properties of such a cavity are their quality factor Q and their effective mode volume V_{eff}. Q corresponds to the spectral mode energy density of the cavity whereas V_{eff} relates to its spatial mode energy density. For metallic cavities one can derive the following dependency[30]

$$\frac{|\mathbf{E}_{\text{Loc}}|}{|\mathbf{E_0}|}^2 \propto \frac{Q^2}{V_{\text{eff}}} \,. \tag{2.13}$$

It is evident from that relationship that by confining the incident radiation more and more beyond $\lambda/2\pi n$, the enhancement increases. Additionally we can see that increasing Q, decreasing the spectral bandwidth of the cavity mode, also increases the EF.

2.2.1 Experimental Realization of SEIRAS

Randomly shaped, percolated metal films Island structure like metal films were found to yield an EF in the order of 10 - 50.[18] These films can be created by physical vapor deposition (PVD) (e.g. Ar sputtering, resistive heating or eletron beam assisted heating) of noble metals on a variety of substrates (e.g. CaF_2, BaF_2, ZnSe, Si or Ge)[17,61–63] or by electroless deposition or chemical deposition (CD) of gold on Si[64] or ZnSe[65] prisms. Although especially the latter method involves relatively cheap chemical compounds for preparation its success strongly relies on environmental factors as well the experimenter's skills.[61,66] Topographical investigation of these surfaces by atomic force microscope (AFM) or scanning electron microscope (SEM) have shown the morphology to be randomly oriented and shaped metal islands instead of a continuous film (Fig. 2.7a).[60,63,66] For accessing the enhancing metal film even when exposed to solution, the Kretschmann geometry is commonly used in which the percolated metal film is deposited on one side of an IR transparent prism at which the IR beam is totally reflected (Fig. 2.7b).

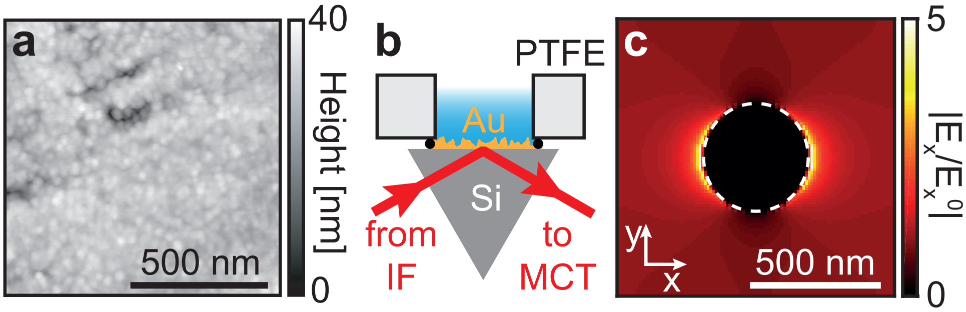

Figure 2.7 (a) AFM topography of a chemically electroless deposited gold film on a Si prism (gold film prepared by Hirofumi Seki, AFM topography acquired by Katerina Kanevche, AG Heberle, Freie Universität Berlin, Germany). **(b)** Sketch of the experimentally used geometry for ATR-based SEIRAS. **(c)** Simulated E-field distribution at the waist of a perfect metallic ellipsoid (at $\sim$1800 cm^{-1}). White dashed line indicates outlines.

Engineered Resonant Metal Antennas To optimize the EF and its reproducibility and to gain insight into the mechanisms of enhancement, much interest was drawn in the past decade to designing nanometer to micron-sized metallic structures by means of engineering their shape and arrangement.[28,67] These bar-like antennas (Fig. 2.8a), slits, or gratings act as antennas or apertures which show dipolar resonances in the IR.[28] The resonance frequency of these antennas can be predicted by a simple scaling law linear in the antennas length.[68,69] The coupling of the antennas to incident radiation and their enhancement factor of vibrational fingerprints can further be tuned by the geometric properties of the single antennas[70] as well as their arrangement in arrays.[69,71] To accurately control the dimensions of these metal structures at nanometer precision electron beam lithography (EBL),[67] focused ion beam (FIB) milling,[72] laser interference lithography (LIL),[73] direct laser writing (DLW),[74] or nano-stencil lithography (NSL)[75] are used. Since most of these methods are not paralellizable and the area on which structures can be produced is effectively limited, they are usually studied with a FTIR-microscope. Still, Adato et al. showed a similar approach to interrogate the antennas spectroscopically while being immersed in aqueous environment.[49] This was introduced as plasmonic internal reflection (PIR) in analogy to attenuated total reflection (ATR) (Fig. 2.8b, cf. 3.2). The resulting array of antennas yield EFs in the order of $10^3 - 10^5$ with high reproducibility and sensitivities down to tens of attograms of a small organic molecules.[28]

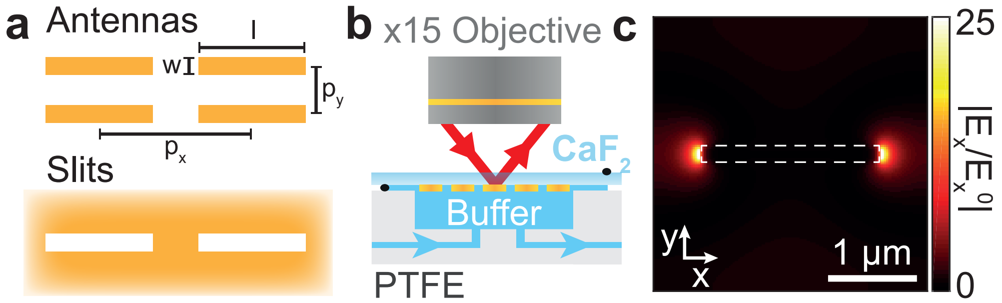

Figure 2.8 (a) Sketch of bar-like gold antennas. **(b)** Sketch of the experimentally used PIR setup. (c) Simulated E-field distribution 5 nm above a perfect metallic bar antenna (at resonance, ~1800 cm^{-1}). White dashed line indicates outlines.

2.2.2 The Enhancement Factor

To quantify and compare different surface-enhanced spectroscopic methods, it is common practice to give an enhancement factor (EF). Although there are different ways of estimating this quantity they all rely on a common method: the apparent absorbance signal per molecule $\tilde{A}_{\text{NF}}$ in the surface-enhanced (near-field) experiment is compared to the apparent absorbance per molecule $\tilde{A}_{\text{FF}}$ in a non-enhanced (far-field) experiment:[28,59]

$$\text{EF} = \frac{\tilde{A}_{\text{NF}}}{\tilde{A}_{\text{FF}}}\alpha \tag{2.14}$$

In some studies[28,49,76] an additional factor α is introduced which compensates for e.g. only molecules at the electromagnetic hot spots contributing to $\tilde{A}_{\text{NF}}$ thereby overestimating the EF. In this work all molecules are assumed to contribute equally to the apparent enhanced absorbance.

2.2.3 Surface Selection Rule

As discussed above (Sec. 2.1.1) the absorption of IR photons can be quantum mechanically described by a vibrational transition. This probability A is proportional to

$$A \propto |\mathbf{E} \cdot \partial \boldsymbol{\mu}/\partial Q_i|^2 = |\mathbf{E}|^2 \cdot |\partial \mu/\partial Q_i|^2 |\cos\varphi|^2 \tag{2.15}$$

where **E** denotes the electric field vector, $\partial \boldsymbol{\mu}/\partial Q_i$ the partial derivative of the dipole moment along the individual vibrations normal coordinate and φ the angle between both vectors. Consequently, vibrations whose transition dipole moment is parallel to the E-field are enhanced whereas those perpendicular are not observed at all. Since the E-field vector is always pointing in normal direction of conductive surfaces, vibrational modes with their transition dipole moment normal to the surface are enhanced and those perpendicular do not appear in the absorption spectrum.

2.2.4 Theoretical Modeling of Near-Field Enhancement

Coupled Harmonic Oscillators and Fano Resonances Depending on the spectral characteristics of the enhancing substrate, the band shapes of the adsorbed molecules can change from a absorptive Lorentzian lineshape to a Fano-type lineshape.[28] The spectral separation, defined as $\omega_{vib}/\omega_{res}$ where ω_{vib} is the frequency of the narrow vibrational mode and ω_{res} the frequency of the broad antenna resonance, is the most influencing one. Depending on the spectral separation and the geometry of the metal structures the lineshape can change from absorptive over asymmetric to anti-absorptive lineshapes.[59,77,78] Giannini et al. presented a parameter free quantum mechanical description of such spectra assuming a discrete state (the molecular vibration) coupled to a continuous state (the antenna resonance) leading to a coupled quasi-continuous state.[77] Figure 2.9 displays a generic vibrational band (centered at ω_{vib} = 1730 cm^{-1} with width Γ_{vib} 10 cm^{-1}) coupled to a antennas resonance (centered at ω_{res} = 1230 ... 2230 cm^{-1} with width Γ_{res} 200 cm^{-1}). The relative reflectance shows the typical asymmetric Fano-type lineshape seen in experiments where linear gold antennas with relatively sharp resonances (Q ~10) are employed.[78] As the spectral separation increases from $\omega_{vib}/\omega_{res} < 1$ the asymmetry first decreases and the line reaches complete symmetric lineshape when $\omega_{vib}/\omega_{res} = 1$. For $\omega_{vib}/\omega_{res} > 1$ the asymmetry increases again but is inverted along the spectral axis.

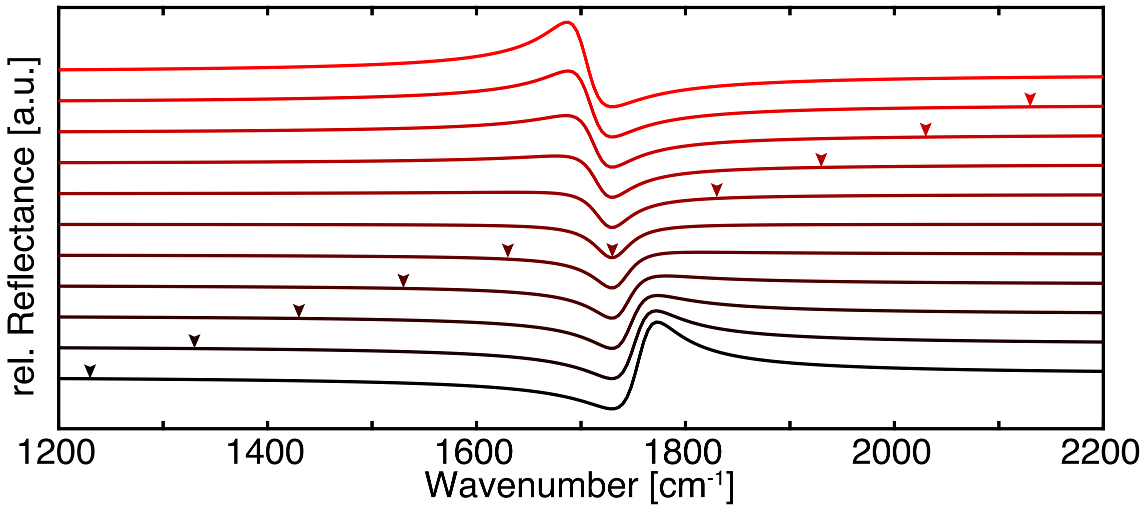

Figure 2.9 Lineshape predicted by Fano-like coupling of a discrete (narrow vibrational mode at 1730 cm^{-1}) to a continuous (broad antenna mode). The center frequency of the antenna mode is shifted from 1230 cm^{-1} (black) to 2230 cm^{-1} (red) indicated by arrows.

Finite-Difference Time-Domain Simulations Various studies reported a strong correlation of the near-field's strength around the plasmonic structures and their vibrational enhancement. Thus, assessing the near-field distribution theoretically enables *a priori* statements about the quality of antennas and yields understanding of the resultant spectra.

An elegant way of predicting the distribution of optically induced electromagnetic near-fields at an arbitrarily shaped surface of metallic structures as well as their transmission and reflection spectra and coupling to closeby molecular oscillators is to solve Maxwell's equations numerically.

One well developed and readily available method is the finite-difference time-domain (FDTD)-method[79] which was published as open-source-code by Oskooi et al. in the package 'MEEP'.[80] Shortly, the time-dependent part of the differential representation of Maxwell's equations are made dimensionless by setting $\epsilon_0 = \mu_0 = c = 1$ which makes this formalism scale invariant in space, thus, enabling any choice of the characteristic lengths scale. The simulated volume is discretized by Yee lattice[81] on which the electric field $\mathbf{E}$ and magnetic field $\mathbf{H}$ is offset by half a pixel in space and are solved temporally alternating. This procedure on the one hand greatly simplifies the simulation formalism and enhances stability. On the other hand it generates the need for interpolation of the fields which potentially reduces accuracy. In such a scheme it is very easy to implement Bloch periodic boundary conditions which mimic the lattice-like arrangement in the x-y-plane of the simulated structures. To avoid propagating waves in the z direction, perfectly matched layers (PMLs) are added at the upper and lower boundaries of the simulated volume.[79] The simulated structures material can be easily set by assigning a dielectric function $\epsilon(x,\omega)$ derived from experimental data. In the context of MEEP $\epsilon(x,\omega)$ is a superposition of a constant (first summand), Lorentzian (second summand, for harmonic resonances) and a Drude-like (third summand, for metals) frequency dependence

$$\epsilon(\mathbf{r},\omega) = \left(1 + \frac{i \cdot \sigma_D(\mathbf{r})}{\omega}\right) \left[\epsilon_\infty(\mathbf{r}) + \sum_n \frac{\sigma_n(\mathbf{r}) \cdot \omega_n^2}{\omega_n^2 - \omega^2 - i\omega\gamma_n} + \sum_m \frac{i\sigma_m(\mathbf{r}) \cdot \omega_m^2}{\omega(\gamma_m - i\omega)}\right] \tag{2.16}$$

with ϵ_∞ the instantaneous dielectric function, σ_D the electric conductivity, and $\omega_{n,m}$, $\gamma_{n,m}$ and $\sigma_{n,m}$ constants for the two nonlinear frequency dependencies (from the MEEP documentation).[80]

Once the computational cell is set up, typically a pulse with Gaussian frequency distribution is launched onto the structure and the transmitted and reflected fields are recorded. Normalization is done by running the same simulation once more lacking the structure of interest. Typically the angle of incidence (AOI) of the source is normal. For simulations under oblique AOIs Θ a spatially varying phase is added to the source such that the light propagates at the given angle e.g. in x-direction

$$I(t,\mathbf{r}) = I(t)e^{2\pi i k_x \cdot x} = I(t)e^{2\pi i\omega \sin(\theta)x}. \tag{2.17}$$

This shows that in simulations with a spectrally broad source each plane wave with frequency ω will propagate at slightly different angles according to Snell's law

$$\theta(\omega) = \sin^{-1}\left(\frac{\omega_c \sin(\theta_c)}{\omega}\right) \tag{2.18}$$

where θ_c denotes the angle at which the plane wave of the central frequency ω_c of the pulse propagates. By performing multiple simulations at different angles one can disentangle this angle-frequency dependence.[71]

For calculations of the reflectance spectra at each nominal AOI, two simulations are performed: one with the desired structure resulting in the time-dependent fields $\mathbf{E}(\mathbf{r},t)$ and $\mathbf{H}(\mathbf{r},t)$ measured at a previously set two-dimensional monitors. And a second one with exactly the same geometry lacking the plasmonic antenna resulting in the fields $\mathbf{E_0}(\mathbf{r},t)$ and $\mathbf{H_0}(\mathbf{r},t)$. Since the spectral response is the desired quantity of the computation, all four fields need to be Fourier-transformed from time-domain into frequency-domain resulting in $\tilde{\mathbf{E}}(\mathbf{r},\omega)$, $\tilde{\mathbf{H}}(\mathbf{r},\omega)$, $\tilde{\mathbf{E_0}}(\mathbf{r},\omega)$ and $\tilde{\mathbf{H_0}}(\mathbf{r},\omega)$.

To calculate the reflected power $P_r(\omega)$ of the antenna array one just needs to integrate the Poynting vector across the monitors area

$$P_r(\omega) = \mathfrak{Re}\left\{\widehat{n}\int\Big[\tilde{\mathbf{E}}(\mathbf{r},\omega) - \tilde{\mathbf{E_0}}(\mathbf{r},\omega)\Big]^* \times \Big[\tilde{\mathbf{H}}(\mathbf{r},\omega) - \tilde{\mathbf{H_0}}(\mathbf{r},\omega)\Big]\,d^2r\right\} \tag{2.19}$$

where $\widehat{n}$ is the unit vector along the incident wave vector. To calculate a relative reflecance spectrum $P_r(\omega)$ can normalized by

$$P_r^0(\omega) = \mathfrak{Re}\left\{\widehat{n}\int\Big[\tilde{\mathbf{E_0}}(\mathbf{r},\omega)\Big]^* \times \Big[\tilde{\mathbf{H_0}}(\mathbf{r},\omega)\Big]\,d^2r\right\}. \tag{2.20}$$

Grating Theory It was shown that effective coupling of the incident light to antennas and collection of the scattered light as well as spectrally shaping their response can be achieved by arranging the antennas periodically.[56,71,74,82] The periodic arrangement can be understood in terms of a grating which adds momentum vectors $\mathbf{G}_{x,y}$ to the incident wave vector $\mathbf{k}_{\text{inc}}$

$$\mathbf{k}_{\text{subs}} = \mathbf{k}_{\text{inc}} \pm \mathbf{G}_x \pm \mathbf{G}_y \tag{2.21}$$

such that a substrate-propagating wave with k_{subs} can evolve.[71] This substrate-propagating wave, when matched to a mode of the plasmonic antenna itself, excites the respective mode collectively and can lead to a change in its spectral shape and radiation pattern. This becomes particularly important when oblique AOIs θ are considered which is the case when focusing optics are employed in the experimental setup: usually an antenna will radiate most of its power normal to the long axis. This directionality is disadvantageous for the IR range since reflective optics (i.e. Cassegrain objective, cf. Sec. 3.2) are used for excitation and collection which have an angle distribution of 10° - 25° omitting normal incidence. From Equation 2.21 we can derive the corresponding grating transition wavelength $\lambda_{i,j}$

$$\left(\frac{2\pi}{\lambda_{i,j}}n_{\text{subs}}\right)^2 = \left(\frac{2\pi}{\lambda_{i,j}}\sin\theta_i\cos\phi + i\frac{2\pi}{d}\right)^2 + \left(\frac{2\pi}{\lambda_{i,j}}\sin\theta_i\sin\phi + j\frac{2\pi}{d}\right)^2 \tag{2.22}$$

for the standing waves in x and y, respectively. Here n_{subs} denotes the substrates refractive index, θ_i the AOI, ϕ the azimuthal angle and i, j the respective grating orders.

2.3 Scattering-Type Scanning Near-Field Optical Microscopy (*s*SNOM)

2.3.1 Experimental Implementation of SNOM

Typically SNOMs are separated into aperture SNOMs (or sometimes near-field scanning optical microscopes (NSOMs)) and apertureless SNOMs or *s*SNOMs:

Aperture SNOM or NSOM utilizes a manufactured sub-wavelength aperture in a fiber-probe (Fig. 2.10a) through which light is transmitted or collected. The probe can be effectively positioned above the sample using Piezo-drives[36] (see Sec. 3.4) and various feedback mechanisms like scanning tunneling microscope (STM)[83] or AFM (cantilever based, normal-force[84] or shear-force[85]). As the probe raster-scans the sample, only light which interacted in the sub-wavelength confined near-field region is detected. This increases the lateral resolution of the resultant optical image. The versatility of this approach allows various illumination and detection geometries to be employed which can yield nanoscopic reflection and transmission properties (Fig. 2.10b).[86] The transmitted powerP_{trans} through a sub-wavelength aperture is critically dependent on the wavelength λ itself and the aperture radius a

$$P_{\text{trans}} = \frac{64}{27\pi}\left(\frac{2\pi a}{\lambda}\right)^4 a^2\,\frac{c}{2}\epsilon_0 E^2{}_{\text{inc}}\,, \tag{2.23}$$

where $\frac{c}{2}\epsilon_0 E^2{}_{\text{inc}}$ indicates the incident irradiance.[87,88] As a consequence, going to mid-IR wavelengths, the transmitted power drastically decreases for a fixed aperture sizes in the nanometer range.

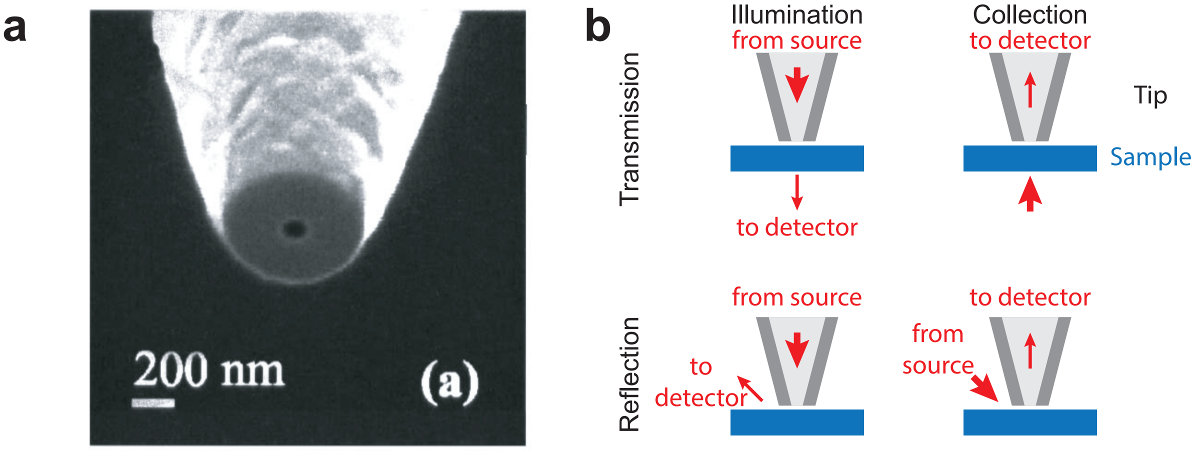

Figure 2.10 (a) FIB micrograph of an aperture SNOM tip (adapted from ref.[89]). **(b)** Four different modes of operation.[86]

Apertureless or scattering-type scanning near-field optical microscope (*s*SNOM). Instead of transmitting light through an aperture, *s*SNOM generates a confined EM field by illuminating a sharp AFM tip.[40,90] The scattered field (elastically or in-elastically) is detected in the far-field by a proper detector. The lateral resolution in such experiments is limited to usually 10-50 nm for various wavelengths depending only on the tip apex radius and up to 1 nm[40] in extreme cases.[41,91] This makes *s*SNOM a well suited technique for spectroscopic applications since it can be applied in a wide spectral range with similar performance ranging from visible[90] via mid-IR[92] to microwave[41] and even simultaneous[93] imaging.

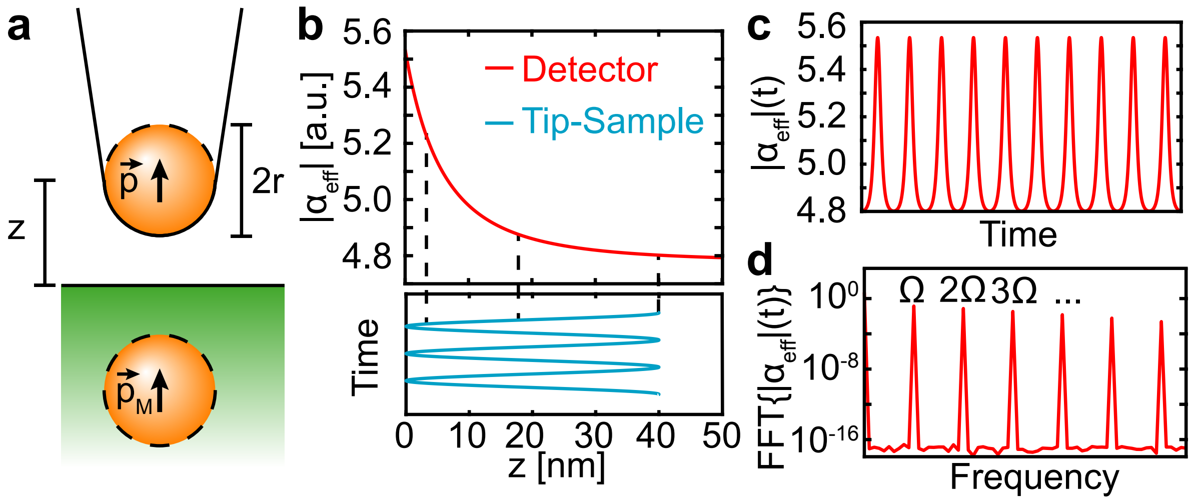

Figure 2.11 (a) A sharp tip acts as a local dipole inducing an image dipole in the sample. **(b)** Polarizability (point dipole) versus tip-sample separation (upper panel) and time harmonic modulation of the tip height (lower panel). **(c,d)** Polarizability α_{eff} in time-domain **(c)** and frequency-domain **(d)**.

Two possible field confinement mechanisms are found for metallic tips: the 'lightning-rod' effect and excitation of localized plasmons. The first one provides a field confinement by condensing the field lines at the sharp apex of the tip. The latter one additionally generates an enhanced electric field due to collective oscillations of the metals conduction electrons. For typical dimensions of metallic AFM tips (around tens of nanometers) this occurs mainly in the visible energy range. For the IR and THz range mainly the first one is found although moderate additional enhancement was found by engineering the tip to exhibit a dipolar antenna resonance in the IR.[94]

A simple mechanism of the tip-sample interaction is the point dipole model.[95] The tip apex is assumed to be a polarizable sphere of radius r separated from the surface by the distance z (Fig. 2.11a). It can be approximated by a point dipole $\mathbf{p}$ located in the center of the sphere. When approaching a surface this point dipole creates a mirror point dipole $\mathbf{p}_M$ in the surface with an effective polarizability α_{eff}. The scattered field can be written as:

$$\mathbf{E}_{\text{scat}} \propto \alpha_{\text{eff}} \mathbf{E}_{\text{inc}}. \tag{2.24}$$

The recorded signal depends non-linearly on the separation of tip and sample (Fig. 2.11b, cf. 2.3.2). Thus, dithering the AFM tip at its mechanical resonance frequency Ω (Fig. 2.11b, lower panel), as commonly done in dynamic mode or tapping mode AFM, modulates the scattered field non-linearly (Fig. 2.11b, upper panel, Fig. 2.11c) introducing higher harmonics in the frequency domain (2.11d). Lock-in detection at higher harmonics $n\Omega$ of the tip suppresses unwanted background signals originating from light scattered at the tips shaft or the sample surface itself.[96]

Although the detection at higher harmonics suppresses most of the background there can be still so-called 'multiplicative background' $\mathbf{E}_{\text{bg}}$ present. It enters the detected signal via interference and can significantly change while scanning. To extract the pure near-field contribution a pseudo-heterodyne detection scheme was proposed.[97] The scattered light interferes with a reference beam of constant amplitude but temporally varying phase $\mathbf{E}_{\text{ref}}(t) = \mathbf{E}_{\text{ref,0}} exp^{i\gamma sin(2\pi Mt)+i\Psi_{\text{ref}}}$. The signal output by the detector can be written as

$$|\mathbf{E}_{\text{det}}|^2 \propto |\mathbf{E}_{\text{scat}} + \mathbf{E}_{\text{ref}} + \mathbf{E}_{\text{bg}}|^2. \tag{2.25}$$

Figure 2.12a depicts a generic signal seen by the detector ($\gamma = 2.63$). The slow modulation is due to the sinusoidal phase modulation (indicated in black). The fast spike like features on top correspond to the near-field modulation, mediated by the dithering tip (indicated in blue).

From equation 2.25 we can see that double lock-in demodulation at the tips higher harmonics $n\Omega$ and it's sidebands mM leaves only product terms of $\mathbf{E}_{\text{scat}}$ and $\mathbf{E}_{\text{ref}}$. The near-field scattered filed phasor can be expressed as a Fourier series with Fourier coefficients $\sigma_n = \text{s}_n \text{exp}^{i\phi_n}$.[97] One can show that the intensity $I(n\Omega + mM)$ at the sidebands can be expressed as when the demodulation order $n > 1$:

$$I(n\Omega + mM) = \kappa|\mathbf{E}_{\text{ref,0}}|J_m(\gamma)s_n cos(\phi_n + \Psi_{\text{ref}} - m\pi/2) \tag{2.26}$$

κ is a constant which collects all detector and setup specific parameters, $J_m(\gamma)$ the Bessel function of first kind s_n the magnitude of the scattered field at the harmonic n, its corresponding argument ϕ_n and Ψ_{ref} a constant phase offset in the reference field. Figure 2.12b shows the FT of 2.12a. Multiple side bands spaced with ± M (black) are created around the near-field modulation at $n\Omega$ (blue) which carry the phase sensitive information of the near-field scattered light.

With Equation 2.26 one can readily derive an expression for the complex scattered field detected at the tips harmonic n:

$$\sigma_n = k\{I(n\Omega + jM)/J_j(\gamma) + iI(n\Omega + lM)/J_l(\gamma)\} \tag{2.27}$$

by setting $\gamma = 2.63$, the Bessel functions of first kind will be equal $J_1(\gamma) = J_2(\gamma) = 1/2.16$ for $l = 1$ and $j = 2$. This simplifies equation 2.27 to

$$\sigma_n = 2.16k\{I(n\Omega + jM) + iI(n\Omega + lM)\}. \tag{2.28}$$

Equation 2.28 can be efficiently used to derive the phase and magnitude of the scattered field at a given harmonic n while scanning the tip across a sample by lock-in detection of their sidebands.

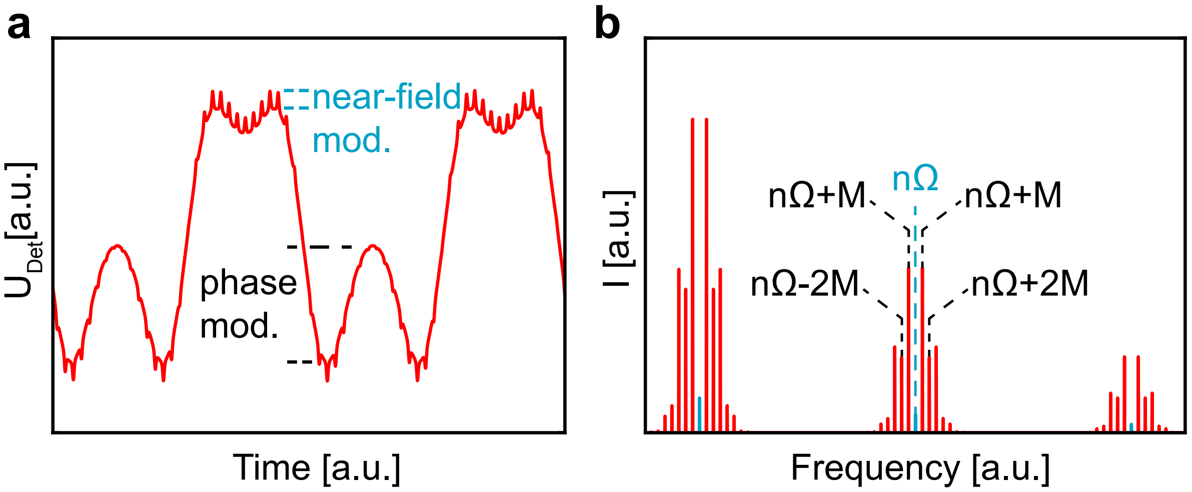

Figure 2.12 **(a)** The voltage seen by the detector produced by the scattered field interfered with the phase modulated reference field. **(b)** FT of the time domain signal. The sidebands at $n\Omega + mM$ can be used for phase retrieval.

A disadvantage of this method is the restriction of the retrieved phase ϕ_n to 0 to $\pi/2$. Moreno et al. recently reported how to recover the full $[0, 2\pi)$ phase from pseudo-heterodyne sSNOM data.[98] They suggest instead of using the modulus $I(n\Omega + jM)$ of the sidebands for reconstructing the near-field amplitude and phase in eqn. 2.28 rather to employ the real part $X(n\Omega + jM)$ of each sideband.

$$\sigma_n = 2.16k\{X(n\Omega + jM) + iX(n\Omega + lM)\} \tag{2.29}$$

By this, a proper sign is assigned to each of two summands in eqn. 2.29 which enables to locate the phasor in all four quadrants. A full description of the implementation can be found in Section A.8 For this method to work, the phase between the local oscillators of the LIA and each demodulated sideband needs to be set to zero before the measurement or to be determined via post-processing. However, it will be explicitly stated when this method was applied to the data.

2.3.2 Theoretical Modeling of the Contrast in sSNOM Experiments

Point Dipole Model Hillenbrand and Keilmann were first to propose a simple quasi-static induced point dipole model:[90,95] the tip is approximated as a sphere with radius a resting with distance z above the sample surface. The incident field polarizes the sphere $\mathbf{p} = \alpha \mathbf{E}_{\text{inc}}$ with

$$\alpha = 4\pi a^3 \frac{\epsilon_{\text{tip}} - 1}{\epsilon_{\text{tip}} + 2}. \tag{2.30}$$

This point dipole induces a mirror-dipole in the sample half-space of $\mathbf{p}_{\text{S}} = \beta \mathbf{p}$ with

$$\beta = \frac{\epsilon_{\text{S}} - 1}{\epsilon_{\text{S}} + 1}. \tag{2.31}$$

Superposing this induced dipole–mirror-dipole fields one ends up with an effective polarizability

$$\alpha_{\text{eff}} = \frac{\alpha}{1 - \frac{\alpha\beta}{16\pi(a+z)^3}}. \tag{2.32}$$

Additionally taking into account an indirect illumination through Fresnel reflection of the incident beam at the sample surface $(1 + r_{\text{p}})^2$ yields the following scattered field

$$\mathbf{E}_{\text{scat}} \propto (1 + r_{\text{p}})^2 \alpha_{\text{eff}} \mathbf{E}_{\text{inc}}. \tag{2.33}$$

Figure 2.13 shows the expected near-field spectra for a sphere of 20 nm radius 5 nm above a sample surface, which exhibits two Lorentzian oscillators which are chosen to be similar to a protein thin film. The most prominent feature in this result is that the absorptive information is stored in the imaginary part and the refractive part in the real part of the detected signal which is just inverted when compared to conventional absorption spectroscopy.

The phase of the near-field scattered light is approximately proportional to the imaginary part of the scattered light.[45] For weakly dispersive oscillators (like molecular vibrations) the

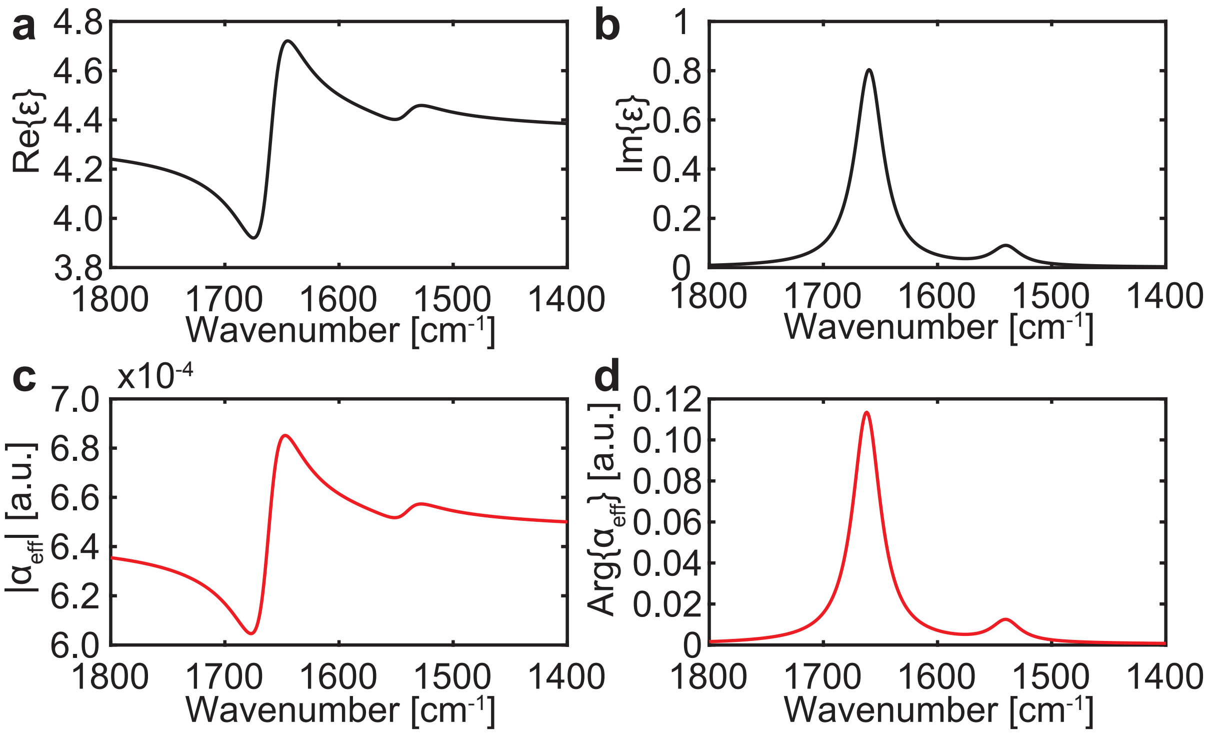

Figure 2.13 **(a)** Real and **(b)** imaginary part of a dielectric function mimicking a protein thin-film (two Lorentzian oscillators). **(c)** Magnitude and **(d)** phase spectrum calculated from **(a,b)** using the point dipole model.[90]

imaginary part of the scattered signal $\mathrm{Im}(\sigma_n(\nu))$ is proportional to the imaginary part of the samples dielectric function $\epsilon_2(\nu)$,[99,100] leading to the following relation

$$\phi_n(\nu) \sim \mathrm{Im}(\sigma_n(\nu)) \propto \epsilon_2(\nu). \tag{2.34}$$

Finite-Dipole Model A more detailed description of the scattered light assumes the tip as an ellipsoid with length L and radius R at the ends of the elongated axis. The effective polarizability can be written as[101]

$$\alpha_{\mathrm{eff}} = R^2 L \frac{\frac{2L}{R} + \ln\frac{R}{4eL}}{\ln\frac{4L}{e^2}} \left(2 + \frac{\beta\left(g - \frac{R+H}{L}\right)\ln\frac{4L}{4H+3R}}{\ln\frac{4L}{R} - \beta\left(g - \frac{3R+4H}{4L}\right)\ln\frac{2L}{2H+R}} \right). \tag{2.35}$$

It was shown that this formalism yields a better theoretical prediction of spectra of strong oscillators (e.g. SiC phonos) compared to the point dipole model. In this work we exclusively used organic molecules which are weekly absorbing for which the point dipole model still is a reasonable good theoretical representation.

2.4 The Anomalous Nernst Effect (ANE)

Ettlingshausen and Nernst described in 1886 the occurrence of an electric field $\mathbf{E} = E\mathbf{e}_x$ when a metal plate is placed in a magnetic field $\mathbf{B} = B\mathbf{e}_z$ and additionally a temperature gradient $\nabla T = [\nabla T]_y$, perpendicular to first two fields, is applied (Fig. 2.14).[102]

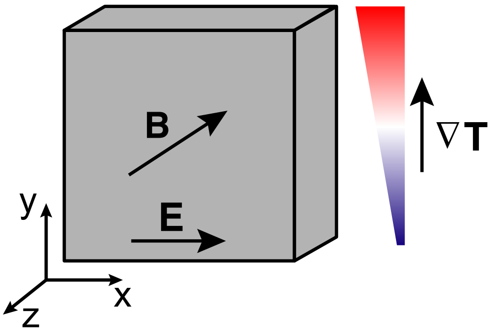

Figure 2.14 Schematic representation of the Nernst effect. A temperature gradient ∇T perpendicular to a **B**-field generates an electric field **E** perpendicular to the two former.

In analogy to the anomalous Hall effect, applying a temperature gradient ∇T to a ferromagnet generates a voltage difference perpendicular to the gradient and the direction of the ferromagnets magnetization $\mathbf{e_M}$ (unit vector along the magnetization $\mathbf{M}$) via the ANE.[103]

$$\nabla V_T = -\mathbf{E} = S_N \mathbf{e_M} \times \nabla T \tag{2.36}$$

with $S_N = |N_{ANE}|\mu_0 M_S$, N_{ANE} the anomalous Nernst coefficient and $\mu_0 M_S$ the magnetic moment of the device with M_S the saturation magnetization. In contrast to other magneto caloritronic effects like the anisotropic magneto thermopower or the planar Nernst effect, the ANE is linearly dependent on the magnetization. This yields the advantage to separate the ANE from other effects simply by repeating the experiment at an opposite magnetization $\mathbf{M} \rightarrow -\mathbf{M}$. We will consider in addition to the ANE the anisotropic Seebeck effect to understand the contrast in the experiments discussed in Section 4.2.4. The total electric field $\mathbf{E}$ can be described by

$$\begin{pmatrix} E_x \\ E_y \\ E_z \end{pmatrix} = \begin{pmatrix} S_{\parallel} \sin^2\theta + S_{\perp}\cos^2\theta & -S_N\cos\theta & (S_{\parallel} - S_{\perp})\cos\theta\sin\theta \\ S_N\cos\theta & S_{\perp} & -S_N\sin\theta \\ (S_{\parallel} - S_{\perp})\cos\theta\sin\theta & S_N\sin\theta & S_{\parallel}\sin^2\theta + S_{\perp}\cos^2\theta \end{pmatrix} \begin{pmatrix} [\nabla T]_x \\ [\nabla T]_y \\ [\nabla T]_z \end{pmatrix}. \tag{2.37}$$

Here $S_{\parallel}$ and $S_{\perp}$ denotes the Seebeck coefficient when the temperature gradient is parallel or transversal to the magnetization, respectively. θ corresponds to the angle between the magnetization $\mathbf{M}$ and the z-axis. The electromotive force (EMF) V_T can be estimated by integration of the x component along the magnetic device ($\mathrm{d}V_T = -E_x \mathrm{d}x$) since the voltage measurement will take place along that direction.[104] Furthermore we will assume that the temperature $[\nabla T]_z$ gradient along z will be negligible. This leaves only the first two elements in the first row of the matrix.

We will use this effect in the following to conceptually show the possibility of imaging ferromagnetic devices in which a domain wall (DW) separates two compartments with opposing magnetization. The EMF V_T will be acquired by scanning a nanoscopic heater – the optical near-field at the apex of a gold coated AFM tip illuminated by IR radiation – across a magnetic device.

3

Experimental Setups and Materials

3.1 Preparation of Enhancing Solid Supported Antennas

Gold Gold (Au form lat. *Aurum*) is a transition metal with atomic number 79 in group 11. It is one of the most used metals in plasmonics besides silver and aluminum. Despite its low abundance in earths crust, it is handy in processing (e.g. thermal evaporation) and resistant against chemicals. Especially modification of a gold surface with organic and inorganic capping layers via a sulfur-gold bond is of utmost importance in life science.[105] All of these properties render gold a unique material for plasmonic structures in biological and chemical applications.

Metal Film Deposition There are different methods available for creating highly pure gold films on different materials (see Tab. 3.1).

	Method	**Substrate Material**	**Substrate Shape**
CD	Electroplating Electroless deposition	conductive⋆ Si[106] or ZnSe[65]	arbitrary
PVD	Sputtering Thermal evaporation Electron-beam evaporation	arbitrary	normal incidence

Table 3.1 Different methods are available for chemical deposition (CD) or physical vapor deposition (PVD) of gold.[107,108] ⋆Deposition feasible on pre-treated insulating materials.[109]

Only physical vapor deposition (PVD) can be used to create films on arbitrary substrate materials. Its directionality is essential for the shadowing procedure described below.

All gold films were prepared by PVD of gold evaporated off a resistively heated elongated dimple boat made from tungsten (EVS31A010W, Kurt J. Lesker Company Ltd., Germany). All preparations were done in a EcoVap 3 evaporation chamber (MBraun, Garching, Germany). Deposition of a smooth gold film was deposited at a rate of ~1 Å/s and a pressure of ~1x10^{-6} mbar. The desired thickness of the films was 50 nm and checked by AFM *ex-situ*. The thickness was chosen such that gold reaches its bulk optical properties which occurs for films thicker than 20-30 nm.[110] No adhesive layer (e.g. titanium or chromium) was applied to the substrates before the gold deposition.

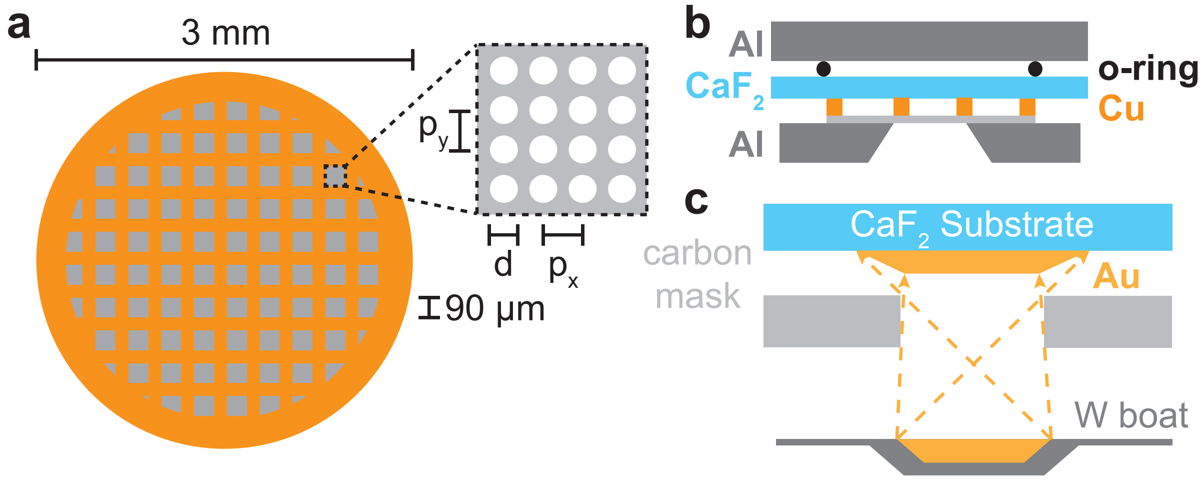

Figure 3.1 (a) Layout of the TEM grid used as nano-stencil. **(b)** Shadowing effect during evaporation from a finite source.

Surface Patterning was achieved by nanostencil lithography.[75,111] Commercially available cryogenic (cryo)-TEM grids covered by a 20-40 nm thick holey carbon film (2/1 C-Flat, Protochips, Morrisville, USA, Fig. 3.1a) were deployed as a shadow mask during metal deposition. The circular apertures in the carbon film were chosen to be $d = 2\mu$m in diameter. These were arranged in a square lattice with periodicity $p_x = p_y = 3$ μm. The carbon film is fixed on the supporting copper grid ($\varnothing_{\text{Cu}}$ = 3 mm, thickness $t \sim 50$ μm, 200 lines per inch). The grids were attached to CaF_2 substrates (Eksma Optics, $\varnothing_{\text{CaF}_2}$ = 12 mm) and fixed by a custom made aluminum holder as described in the following (Fig. 3.1b). A TEM grid is placed on an aperture in the aluminum holder and covered with a cleaned CaF_2 substrate (15 minutes sonication in isopropanol). The carbon film is oriented such that it is averted from the substrates surface. A rubber o-ring is placed on top of the CaF_2 and the sandwich fixed with a aluminum counter plate. This geometry ensures that the free standing carbon shadow mask has no physical contact with the substrate and later deposited antennas. This spares the need for an adhesion layer beneath the gold and prevents precontamination by the lithography process (e.g. by poly(methyl methacrylate) (PMMA) used in EBL). To maintain a constant distance of the carbon film to the substrate the grids are slightly pressed against the CaF_2 by the counter plate. The finite distance of the shadow mask to the substrate surface and and the finite lateral extension of the evaporation source leads to a blurring of the resulting gold structures as inferred from Figure 3.1c (see Sec. 4.1.1). These structures are discs arranged in a square lattice according to the square-lattice circular apertures in the TEM grids. They will be referred to as disc antenna arrays (DAAs) in the following.

Modification of Disc Antenna Arrays (DAA) by Self-Assembled-Monolayers (SAM) To evaluate the DAAs two different types of molecules were covalently bound via gold-sulfur bond: a small organic molecule, 4-mercaptobenzoic acid (4-MBA), and a detergent stabilized light-sensitive membrane protein sensory rhodopsin II from *Natromonas pharaonis* (*Np*SRII) (Fig. 3.2).

4-MBA (Fig. 3.2a, $M_w = 154.19$, 99%, Sigma-Aldrich Chemie GmbH, Germany) consists of a central phenyl-ring. A thiol is located at carbon 1 and a carboxylic acid at carbon 4. It is well studied in a SAM-configuration by various methods including IR spectroscopy[114–117] and, thus, serves as a model system for validating the presented DAA structures in different chemical environments. Neglecting the hydrogens at the carboxyl and sulfhydryl, 4-MBA has a C_{2v} symmetry with its according symmetry axis. The protonation state of its carboxylic moiety is easily changed by adjusting the surrounding solution pH.

For *ex-situ* spectroscopic characterization (cf. Sec. 4.1.2) DAAs were incubated for 1 h in the 4-MBA-dimethylsulfoxide (DMSO) solution and subsequently rinsed with milli-Q water and dried under ambient condition. For *in situ* observation of the 4-MBA adsorption kinetics and pH titration (cf. Sec. 4.1.3), the DAAs were incubated for 2 h in either the 4-MBA-DMSO solution (1 mM) or 4-MBA-water (~100 μM) solution in the home-built flow cell (Fig. 2.8b) until a SAM was established. The volume in the flow cell was thereafter rinsed with a buffered solution (see Sec. 3.1).

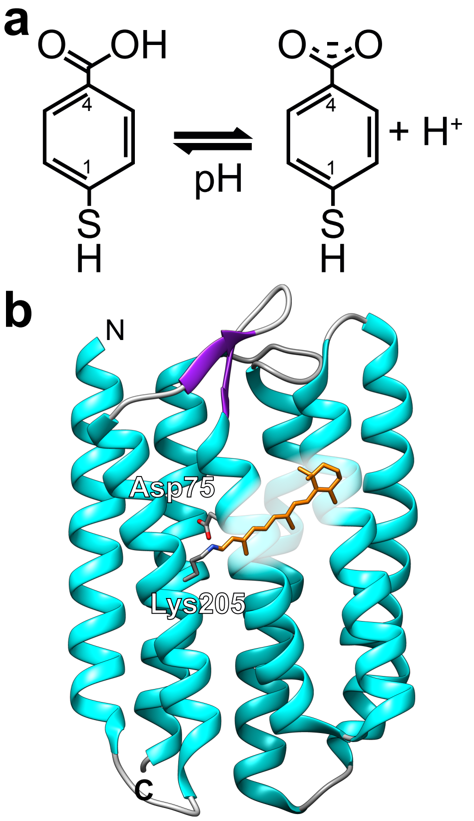

Figure 3.2 (a) Molecular structure of 4-MBA in its (de-)protonated state. **(b)** Crystal structure of *Np*SRII (pdb entry: 1JGJ,[112] UCSF Chimera[113] program used for preparation of 3D representation).

***Np*SRII** (Fig. 3.2b) is a light-sensitive retinal membrane protein of *Natronomonas pharaonis* which is involved in the negative phototactic response of these bacteria (earlier called '*pharaonis* phoborhodopsin').[118] Its secondary structure formed from the 239 amino acid long peptide chain is dominated by seven transmembrane α-helices (similar to bacteriorhodopsin (bR),[112] Fig. 3.2b). The all-*trans* retinal chromophore is bound via a Schiff base linkage to lysin 205 of the protein fold. The cofactor gives rise to a visible absorption at λ_{max} ~500 nm which lets the protein solution appear orange.[118] Upon absorption of a photon the retinal isomerizes to its 13-*cis* conformation and induces *Np*SRIIs photocycle. During the photocycle several conformational changes take place which show characteristic spectral states K_{NpSRII}, L_{NpSRII}, M_{NpSRII}, N_{NpSRII} and O_{NpSRII} similar to the one of the well studied bR.[119] Naturally *Np*SRII has a transducer HtrII presumably attached to helix F and G responsible for signaling motility.[112]

In this study *Np*SRII was used as a model system for light-sensitive proteins without its transducer. The protein was kindly supplied by AG Schlesinger (Genetic Biophysics, Departement of Physics, Freie Universität Berlin, 14195 Berlin, Germany). It was expressed and purified by Fucsia Crea as previously described.[120] The sequence of *Np*SRII was genetically engineered by AG Schlesinger to expose a methionine alanine cysteine histidine (MACH) sequence on its N-terminus.[121] The cysteines thiol serves for oriented binding of the protein to the gold surface. A SAM of *Np*SRII was established by incubation of a DAA with buffer (50 mM MES, 4 M NaCl, pH 6.6) containing ~20 μg / ml purified protein, solubilized in 0.05% detergent (n-dodecyl β-D-maltoside (DDM), > 99 %, Glycon Biochemicals GmbH, Luckenwalde, Germany) for at least 6 h. Subsequently the flow cell volume was rinsed by pure buffer.

pH Titration of a 4-MBA-SAM For titration of the created 4-MBA monolayer the volume of the flow cell was flushed with buffer (10 mM [sodium citrate + TRIS + PIPPS + CHES], 30 mM NaCl) adjusted to different pH. Subsequently a spectrum was recorded. The buffer pH was step wise adjusted by adding few drops of either 1M HCl (Carl Roth GmbH + Co. KG, Germany) or 1 M NaOH freshly prepared from dry pellets ($\geqslant$ 99 %, Carl Roth GmbH + Co. KG) and measured with a pH meter (MP 225, Mettler-Toledo GmbH, Germany). Addition of acid or base altered the salt concentration in the buffer such that the concentration in this experiments will be referred to as c(NaCl) $<$ 100 mM. For pH titration experiments with higher salt concentrations the buffer was already prepared to contain 500 mM NaCl before the actual titration of the buffers pH.

Light-induced spectrscopy of *Np*SRII A blue diode-pumped solid-state laser (473nm, ~10 mW cm^{-2}, CNI, Changchun, China) was used to excite the protein film driving it into the photostationary M state.[122] Periodically switching on and off the excitation laser enabled the acquisition of multiple light-induced difference spectra. In total 400.000 spectra at four different positions on the DAA where recorded and averaged. The spectral resolution was set to 8 cm^{-1} and the spectral range limited to 600 - 2500 cm^{-1} by built in filters of the spectrometer in these experiments. This allowed to reach a mirror velocity of 240 kHz, resulting in a faster acquisition rate as in the pH-dependent experiments described above.

3.2 FTIR Microscope

For spectroscopic characterization of the DAAs and later SEIRAS, a FTIR-microscope (Hyperion 2000, Bruker Optik GmbH, Germany) equipped with a reflective Cassegrain objective (x15, numerical aperture (NA) of 0.4) was used. The spectral range was set to 600 cm^{-1} to 5000 cm^{-1} at a spectral resolution of 2 cm^{-1} with the mirror velocity set to 40 - 80 kHz. Spectra were acquired by averaging 500 individual spectra. For acquisition of adsorption kinetics only 65 spectra every 30 seconds were averaged. Spectra were taken in transmission or reflection configuration (Fig. 3.3a). The region of interest was narrowed down to ~90 x 90 μm^2. As seen from Figure 3.3b the reflective objective illuminates the sample and collects reflected or scattered light in a range of angles $\theta_{min} < \theta < \theta_{max}$ ($\theta_{min} \sim 10°$ and $\theta_{max} \sim 24°$ for the used objective). The angle distribution is important when considering periodically arranged antennas as used in this thesis. Here the AOI determines the most efficient coupling wavelength at a given periodicity (see Sec. 2.2.4).

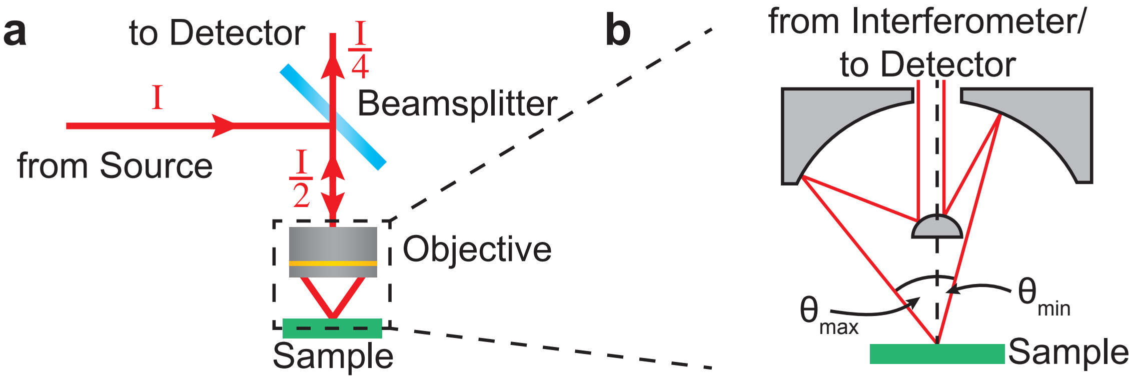

Figure 3.3 (a) Schematic layout of the microscopes beam path. Even for a sample with reflectivity $r = 1$ the total intensity send to the detector is a fourth of the incident intensity I. **(b)** Cross section of a Cassegrain objective with extreme AOIs θ_{max} and θ_{min}.

3.3 Angle-Resolved Finite-Difference Time-Domain Simulations of Disc Antenna Arrays

The geometry of a single disc antenna was modeled according to the topographies by conical discs with an upper diameter of 1 μm, a lower diameter of 2.5 μm and thickness of 50 nm made of a Drude-like metal using the parameters of Johnson and Christy.[110] The cone was located in the center of a 3μm x 3μm x 15.05μm computational cell with periodic boundary conditions (Fig. 4.5a). The CaF_2 support was accounted for by filling the lower half of the computational cell with a dielectric of constant refractive index of 1.41.[123] To resolve the angle-dependent reflectance spectra of the antenna array several simulations were performed. The AOI of the Gaussian pulse at 2000 cm^{-1} was varied from 0° to 30° in steps of 2.5°.

3.4 Atomic Force Microscope

The first atomic force microscope (AFM) was build by Binning et al. in 1986.[124] Shortly, a sharp tip with a radius of one to tens of nm is fixed on a cantilever. When a sample is brought close enough to the tip, it senses interatomic forces. These are transmitted to the cantilever which, in turn, bends. The bending is efficiently inferred from the reflection of a laser on the back side of the cantilever. Conceptually being close to a Scanning Tunneling Microscope, the tunneling current for surface sampling is replaced in a AFM by interatomic forces: short ranged attractive dipole-dipole forces (Van der Waals force) and repulsive ionic interaction and Pauli's principle (Pauli exclusion principle) which can be effectively described by the Lennard-Jones-potential.[125,126] Additionally, long ranged attractive or repulsive electrostatic forces can act on the tip depending on the potential difference between tip and sample.

3.4.1 The Setup

The AFM used in this thesis was a Nanowizard II (JPK Instruments AG, Berlin). The deflection of the cantilever is sensed by a quadrant photodiode, which detects the reflection of a laser on the backside of the cantilever. This enables reading out the mechanical bending of the cantilever at sub-nm precision. For accurate sub-nm positioning of the sample relative to the tip, either the cantilever or the sample is displaced by a x-y-z piezo tube. The used AFM comprises both options which will become important when coupling steady external optics to the tip. External optics need to be fixed relatively to the tip. This leaves displacement of the sample as only practicable option. The tip-sample distance is adjusted by a proportional-integral control loop. The loop takes the force acting on the tip as a measure and adjusts the sample-tip distance such that it comes as close as possible to the set-point.

3.4.2 The Tip

As the tip is the AFMs sensor it is crucial to successful imaging. Usually silicon or silicon-nitride is used as material for the tips. It is cost-effectively handled in parallel mass production, allows for precise manufacturing via chemical etching which is mainly based on already well established semiconductor technology. A further advantage of using silicon based tips and cantilevers is the high resistance against mechanical stress. Although for normal AFM imaging such stock silicon cantilevers are perfectly suited, metal coated tips were used throughout this study. The metal coating increases the scattering efficiency *s*SNOM experiment tremendously due to its higher polarizability at optical and infrared wavelengths. $PtIr_5$ coated tips with a resonance frequency of $\Omega \sim$250-290 kHz with a nominal tip radius better than 25 nm (Arrow-NCPt, NanoAndMore GmbH, Germany) were chosen since these tips are used in many published *s*SNOM studies, which ensures best comparability of our results with other works.

3.4.3 Modes of Operation

The tip can be operated in mainly two modes:

Contact Mode approaches the tip into physical contact with the surface – i.e. until the onset of Paulis repulsive exclusion principle. Usually, a certain bending of the tip is chosen as set-point. This is maintained by a proportional-integral-control loop. The set-point corresponds to a net force exerted on the sample while imaging and typically needs to be kept at an minimum to prevent damage on either the tip or the sample.

Dynamic Mode oscillates the cantilever at or close to its mechanical resonance frequency Ω. This opens different regimes of operation: in *non-contact mode* mode the set-point is chosen to be in the attractive range. The tip is ideally never in mechanical contact with the surface. This mode is difficult to establish under environmental conditions due to low Q factors of the oscillating tip in air.[126] For *tapping* or *intermittent contact mode* the set-point is set such that the tip senses repulsive force while its oscillation. It virtually taps on the surface. This mode is more stable than non-contact mode but can easier lead to tip damage.

In the following the AFM will be operated in *tapping mode* as it is convenient for imaging and enables efficient lock-in detection of light scattered from the tip on the frequencies $n\Omega, n = 1, 2, 3 \ldots$ in a *s*SNOM experiment (see next Section).

3.5 sSNOM

As described previously (Sec. 2.3.2) the most convenient way, from a spectroscopic point of view, of nano-focusing light using a tip is apertureless or scattering-type SNOM. In the following the characteristics of the custom build *s*SNOM and nano-FTIR setup shall be depicted in detail as it is a substantial part of this thesis. Basically the created setup consists of the focusing optics, an asymmetric Michelson-type interferometer and different light sources (Fig. 3.4). The 'sample' and 'reference' arm are described in detail in the following sections.

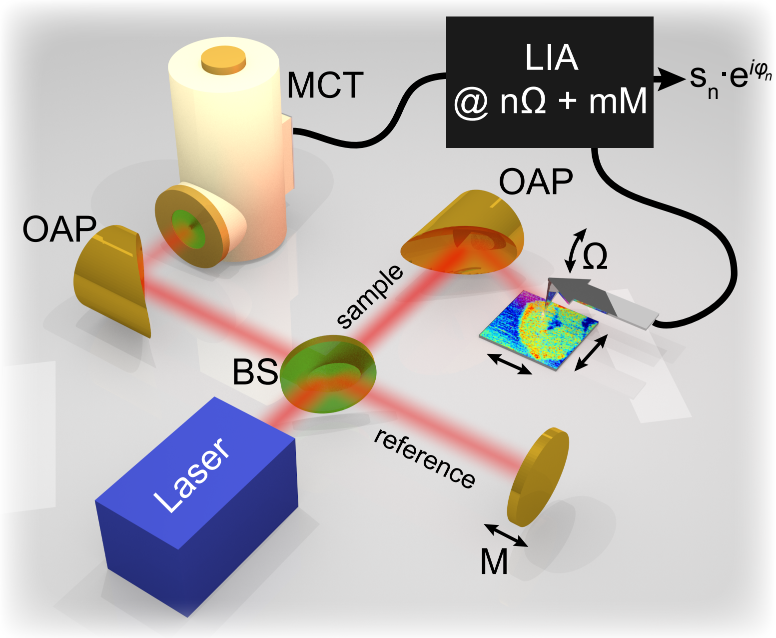

Figure 3.4 Overview of the *s*SNOM Setup. An IR laser source illuminates a metallic AFM tip, vibrating at its mechanical resonance Ω, via an off-axis parabolic mirror (OAP). In the reference arm the light is reflected at a mirror vibrating at frequency M introducing a periodic phase shift. Light back-scattered from the tip (sample arm) and from the phase modulated reference arm, is combined at the beam-splitter (BS) and interferometrically detected by the mercury-cadmium-telluride (MCT). The background free complex near-field $s_n e^{i\varphi_n}$ is extracted by a lock-in amplifier (LIA) at the frequencies nΩ + mM (see Sec. 2.3.2).

3.5.1 Detection Schemes

A side-illumination scheme turned out to yield good results with low cost and compatibility with already existing equipment. For this purpose many setups use metal coated OAPs with high numerical apertures (neaSNOM , neaspec GmbH or nanoIR2-s^{TM}, Bruker Optik GmbH). A silver or aluminum coating for example allows the use of the same setup and adjustment over a spectral range from ∼400 nm to 20 μm. Taubner et al. demonstrated similar performance in the visible to mid-IR range even with the same tips.[91] Despite the poor imaging quality of metal plated OAPs they are an ideal focusing device for side-illumination of a sSNOM tip and collection of scattered light due to their low chromatic aberrations.[127] This is another essential property of OAPs for nano-spectroscopic applicability. The only disadvantage of these mirrors is their sensitivity to alignment. Slight deviations of the incident beam off the optical axis of the paraboloid results in severe astigmatism.[127] The astigmatism needs to be reduced as much as possible. One possibility is to mount the parabolic mirror on a reflecting plane. Thereby the base plate of the OAP and, thus, the mirror itself can be adjusted to normal incidence. In the presented work a gold coated 90° OAP with 12.7 mm diameter and 15 mm focal length was used (Thorlabs GmbH, Germany).

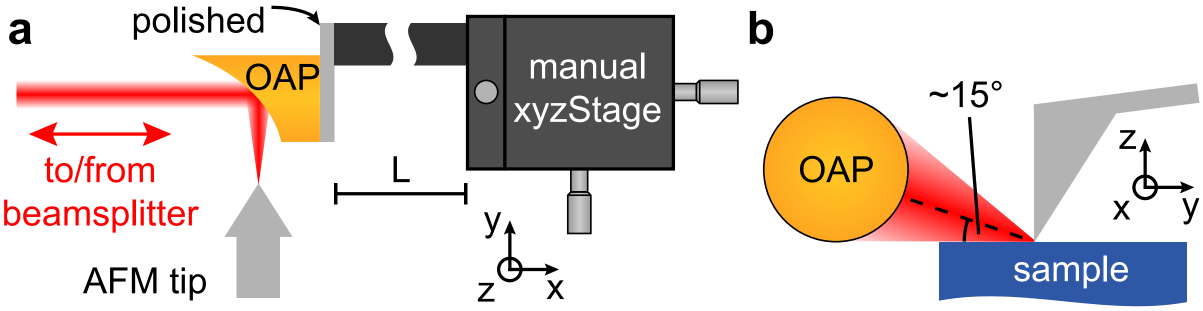

Figure 3.5 (a) Top view of the tip arm design. A 90° off-axis OAP is mounted on a polished stainless steel support. The support is used for adjusting the tilt and yaw of the OAP. The support is mounted via a lever on a *x*-*y*-*z* translation stage. **(b)** Side view of the OAP. The OAP is tilted such that the light focused on the tip travels at 75° off the surface normal.

To efficiently collect the scattered light it is lead by a ∼50:50 beam-splitter to another OAP which focuses the radiation to a suited detector. In the case for mid-IR radiation the beamsplitter could be an uncoated zinc selenide (ZnSe) window which has a reflectivity of R∼ 0.28 for s polarization at 45° due to Fresnel reflection. In this frequency range conventionally a liquid nitrogen cooled MCT detector with a built-in preamplifier is used (KLD-0.01, Kolmar Technologies Inc., USA). The preamplifier was supplied by a home-built regulated constant voltage power supply. The detector was placed on a manual *x*-*y*-*z* micrometer stage for proper alignment.

The detected light was fed into a LIA (HF2LI, Zurich Instruments, Switzerland). Demodulating the detected light at higher harmonics of the mechanical resonance frequency $n\Omega$ of the tip results in suppression of unwanted background[128] (cf. Sec. 2.3.2). This background could be light scattered off the tip shaft, the cantilever or inhomogeneities of the sample surface which is as well modulated at the tip fundamental frequency Ω. Thus demodulation at harmonics $n > 1$ is necessary. Still, coherently scattered light can lead to interferometrically transduced artifacts while scanning. To suppress these, interferometric detection as depicted in Figure 3.4a was suggested.[90]

3.5.2 The Interferometer

Beside the tip and its focusing optics the most important development was the introduction of interferometric detection of the tip-scattered light $E_{tip}(t)$. In the homodyne case, i.e. when the scattered light interferes with a reference beam E_{ref} of same phase and frequency as the illumination light but much higher intensity ($|E_{ref}| \gg |E_{tip}|$), the modulation depth introduced by the mechanical dithering of the tip is amplified. This can be understood by writing the field detected by the MCT as

$$|\mathbf{E}_{\text{Det}}(t)|^2 = |\mathbf{E}_{tip}(t)|^2 + |\mathbf{E}_{ref}|^2 + 2|\mathbf{E}_{ref}E_{tip}(t)|. \tag{3.1}$$

The first term is small since $|\mathbf{E}_{ref}| \gg |\mathbf{E}_{tip}|$ and the second constant in time. The last term multiplicatively enhances the modulation depth of the tip-scattered light by a factor $2\,|\frac{\mathbf{E}_{ref}}{\mathbf{E}_{tip}}|$. The tip-scattered light generally contains the near-field contribution as well as light coherently scattered at the tip shaft or the sample. Thus, demodulation at higher harmonics is not sufficient to suppress this multiplicative background term (cf. 2.3.2).[97] To single out the pure near-field contribution a heterodyne[90] and later a pseudo-heterodyne[97] detection was successfully adapted for *s*SNOM. In the following two paragraphs the experimental realization of this demodulation scheme will be presented for the case of a single frequency source used for imaging and a source with a broad frequency distribution used for nano-spectroscopy.

Single Frequency Imaging For single frequency imaging the suggested pseudo-heterodyne detection scheme was used.[97] The tip-scattered light is interfered with light from a reference arm whose phase is periodically modulated relative to the phase of the tip-scattered light (see Sec. 2.3.1).

In the original work[97] the mirror in the reference arm is mounted on a piezo actuator. The piezo is driven sinusoidally at frequency M which results in the sinusoidal phase modulation with a modulation depth γ = 2.63 rad (cf. 2.3.2). To accurately set the modulation depth, the phase was varied slowly with a sawtooth pattern additionally to the sinosoidal modulation.

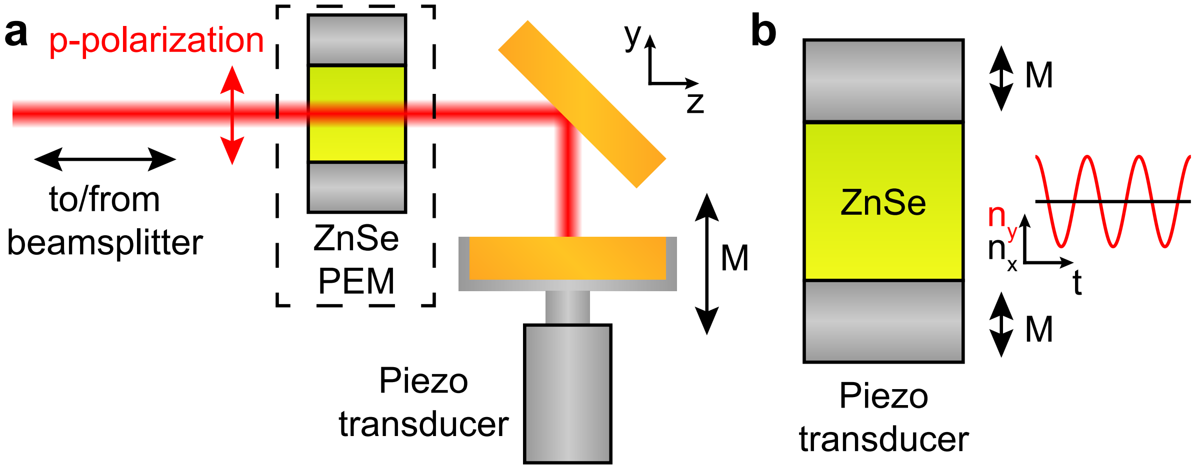

Figure 3.6 (a) Reference arm layout for pseudo-heterodyne detection using a piezo transducer or PEM based phase modulation. **(b)** Photoelastic effect: the anisotropic compression of the ZnSe crystal along the y-axis leads to a corresponding change in refractive index. Accordingly, the phase is retarded along the y-axis whereas it is unaffected along the x-axis.

γ was then optimized such that the determined optical phase φ_n varied according to the sawtooth pattern linearly and the amplitude s_n stayed constant. The advantage of this method is the broad acceptable frequency range of this technique since only the amplitude of the phase modulation needs to be changed. The disadvantage is the limitation in the modulation frequency to hundreds of hertz. Higher frequencies would lead to higher forces at the inflection points of the mirrors trajectory which creates a mechanical crosstalk between the piezo drive and the AFM. The mirrors frequency was set to 250-350 Hz where ever a minimal crosstalk was achieved. The limitation of the modulation frequency has a rather slow acquisition rate as consequence. The time constant of the downstream LIA needs to be adequately high to properly filter the modulation frequency. This results in a acquisition rate of $\sim$100 pixels per second. This demodulation scheme was realized in this work using a piezo actuator (P-843.10, Physik Instrumente (PI) GmbH & Co. KG, Germany) controlled by the HF2LI LIA. During the scanning the AFM outputs transistor-transistor-logic (TTL) pulses at times when a topography pixel is acquired. The demodulated samples are accordingly registered at these pixel times. To control the relative intensity of the tip-scattered light and the light in the reference arm, a gold mesh with square apertures (25 μm aperture size, 9 μm gold width, Precision Eforming LLC, USA) was placed in the beam as attenuator. The gold mesh attenuator has the advantage of being dispersion-free which is beneficial especially for the broadband access of the tip-scattered light (*vide supra*).

A different approach for a periodic phase modulation is the use of a PEM in the reference arm. A PEM consists of a crystal (ZnSe for the mid-IR) which is attached to a piezo actuator.

The refractive index $n = n_0$ of the unstrained crystal is isotropic. The crystal is designed such that the actuators excites an eigenmode of the crystal which has typically a frequency of tens to hundreds of kHz (∼50 kHz, Series II/ZS50, Hinds Instruments/Acal BFi Germany GmbH). Applying anisotropic strain to the crystal along the one axis (y axis in Fig. 3.6b) leads to a modulation of the refractive index along that axis (y-axis) but leaves the refractive index along the unstrained axis (x-axis) unaffected.[129] The resulting refractive indices can be written as

$$\begin{aligned} n_x(t) &= n_{x,0} \\ n_y(t) &= n_{y,0}\left[1 + \delta \sin(2\pi M t)\right] \end{aligned} \tag{3.2}$$

where δ is proportional to the maximal applied strain. If using linearly p-polarized light (along y axis) the phase will be retarded periodically.

In the current setup this type of phase modulation is realized. An additional polarizer in front of the detector selecting p-polarized light helps reducing circularly polarized contributions in the detected light. Due to the 20-fold increase in modulation frequency, the imaging speed can be increased accordingly (Sec. 4.2).

3.5.3 Broadband Nano-Spectroscopy

To access spectral resolved information from the tip scattered light the light source is replaced by an broadband emitting fs-laser system based on difference frequency generation (DFG) (Par. 3.5.4) and the reference arm is modified as depicted in Figure 3.7. The light in the reference arm is guided via a gold plated retroreflector (38.1 mm Diameter, Newport Spectra-Physics GmbH, Germany) which is placed on a voice-coil drive (V-524, Physik Instrumente (PI) GmbH & Co. KG, Germany) to a folding mirror. This construction has the big advantage that any shear or tilt occurring during the mirrors displacement does not affect the alignment of the interferometer.[50] As described earlier, an interferogram can be acquired by varying the relative optical path length between the tip and reference arm and subsequently Fourier-transforming the sampled data (Sec. 2.1.4). In order to sample the IR interferogram correctly, the relative retardation is read out by an auxiliary HeNe interferometer. For correct sampling of the interferogram, the IR radiation is demodulated by the LIA at different harmonics (n = 1..4) and the HeNe signal is simultaneously digitized by auxiliary inputs of the LIA. This ensures that both interferograms are sampled at the same times. Once the interferogram is digitized, they are both interpolated and the zerocrossings of the HeNe interferogram are determined. The IR interferogram is then constructed from the values at the found zerocrossings. This ensures that the retardation between all points in the IR interferogram are equidistant. It is important to note that for this procedure both interferograms need to be sampled at a frequency f_S which is at least 10 times the HeNe zerocrossing frequency.[50] The sampled IR interferogram is then post-processed as follows (see Sec. 2.1.4):

1. Search for center burst.
2. Cut Interferogram symmetrically around the center burst.
3. Apply phase correction to shift the point of zero retardation (and maximal interference) to center.
4. Multiply with suited apodization (3-term Blackman-Harris).
5. Append zeros at either end for smoother appearance.
6. Fourier-transformation.
7. Average resulting spectrum with its complex conjugate.
8. Subtract a linear base line if necessary.

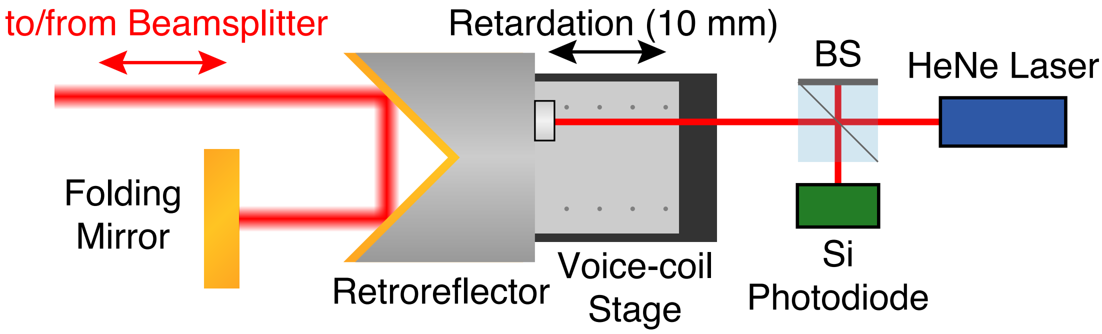

Figure 3.7 The light guided to the movable (mounted on a voice coil stage) by a retroreflector. The position is read out by a auxiliary HeNe-interferometer. (BS: beamsplitter cube)

3.5.4 Light Sources

Quantum Cascade Laser For single-frequency imaging *s*SNOM a quantum cascade laser (QCL)[130] is used as a light source. Those lasers were shown to be of high relevance for the progress in mid-IR *s*SNOM applications.[44,131–135] For interrogating the amide I region, a tunable external cavity QCL emitting ~200 mW in the range of 1580-1720 cm^{-1} was installed (Daylight Solutions, USA). The well collimated beam with TEM_{00} mode profile (M^2 ~1.2) with spectral width of ~0.01 cm^{-1} ensures that the incident light can be well focused on the tip. The laser was operated at maximum output power to achieve an optimum signal-to-noise ratio (SNR).[136] A power of 200 mW would by far saturate the detector or induce light damage on the sample. Thus, the power was attenuated by a pair of polarizes of which one was fixed in a rotating mount.

Broadband Difference Frequency Generation The broadband source used in this work is a commercially available femtosecond (fs) fiber laser (neaSpec GmbH, Germany).[137,138] It is based on DFG in a GaSe crystal from two Er fiber lasers (Fig. 3.8a). One of the fs pulse trains with a repetition rate of ∼ 80 MHz centered at 1.55 μm is fed into a nonlinear optical fiber which generates a super continuum from ∼1.7 - 2.3 μm. The continuum and the original 1.55 μm pulses are combined and focused into the nonlinear GaSe crystal which results in generation of pulses ranging from ∼4.5 - 16 μm via DFG. The chirp of the continuum pulse determines the center frequency of the generated IR continuum.[139] The orientation of the GaSe crystal relative to the combined beam and delay between the two pulses is used to optimize the output power of up to 2 mW.

Figure 3.8b shows the available spectral regions recorded when the free space output is coupled into an Vertex 80V FTIR spectrometer (Bruker Optik GmbH, Germany). There are five different tuning ranges (A-E) available which cover the whole mid-IR fingerprint region from.

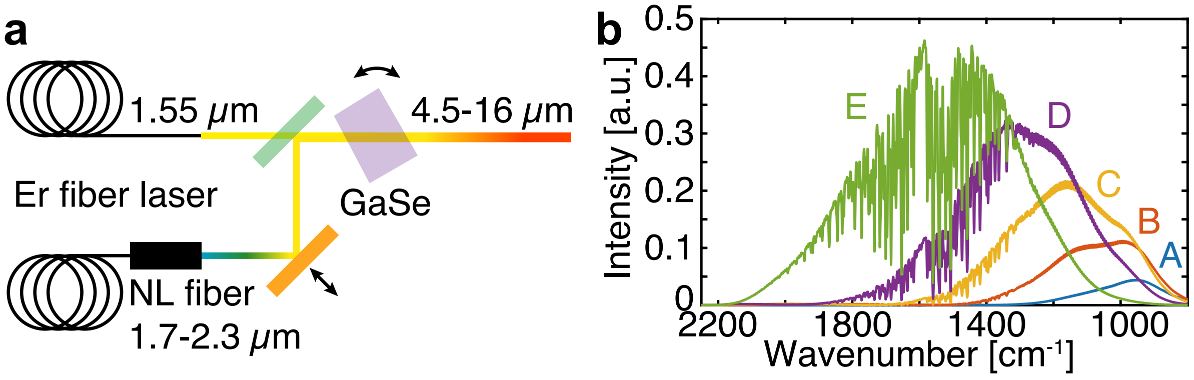

Figure 3.8 (a) Schematic layout of the DFG laser system as described in ref.[138] **(b)** Relative spectral output by the DFG laser system when fed into a conventional Vertex 80V FTIR spectrometer. The laser can be tuned to the different ranges A-E. The spectra are limited by the detector response on the lower frequency side.

3.5.5 Sample Preparations for AFM and sSNOM

Purple membranes (PMs) are patches in the plasma membrane of *Halobacterium salinarum* (see next paragraph). They are expressed when these archeabacteria grow under low oxygen tension. The patches are filled with the retinal protein bacteriorhodopsin (bR) which is a light-driven proton pump.[140] The 26 kDa protein consists of seven transmembrane α-helices with the retinal covalently linked to a lysine residue (Lys216) via a protonated Schiff base.[141] The bound retinal gives rise to a strong absorption around 560 nm which causes its characteristic purple color.[142] bR is arranged in a hexagonal crystalline lattice in these patches.[143] PM is already well known since the 1960s and target to a variety of different studies including electron microscopy, X-ray diffraction, neutron scattering and in particular vibrational spectroscopy[144–146] and scanning probe microscopy[143,147–149] as well as their combination.[44,45,135]

Purified samples were generously provided by AG Schlesinger (Freie Universität Berlin, Germany) at concentrations of ∼5 mg/ml. Individual patches were adsorbed on template-stripped Au (TSAu) or silicon from a dilute solution containing ∼50 μg / ml in buffer containing 10 mM 2-amino-2-hydroxymethyl-propane-1,3-diol (Tris), 300 mM KCl at pH 7.8 for 10 - 60 min.[150] The substrates were subsequently rinsed with Milli-Q water and dried under ambient conditions.

Halobacterium salinarum is an extreme halophile which requires salt concentrations of more than 2 M NaCl or KCl to survive.[151] Thus, preparation of dry samples of *halobacteria* copes with growth of salt crystals. Samples suited for AFM studies could be obtained by controlling the process of drying and crystallization: typically 1 ml of *H. salinarum* in growth medium with an optical density of $OD_{600} \sim 1$ was spun down at 2000 relative centrifugal force (rcf) for 10 minutes at 4°C. The supernatant was discarded and the cells resuspended in 100 μl of [4.3 M NaCl + 80 mM $MgSO_4$ + 10 mM tri-sodium citrate + 27 mM KCl] at pH 7.0. 5-10 μl were added to a ∼5x5 mm^2 TSAu or silicon (Si) substrate and directly covered with the flat face of a polycarbonate filter membrane (PC MB BL 25mm, 0.2 um B, Whatman, GE Healthcare Europe GmbH, Germany). The sample was stored under ambient conditions for several hours until all water evaporated. Lift off of the filter membrane removed sufficiently salt that the dried archaea were exposed and accessible to the AFM tip. Prior to AFM or sSNOM studies, all samples were checked by an optical microscope equipped with a x20 objective and regions of interest selected. Two strains, L33 and S9 of *Halobacterium salinarum* (*H. salinarum*), were used to prepare such samples. L33 does not overexpress bR in the form of PM whereas S9 is genetically modified to do so.

3.5.6 Imaging of Magnetic Domains via the ANE

As described in Section 2.4, a temperature gradient can generate an EMF, V_T, in a ferromagnetic sample perpendicular to the plane which is spanned by its magnetization and the temperature gradient. In order to generate the EMF locally we utilized a gold coated AFM tip (tip radius r $\sim$ 30 nm, tapping amplitude Δz = 50 nm) which is illuminated by focused IR radiation from a QCL ($P \sim$50 mW, $\tilde{\nu}$ = 1661 cm^{-1}, Fig. 3.9). The near-field induced local temperature gradient was periodically modulated by the dithering tip. The thermal EMF induced in the magnetic device was fed into a LIA and demodulated at the tips resonance frequency Ω. The output of the LIA is multiplied by $2\sqrt{2}$ to yield peak-to-peak values. Thermal EMF maps were acquired by scanning the nanometric heat-source across the magnetic device and registering V_T at every position of the tip relative to the sample.

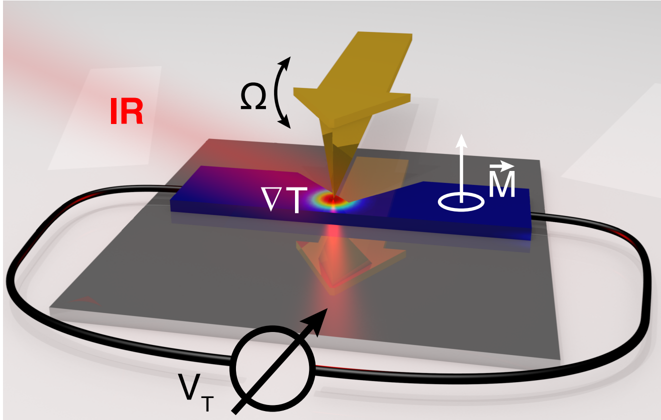

Figure 3.9 Sketch of the near-field induced magnetocaloritronic imaging. A gold plated Si tip oscillates at its resonance frequency Ω above the magnetic device. IR radiation of a QCL is focused on the tip and generates via its near-field a nano heat-source. The EMF generated is demodulated at Ω and registered during the tip is scanned across the wire.

The 1 μm wide and 60 μm long microbar with a central triangular constriction was defined by EBL into PMMA. The magnetic wire was built up by multilayers of Ta/Pt/Co/AlO$_x$ (3 nm / 3 nm / 0.6 nm / 2 nm) by DC magnetron sputtering on a thermally oxidized silicon substrate providing a perpendicular magnetic anisotropy.[152] A 500 nm notch is embedded in the center of the magnetic wire which acts as a pinning center for magnetic DWs. Initially the bar had a DW pinned to that center by application of an external magnetic field.[153]

The magnetic multilayers were kindly prepared by Murat Cubukcu(Cavendish Laboratory, University of Cambridge, Cambridge, UK) and Dr. Joerg Wunderlich (Hitachi Cambridge Laboratory, Cambridge, UK and Institute of Physics ASCR, Praha, Czech Republic).[104]

4

Results and Discussion

4.1 Surface-enhanced spectroscopy on ensembles of biomolecules

Within this thesis a new facile method for reproducible preparation of substrate for surface-enhanced infrared absorption spectroscopy (SEIRAS) was established. This method is based on nano-stencil lithography (NSL) using commercially available grids commonly used in cryogenic-TEM. The morphology and topography of the produced disc antenna arrays (DAAs) is first investigated and linked to spectroscopic characterization. Their spectral response is compared to theoretical prediction made by finite-difference time-domain (FDTD) and grating theory. The applicability of SEIRAS in the field of life science is demonstrated by two different types of samples and experimental conditions. First an *in-situ* pH titration of a self-assembled monolayer (SAM) of 4-mercaptobenzoic acid (4-MBA) will be presented. High mechanical stability of the created SAM will be inferred from the pH-dependent spectral characteristics supported by density functional theory (DFT) calculations. Second, light-induced difference spectra of sensory rhodopsin II from *Natromonas pharaonis* (*Np*SRII) will be presented.

Parts of the results were acquired together with Dr. Hirofumi Seki (Toray Industries Inc., Japan), discussed with Dr. Kenichi Ataka (Freie Universität Berlin, Germany) and published in ref.[121]

4.1.1 Topographic and Spectroscopic Characterization of Disc Antenna Arrays

Optical microscopy served as an initial quality control of the created DAAs. Figure 4.1a shows an exemplary photograph of a DAA substrate. The colorful refraction is an indicator for a proper periodic alignment of the gold discs. In some preparations the strength of the refraction was heterogeneous. This heterogeneity can be explained by a non-uniform distance of the holey carbon film to the CaF_2 which potentially leads to blurring of some individual arrays (cf. 4.1.1). Micrographs of different individual arrays in Figure 4.1b-e show no visible heterogeneity over the whole structured area of $\sim$5 mm^2. Only few arrays (mostly on the rim) are defective by scratches originating from the TEM-grid removal or just blank due to a ruptured carbon film before gold deposition. From the micrographs an average area of 7991± 27 μm^2 can be inferred (A.3). This area will later enter the estimation of the EF (Sec. 4.1.2).

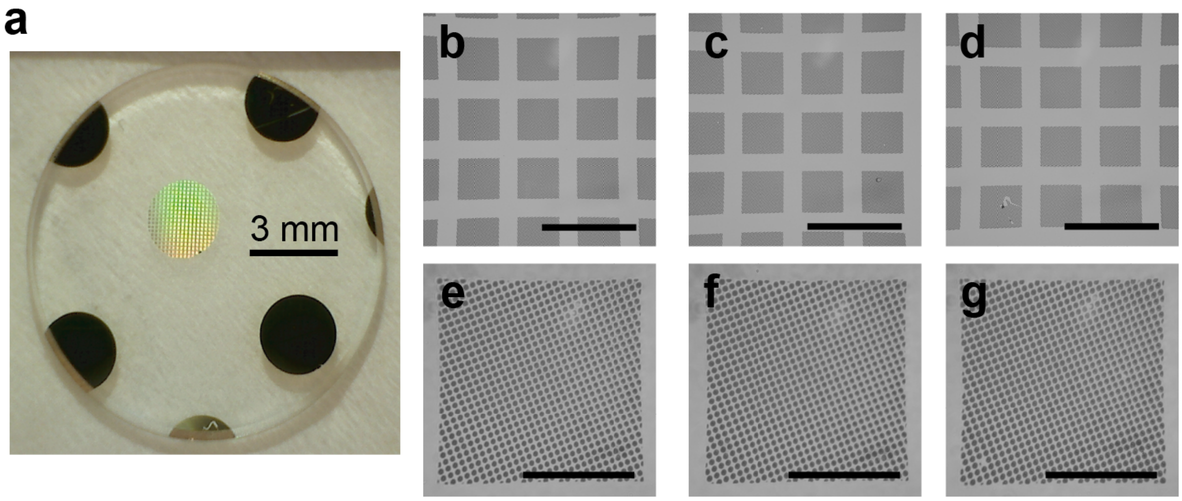

Figure 4.1 **(a)** Photograph of a DAA **(b-d)** Micrographs of different representative locations of a DAA (x20 objective, scale bar: 200 μm). **(e-g)** Zoom-in of typical individual DAAs (x100 objective, scale bar: 50 μm).

AFM To characterize the morphology of the DAAs more precisely AFM topographies were acquired on five different locations of one DAA (Fig. 4.2b-f). The average height of the antennas of 50.4 ± 3.2 nm (obtained by histogram analysis of the AFM topographies) is well within the thickness of 50 nm monitored by the quartz crystal balance during evaporation. To ensure a uniform shadow of the TEM grid, the samples were mounted above the gold boat which is mounted on one side of the chamber. The calibration of the quartz-crystal balance, however, was done by an evaporation placing the substrates in the center of the evaporation chamber.

As intended the shape of individual discs is circular with minor deviations. The average diameter of the antennas is 2.510 ± 0.006 μm. The increased diameter compared to the apertures of the TEM grids (2 μm) can be related to the distance of the carbon film to the substrate. As outlined in Figure 3.1b, a finite source produces bigger structures by a half-shadow effect. This is the reason for the smeared out edges, as well.[75,154] The blurriness slightly varies between the different DAAs. The edges are consistently blurred in arrays 1, 2, 4 and 5 whereas in array 3 the edges are slightly stronger smeared out. These discs are in average 121 nm (9.7 %) bigger compared to the other DAAs (see A.3, measured with ImageJ[155]). This is due to varying distance between grid and substrate and the finite size of the gold source. This rather small deviations in morphology also affect the spectroscopic results. The reflectance spectra (Fig. 4.6a) of the sample on which the topographic study was carried out shows strongest variation on location 3 (Fig. 4.2d). This spectrum is marked by a † in Figure 4.6a. The resonance of these antennas is shifted to lower frequencies by ∼150 cm^{-1}. The downshift of the resonance frequency qualitatively corresponds well with the effective larger dimensions of the blurred antennas.[49,55] The blurring effect can be minimized by choosing a smaller boat or crucible for evaporation or using electron-beam evaporation.

To determine the effective surface of the gold compared to the projected area of a DAA the average surface area was calculated using Gwyddion (cf. A.3). The relative gold surface area is $\eta^{\mathrm{Au}} = 0.54 \pm 0.03$.

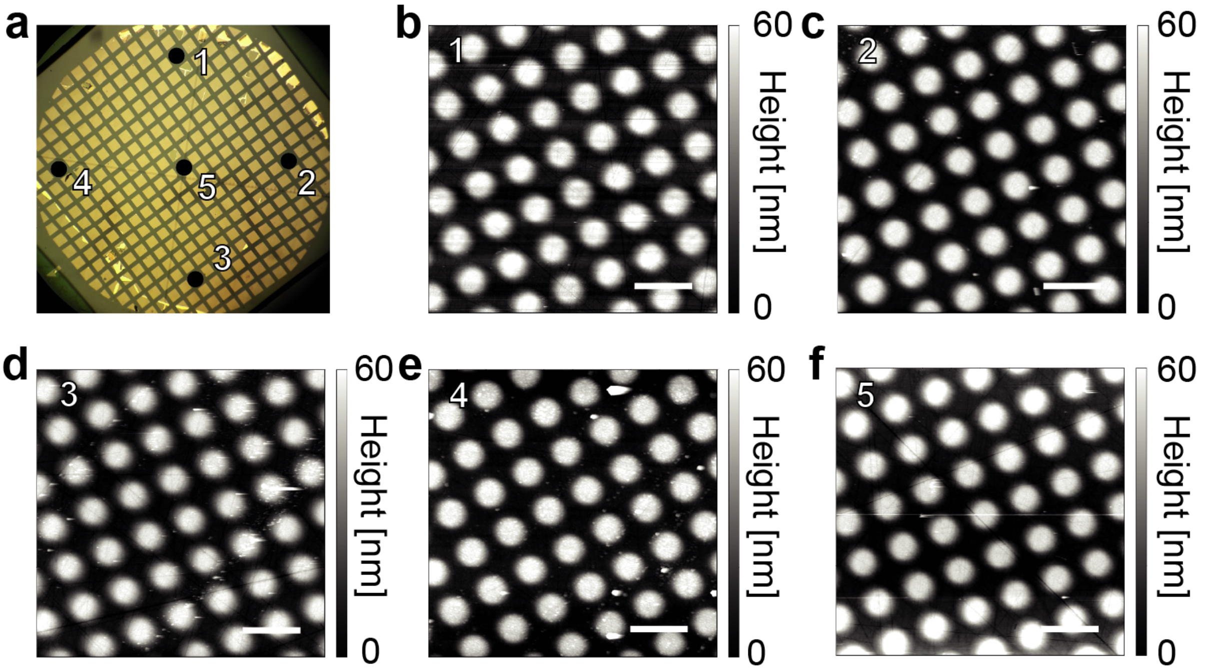

Figure 4.2 (a) Micorgraph of a DAA. Positions of the AFM topographies are indicated by dots. **(b-f)** AFM topographies of the positions indicated in **(a)** (scale bar: 4 μm).

FTIR To address spectroscopic different arrays the DAAs were studied with a FTIR-microscope (Sec. 3.2). Figure 4.3 shows reflectance and transmittance spectra acquired on 10 different individual arrays in a top (antennas facing the collection objective) and bottom (antennas averted from the collection objective) geometry. The spectra are almost identical in their respective geometry which indicates good uniformity of the DAAs. The reflectance spectra (Fig. 4.3a) show a strong resonance in both geometries (top and bottom). A global maximum of reflectance is observed at ∼1800 cm^{-1} and a second local maximum at ∼2200 cm^{-1}. The main difference between spectra of the two configurations is a offset. This offset can be attributed a different phase shift in the two configurations.[156] Light reflected on the CaF_2/air interface in the top configuration experiences a shift of π as well as on the resonant structures. In contrast, the phase shift in the bottom configuration is π on the antennas and 0 on the CaF_2/air interface. This leads to constructive interference for the top configuration and destructive for the bottom one which induces the offset.

The transmittance spectra (Fig. 4.3b) exhibit the same resonances as the reflectance spectra. The spectra lack the relative offset since the light passes CaF_2 only once in both top and bottom geometries.

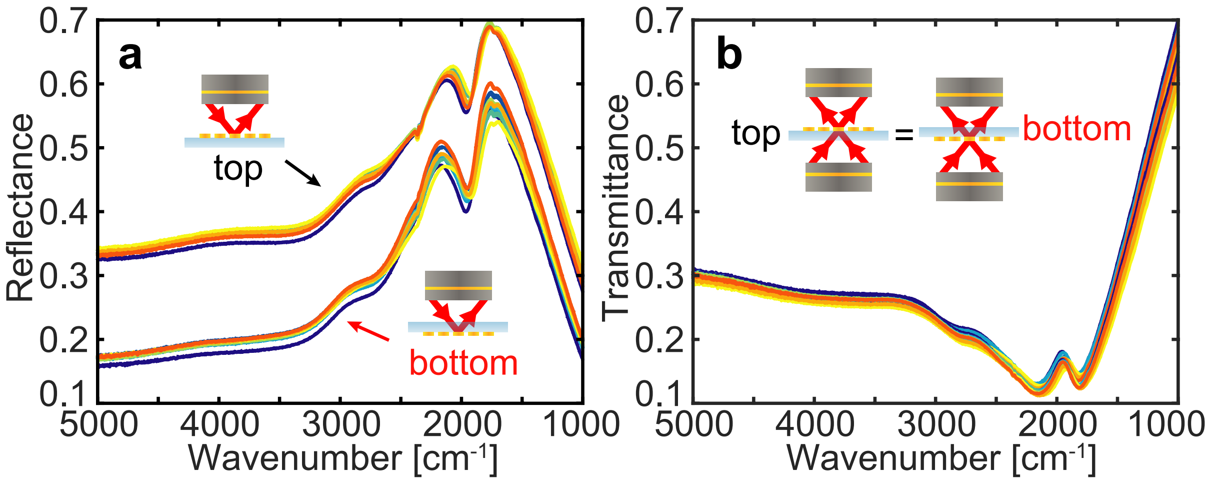

Figure 4.3 (a) FTIR reflectance and **(b)** transmittance spectra of various individual arrays on a DAA sample. DAAs were facing the upper objective (to detector) or averted from it (see insets).

Angle-resolved absorbance spectra were acquired in a FTIR spectrometer without the use of focusing optics to corroborate the origin of the split resonance (Fig. 4.4). An aperture ensured that only light reached the detector which passed DAAs (the diameter of the focus of a conventional spectrometer is in the order of the size of one DAA sample). Additionally, a polarizer was mounted in front of the sample to either collect spectra with s- or p-polarization (Fig. 4.4a). The resulting spectra (Fig. 4.4b) show a progressive splitting of the resonance with increasing tilt angle in both s- and p-polarization. Figure 4.4c-d show a heatmap representation of the spectra in Figure 4.4b. The solid and dashed lines in both maps indicate the grating transition frequencies (see Sec. 2.2.4 and Eqn. 2.22). Different grating transition frequencies are plotted for different momenta transferred to the photons at the gold/CaF_2 interface by

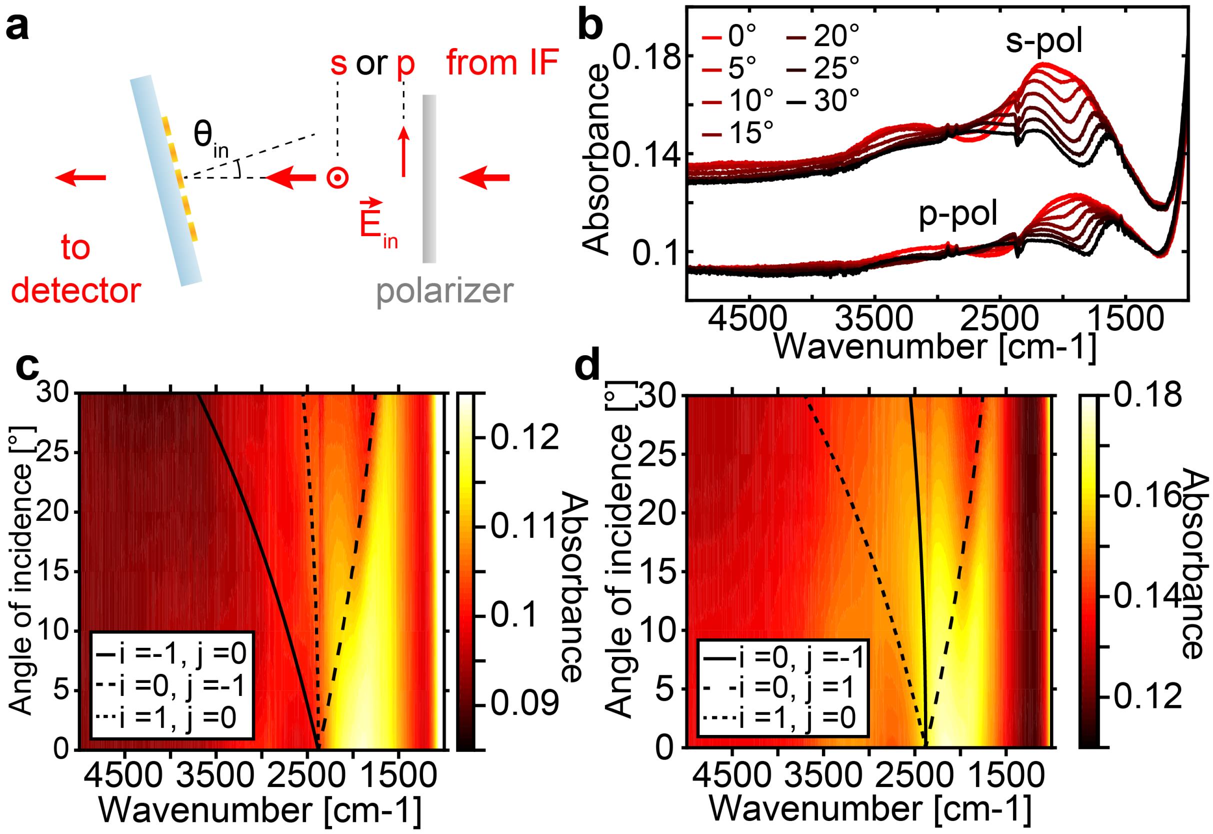

Figure 4.4 **(a)** Sketch of the geometry used for acquisition of the tilt series absorbance spectra. **(b)** FTIR absorbance spectra at different tilt angles with p- and s-polarization. Spectra are offset such that the absorption of CaF_2 (< 1200 cm^{-1}) overlaps. **(c & d)** Heatmap representation of the absorbance spectra vs AOI in p- **(c)** and s-polarization **(d)**. The lines represent the grating transition frequencies for arrays with a periodicity of 3 μm in x- and y-direction with the respective grating momenta at the gold-CaF_2 interface in x- (i) and y-direction (j).

the periodic grating with periodicity $p_x = p_y = 3\mu$m. The lines for the two lower transition frequencies match qualitatively the frequency of the angle-dependent absorption maximum. It is known that the i = -1,j = 0 (p-polarization) and i = 0, j = -1 (s-polarization) grating order affects the resonance strongest, thus, shifting the maximum absorbance according to the grating transition frequency.[71,82] In addition to the frequency shift, the resonance is enhanced as soon as the antenna resonance frequency matches the grating transition frequency. In this case all antennas will oscillate in-phase and the electromagnetic field in the hot spots will be further enhanced by one order of magnitude.[82] On the other hand, the coupling to incident radiation is reduced by detuning the collective resonance frequency from the intrinsic antenna resonance frequency by very high AOIs. This is reflected by the decreased absorbance at higher AOIs in Figure 4.4c,d. The micro-FTIR spectra can be approximated by an average of the s- and p- polarized spectra in the respective angle range (10°-24°). This qualitatively explains the double-maximum feature of the spectra in Figure 4.3.

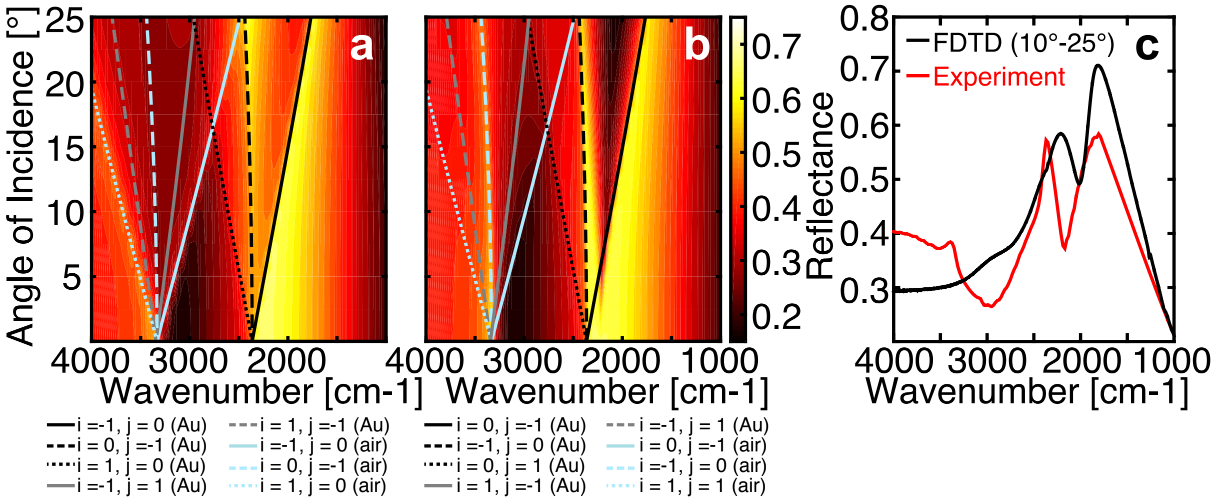

Figure 4.5 (a, b) FDTD reflection spectra of the DAA as contour in p-**(a)** and s-polarization **(b)**. The solid and dashed lines represent the grating transition frequencies for arrays with a periodicity of 3 μm in x- (i) and in y-direction (j). The grating transition frequencies were corrected to match the distorted frequency from the FDTD simulation (see Sec. 2.2.4). **(c)** Average simulated reflection spectrum (10-25°, black trace) and experimental reflectance spectrum (red trace).

Finite-Difference Time-Domain (FDTD)[79] Simulations were performed as a complimentary method to understand the origin of the micro-FTIR spectra's shape (Sec. 2.2.4 & Sec. 3.3).The simulated reflectance spectra are displayed as a contour in Figure 4.5 (a: p-polarization, b: s-polarization). As stated earlier in Sec. 2.2.4 the method by which different AOIs are simulated in FDTD leads to an frequency-dependent AOI. This means that the reflection spectra at a nominal AOI are mixtures of different AOIs. It was shown that it is possible by post-processing to disentangle this frequency dependence by running multiple simulations with a high AOI resolution.[71] Due to lack of computational power this was not done here. Despite that, the simulated and experimental spectra (Fig. 4.4) correspond well. To compare these spectra to analytically calculated grating transition frequencies, the grating transition frequencies were corrected for their AOI dependency (Sec. 2.2.4). Qualitatively the simulated reflection spectra and the corrected grating transition frequencies match quite well and show the same trend as the experimentally derived angle-dependent absorbance spectra in Figure 4.4c-d. An average reflectance spectrum was calculated from the FDTD spectra at AOIs between 10° and 25° to account for the NA of the objective used in the micro-FTIR measurements. The average FDTD spectrum shows the same splitting of the main resonance and resembles well the frequency of their maxima.

4.1.2 Characterization of Vibrational Enhancement

In the following section the enhancement factor (EF) will be determined on the example of 4-mercaptobenzoic acid (4-MBA), compared to values present in literature and, finally, critically discussed.

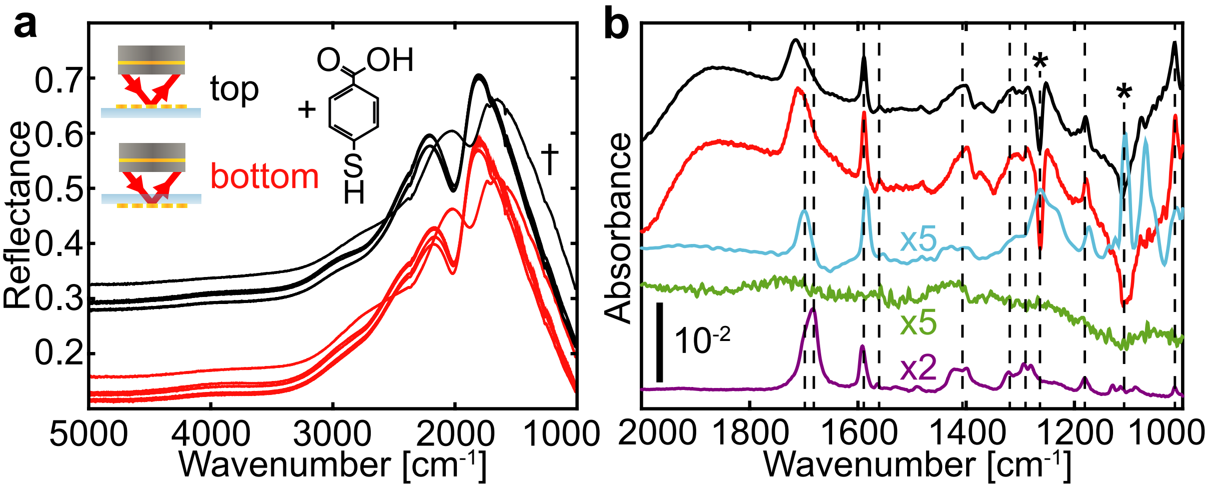

Figure 4.6 (a) FTIR reflectance spectra of the locations indicated in Fig. 4.2a. DAAs were facing the upper objective. The spectrum marked with a † corresponds to the blurred array 3 (Fig. 4.2d). Figure adapted from[121] (b) Representative absorbance spectra obtained in top (black) and bottom (red) geometry from the 4-MBA-SAM. Si-based SEIRA spectrum of 4-MBA (cyan). Spectrum of an unstructured, flat gold interface coated with 4-MBA (green) and ATR-FTIR spectrum 4-MBA dried from acetone (purple).

4-mercaptobenzoic acid (4-MBA) absorption and EF determination To acquire absorbance spectra of a DAA with a well defined density of molecules, a self-assembled monolayer (SAM) of 4-MBA was established on the DAAs (Sec. 3.1) and spectra were recorded in top (black traces) and bottom (red traces) geometry on various positions (Fig. 4.6a). Note that the spectrum marked with † (corresponding to array 3 in Fig. 4.2d) is red shifted and distorted due to stronger blurred discs as discussed above. The spectra of Figure 4.6a were referenced to spectra recorded before the SAM deposition, resulting in an absorbance spectrum for each position. The black and red trace in Figure 4.6b corresponds to a representative absorbance spectrum of the 4-MBA SAM. However, qualitatively the enhanced vibrational bands are identical to each other among the different positions (data not shown). All major vibrational bands are present compared to a ATR-FTIR spectrum of 4-MBA (Fig. 4.6b, purple trace). The negative bands marked with an asterisk are due to a temporary contamination of the evaporation chamber by poly(dimethyliloxane) (PDMS)[157] which is desorbed from the surface upon 4-MBA adsorption. The relative intensity of the bands is strongly influenced by the orientation of their transition dipole moment relative to the surface (see Sec. 2.2.3). The intensity ratio of ν(C=O) (1700 cm^{-1}) and the most prominent ring mode 8a (1588 cm^{-1}) in the DAA spectra are almost equal whereas in the ATR spectrum the ν(C=O) is twice as intense as the latter. The transition dipole moment of the 8a ring mode points along the C_{2v} symmetry axis of the molecule and is well aligned with the electric field assuming the molecules are tilted by $\sim 35^\circ$ off the surface normal (an average angle of the bridge-hcp and bridge-fcc was assumed).[158] Within this assumption, the transition dipole moment of the ν(C=O) mode would be tilted by $\sim 50^\circ$ relative to the surface normal and is consequently less probed as imposed by the surface selection rule (Sec. 2.2.3). Most of the other strong bands are due to vibrational modes of the ring which also exhibit a transition dipole moment along the symmetry axis of 4-MBA (see Tab. A.4 for a comprehensive assignment). The apparent absorbance of 4-MBAs bands in the DAA spectrum gets relatively more intense with decreasing wavenumber compared to the ATR-FTIR spectrum. Although, being less efficiently probed by the antenna – the vibrational mode gets spectrally more separated from the antennas dipole mode[78,159] – it gets more enhanced due to the enhancement factor scaling with λ^3.[57] Compared to a Si prism based SEIRA spectrum of 4-MBA (Fig. 4.6b, blue trace), the apparent absorbance in the DAA spectra is almost an order of magnitude stronger. An unstructured flat gold surface coated with a 4-MBA SAM shows no specific vibrational bands. Due to the increased effective refractive index of the antennas surrounding upon binding of the SAM, the resonance is slightly shifted to lower frequencies.[28,49] This adds a superimposed non-linear baseline to the absorbance spectrum. It was removed by first smoothing each spectrum by a broad moving average filter (width 400 cm^{-1}) and subtracting the smoothed spectrum from the non-smoothed spectrum (see Sec. A.4).

We have chosen four different modes specific to vibrations of the phenyl ring of 4-MBA to compute the EF over a broad spectral range (1600-1000 cm^{-1}, see Sec. A.2) under ambient conditions after establishing a SAM and in liquid environment after *in situ* deposition of the SAM, respectively. To estimate the EF of each of this modes, the ratio of the apparent absorbance per molecule $\tilde{A}^i_{\mathrm{SEIRAS}}$ from the SEIRAS experiment and $\tilde{A}^i_{\mathrm{ATR}}$ from an bulk experiment in ATR configuration was computed.

$$EF^{\mathrm{i}} = \frac{\tilde{A}^{\mathrm{i}}_{\mathrm{SEIRAS}}}{\tilde{A}^{\mathrm{i}}_{\mathrm{ATR}}} = \frac{A^{\mathrm{i}}{}_{\mathrm{SEIRAS}}}{\rho^{\sigma}{}_{\mathrm{SEIRAS}}\eta^{\mathrm{Au}}\sigma^{\mathrm{Au}}} \cdot \frac{\tilde{d}^{\mathrm{i}}_{\mathrm{p}}\sigma^{\mathrm{ATR}}c_{\mathrm{ATR}}}{A^{\mathrm{i}}{}_{\mathrm{ATR}}} \tag{4.1}$$

$\tilde{A}^{\mathrm{i}}_{\mathrm{SEIRAS}}$ can be easily calculated from the apparent absorbance extracted from Figure 4.6b divided by the amount of molecules bound to the gold surface. Here $\rho^{\sigma}{}_{\mathrm{SEIRAS}}$ = (7.4 ± 0.2) 10^{-10} mol cm^{-2} is the density of benzoic acid chemisorbed to gold taken from literature[160] as an estimate for the density of 4-MBA, η^{Au} the relative surface area of the gold antennas deduced from AFM topographies (see Sec. A.3) and σ^{Au} the area of one individual DAA measured by optical microscopy (Sec. A.3). $\tilde{d}_{\mathrm{p}}^{\mathrm{i}}$ is the effective penetration depth at the wavenumber of each mode i, σ^{ATR} the area probed in the ATR experiment and c_{ATR} the concentration of 4-MBA.

To determine the wavelength-dependent penetration depth $\tilde{d}_{\mathrm{p}}^{\mathrm{i}}$ at each selected vibrational mode in the ATR dilution series, a a linear scaling law was assumed:

$$\tilde{d}_{\mathrm{p}}^{\mathrm{i}} = \frac{\tilde{d}_p^{H_2O}\,\lambda^i}{\lambda^{H_2O}} \tag{4.2}$$

The well-defined absorption of the bending mode of water at 1640 cm^{-1} ($\lambda^{H_2O} = 6.098$ μm) served as a marker band for deriving the penetration depth $\tilde{d}_p^{H_2O}$ at this wavenumber. Therefore, the ATR crystal was totally immersed in liquid water to ensure that the evanescent wave exclusively probed H_2O. The effective penetration depth at this frequency was determined via Lambert-Beer's law. $A^{i}{}_{ATR}/c_{ATR}$ was determined from series of spectra in which the concentration of 4-MBA was varied (see Sec. A.2). Taking all this considerations into account we determined the following values for the EFs at the four different frequencies.

Frequency [cm^{-1}]	**Assignment***	**EF**$_{dry}$ [10^4]	**EF**$_{DMSO}$ [10^4]
1588	ring mode (8a)	4.1 ± 0.5	3.8 ± 0.4
1559	ring mode (8b)	3.5 ± 1.5	2.4 ± 1.1
1189	δ(C-O) & ring mode (9a)	6.5 ± 0.8	5.1 ± 0.6
1017	ν(C=O) & ring mode (1)	4.0 ± 0.6	2.4 ± 0.4

Table 4.1 EFs for four vibrational modes associated to the phenyl ring of 4-MBA. *For ring modes, the Wilson notation is used in brackets. ν: stretching mode, δ: bending mode.

The EFs are overall in agreement with ones reported for similar antenna based SEIRAS platforms produced by EBL[56,161,162] or DLW.[74] The orientation of the transition dipole moment of all four modes is similar but difficult to determine precisely *in situ*. This might lead to the significant difference among the EFs. However, a rather constant enhancement over the probed spectral range can be inferred from table 4.1. Due to additional damping of the antennas resonance by the DMSO, the enhancement of the SAMs vibrational modes is diminished. The reduced EFs derived in DMSO corresponds well to the observation made by Adato et al.[49]

Dependency of observed area Even though the EF is a common parameter given for SERS and SEIRAS structures in literature, its definition suffers fundamentally from robustness. A SAM of *Np*SRII (see 4.1.3) was adsorbed on a DAA to illustrate that. The effect of the detected

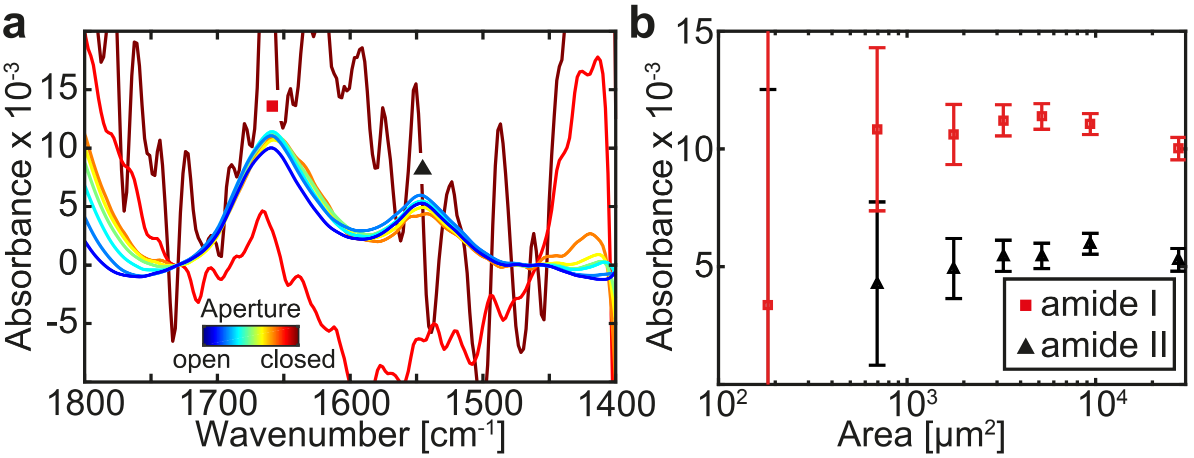

Figure 4.7 (a) Absorbance spectra of a DAA covered by a *Np*SRII-SAM at different aperture openings (indicated by the colorbar). Spectra were corrected for a linear baseline for clarity. **(b)** Absorbance of *Np*SRII bands vs observed area.

area on the enhancement was estimated by recording spectra on the same DAA while decreasing the probed area by IR-intransparent blades (Fig. 4.7a). The blue trace corresponds to a spectrum when the aperture was fully opened while the dark red one corresponds to a spectrum when the aperture was closed. The intensity of the amide I (red square) and amide II (black triangle) bands are displayed against the aperture area in a semi-logarithmic representation in Figure 4.7b. Interestingly, the enhancement is not dependent on the probed area. Closing the aperture leads to less photons detected by the MCT which interacted with the antennas and, thus, to an increase in noise. This observation rises the question about the correctness of the presented EFs. Simply decreasing the probed area increases the EF since the same absorbance corresponds to less probed molecules (see Eqn. 4.1). This makes the different EFs across different SEIRAS platforms barely comparable. However, the presented way of determining the EF is commonly found in literature.[28,62,163] There is just a very limited selection of suited FTIR microscopes and objectives available, which have common optical properties (e.g. focal length, NA, etc.). Thus, the probed area might be similar in different publications. This would make a comparison possible again but only when a microspectroscopic readout is employed. A different approach is to normalize the found vibrational signal enhancement to the density of observed antennas.[57] Yet, this prevents a comparison of chemically prepared percolated metal films with discrete resonant antennas.

4.1.3 Application to Self-Assembled Monolayers and Membrane Proteins

The application of SEIRAS in life science has delivered high quality spectroscopic information at lowest analyte amounts (~attomol).[55] To demonstrate reliable application of the DAAs in life science, we choose two model experiments: *in situ* spectroscopic analysis of a 4-MBA-SAM during its adsorption and subsequent pH titration and light-induced difference spectroscopy on a tethered retinal protein, *Np*SRII.

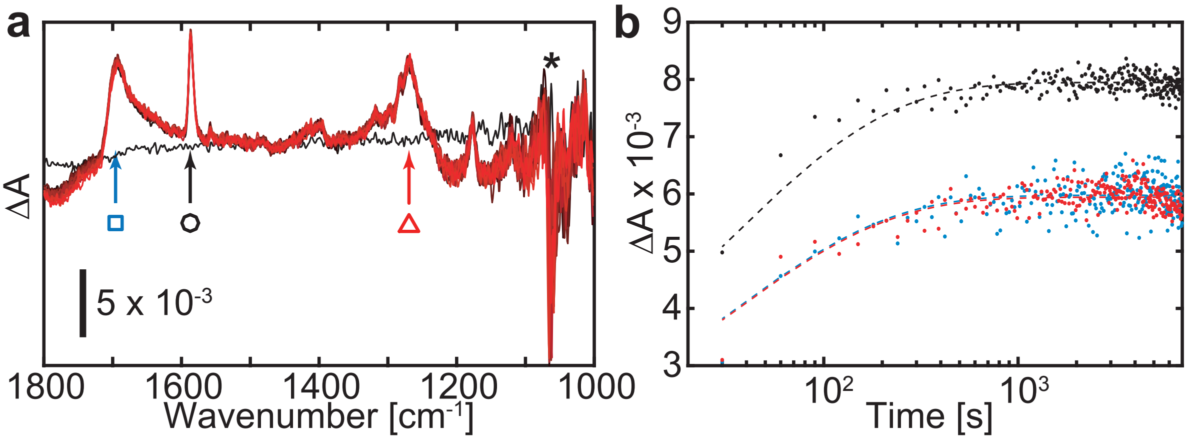

Figure 4.8 (a) Time-resolved FTIR spectra during adsorption of 4-MBA over 2 hours in DMSO. **(b)** Time evolution of the bands marked in **(a)**. The dashed lines indicate a Langmuir adsorption kinetic fitted to the data.

***In situ* adsorption and pH titration of 4-MBA** The process of adsorption of 4-MBA was followed spectroscopically (Fig. 4.8a) and the kinetics of the SAM formation was determined from plotting the absorbance of marker bands over time (Fig. 4.8b). The increasing coverage of 4-MBA leads to a slight baseline shift which is compensated for by a baseline correction (see Sec. A.4). The temporal evolution of the absorbance of three marker bands for the protonated 4-MBA (blue square: ν(C=O), black circle: 8a ring mode, red triangle: δ(C-O-H)) is depicted in Figure 4.8b. The non-exponential time dependency of the absorbance $A_i(t)$ of all three bands is best fitted with the following model[164]

$$A_i(t) = A_i^{max}\left(1 - e^{-(t/\tau)^{\alpha}}\right) \tag{4.3}$$

where A_i^{max} is the maximal absorbance at each band i, τ the time constant of the adsorbtion process and α a scaling factor. Global fitting of the three bands reveals a value for α = 0.49. According to literature a value of α = 0.5 can be attributed to a diffusion limited Langmuir-type adsorption of the molecules:[164,165] every particle eventually making contact to the surface adsorbs to it while the rate limiting step is diffusion of the molecules to the surface. As a result, the monolayer grows randomly to full coverage. The time constant was determined to be τ = 29 s. Thus, incubation for at least 2 hours was assumed to yield a fully covered SAM.

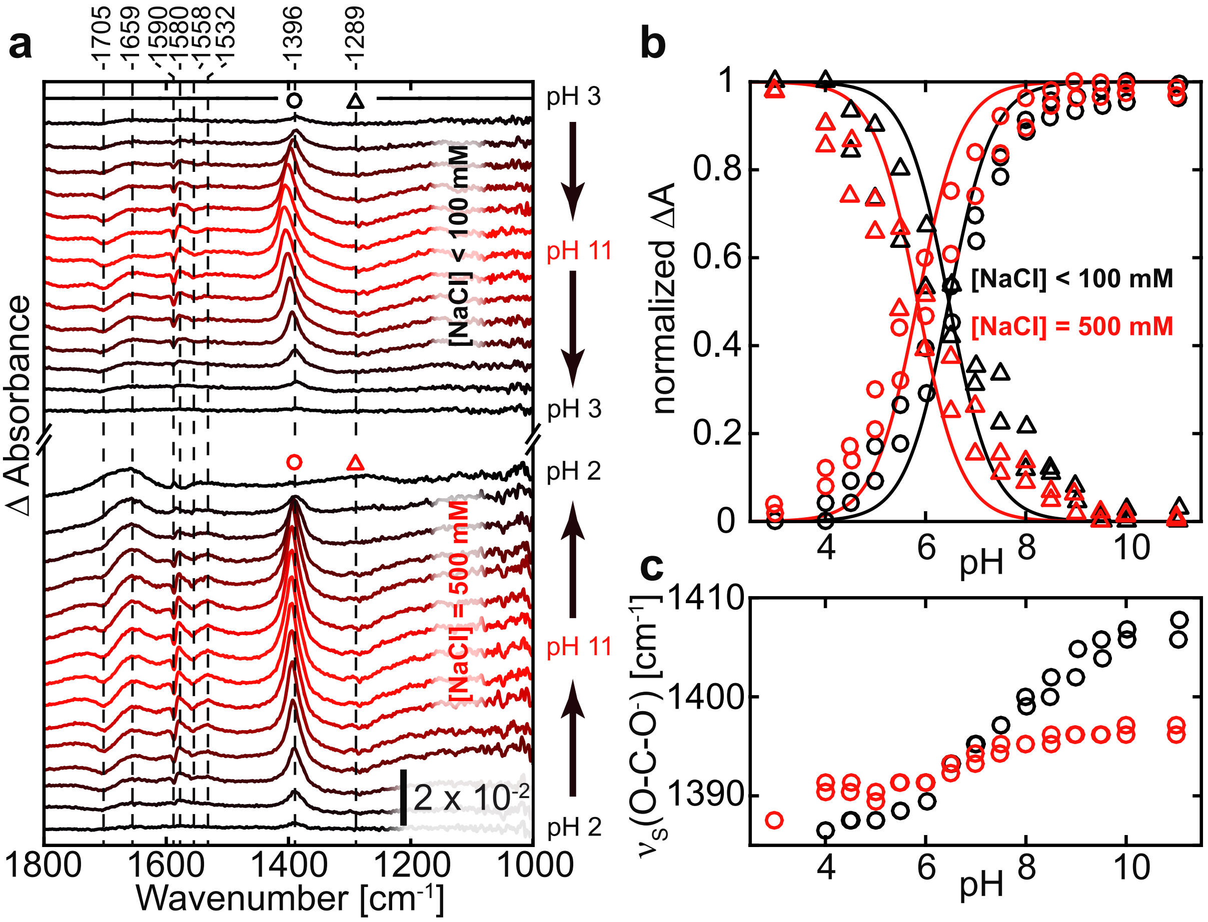

Figure 4.9 (a) SEIRA spectra of a 4-MBA-SAM adsorbed from DMSO in a buffered solution containing either [NaCl] $<$ 100 mM (upper panel) or [NaCl] $\cong$ 500 mM (lower panel) during pH titration. **(b)** Normalized amplitude of the symmetric $\nu_s(\mathrm{COO}^-)$ (○) and δ(C-O-H) (△) vs pH at [NaCl] $<$ 100 mM (black symbols) and [NaCl] $\cong$ 500 mM (red symbols). The solid lines represent a Henderson-Hasselbalch fit to the data. **(c)** Frequency of $\nu_S(\mathrm{COO}^-)$ vs pH. The color code is the same as in **(b)**.

The freshly prepared SAM was immediately used for *in situ* pH titration (see Sec. 3.1). The flow cell volume was flushed with buffer of a given pH and salt concentration before acquisition of different spectra (Fig. 4.9a). As a wide range of pHs is of interest to biological samples we covered pHs from 2 - 11. Three major difference bands can be assigned to 4-MBA: ν(C=O) (1705 cm^{-1}) and δ(C-O-H) (1289 cm^{-1}, △) decreasing and $\nu_s(\mathrm{COO}^-)$ (~1400 cm^{-1}, ○) increasing with increasing pH. The first two correspond to the protonated state of 4-MBA while the latter one to the deprotonated state. The antisymmetric $\nu_{as}(\mathrm{COO}^-)$ (~1589 cm^{-1})[21] is absent in these spectra because its transition dipole moment is oriented parallel to the surface and not enhanced. Increasing the solutions pH increases the probability of deprotonating the 4-MBAs carboxylic moiety. Titrating a bare DAA without 4-MBA-SAM yielded minor changes in the same spectral region (Fig. 4.11a). Decreasing the pH again shows reversible reprotonation of the SAM except for a slight change in the band at 1659 cm^{-1}. This could tentatively be assigned to a water band

(δ(H-O-H)) whose frequency is unusually high (bulk liquid water:δ(H-O-H) $\sim$1643.5 cm^{-1}).[166] The high frequency could indicate a stronger hydrogen bonding of interfacial water.[167] The residual water peak after titration indicates a reorientation or reformation of the hydrogen-bonding network of water at the SAM interface. A slight hysteresis between the intensities for increasing and decreasing pH can be found in Figure 4.9b. The origin of this hysteresis is not clear. Recording multiple spectra of the SAM after a pH jump did not show a significant change in the band intensities. This excludes that there is any kind of slow relaxation after a pH jump, which might induce a hysteresis. During pH titration the ν_S(COO$^-$) frequency (indicated by $\circ$) shifts up by $\sim$20 cm^{-1}, which can be diminished upon the addition of salt (4.9a, lower panel). This suggests electrostatic interaction between the negatively charged head groups of 4-MBA in its deprotonated state. Although carboxylic moieties don't show a significant Stark tuning[160] and the frequencies of the other bands are unaffected, the water hydrogen bonding network might be significantly altered with increasing degree of deprotonation. This is additionally supported by the band at $\sim$1659 cm^{-1} rising with the degree of deprotonation.

Figure 4.9b shows the normalized amplitudes of the two most prominent marker bands for the protonated (δ(C-O-H), $\triangle$) and deprotonated (ν_S(COO$^-$), $\circ$) state versus the solutions pH are displayed both under low (black symbols, [NaCl] $<$ 100 mM) and high salt concentration (red symbols, [NaCl] = 500 mM). It can be assumed that the amplitude ΔA of either band is directly proportional to the relative degree of the SAMs protonation ϑ(pH). Since 4-MBA is a monoprotic acid, the degree of deprotonation ϑ(pH) might be fitted by the Henderson-Hasselbalch equation:

$$\mathrm{pH} = \mathrm{pK_a} + \log_{10}\left(\frac{\vartheta}{1-\vartheta}\right) \tag{4.4}$$

The resulting fit is depicted as a solid line in Figure 4.9b with pK$_\mathrm{a}^{100mM}$ = 6.47 for [NaCl] $<$ 100 mM and pK$_\mathrm{a}^{500mM}$ = 5.84 for [NaCl] = 500 mM. The apparent pK$_\mathrm{a}$ is unusual high for 4-MBA compared to benzoic acid as a model compound, which has typically a pK$_\mathrm{a}$ around 4 in solution.[168] In addition, the titration curve spreads over a much wider pH range as typical for monoprotic acids. The upshift of the pK$_\mathrm{a}$ was previously observed in contact angle measurments on 4-MBA SAMs,[169] as well as, the wider spread of the titration curve on carboxyl-terminated SAMs.[170] It was attributed to electrostatic interactions of the moieties. Upon deprotonation, the surface gets negatively charged depending on the degree of deprotonation ϑ, which increases the local proton concentration at the interface. This leads to an additional energetic cost for further carboxylic moieties to deprotonate.[170] Consequently, the fit in Figure 4.9b assuming a monoprotic acid, is not quite perfect. The Henderson-Hasselbalch equation is only valid in dilute solutions, in which the individual acid and base molecules do not electrostatically interact. This is not the case for the carboxylates in the SAM. Nevertheless, a slight downshift of the apparent $\mathrm{pK_a}$ can be observed upon increasing salt concentration. The increased concentration of counter ions ($\mathrm{Na^+}$) screens the electrostatic interaction partially and leads to a $\mathrm{pK_a}$ closer to the bulk value. Borkovec et al. suggested a model in which the interaction between protonatable residues and the surrounding via an mean electrostatic field is accounted for by an additional term in the Henderson-Hasselbalch equation.[171,172]

$$\mathrm{pH} = \widetilde{\mathrm{pK}}_\mathrm{a} + \log_{10}\left(\frac{\vartheta}{1-\vartheta}\right) + \frac{\overline{E}\,\vartheta}{RT\ln(10)} \tag{4.5}$$

The additional term leads qualitatively to a less steep slope in the titration curve and, thus, to a higher apparent $\mathrm{pK_a}$, while the bulk $\widetilde{\mathrm{pK}}_\mathrm{a}$ of the molecule is well below.[172] In a densely packed SAM, this behavior can be easily understood by means of an additional electrostatic (energetic) penalty $\overline{E}$ for deprotonation. Introducing a negative charge in a fixed arrangement of negative charges makes deprotonation more unlikely at a certain pH.

Unfortunately, Equation 4.5 can not be solved for ϑ. However, a nonlinear least squares fit pH(θ) (the inverse function of Eqn. 4.5) was attempted to estimate $\overline{E}$ and $\widetilde{\mathrm{pK}}_\mathrm{a}$ (Fig. 4.10). Equation 4.5 clearly resembles the experimental data more accurately as the Henderson-Hasselbalch equation (Fig. 4.9b). The resulting parameters $\overline{E}$ and $\widetilde{\mathrm{pK}}_\mathrm{a}$ are listed in table 4.2:

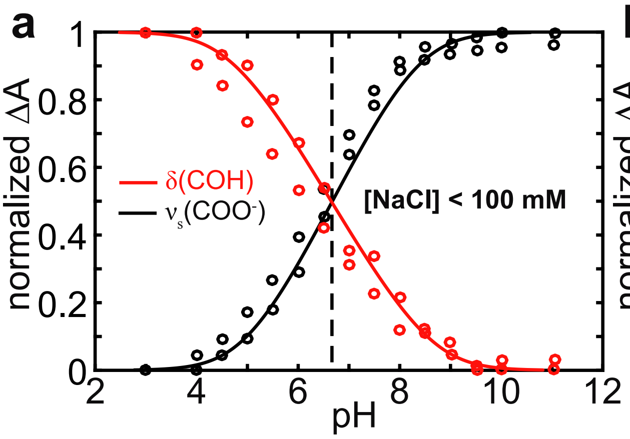

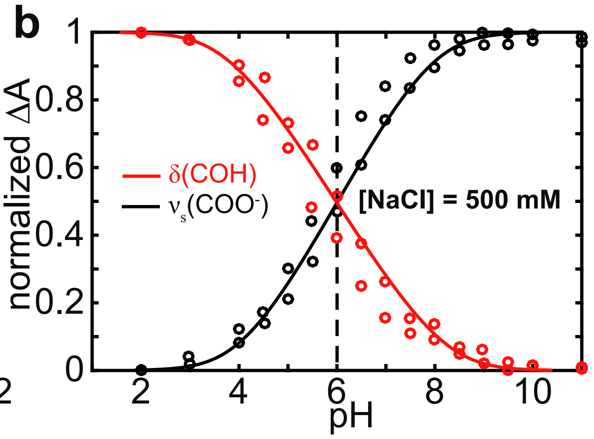

Figure 4.10 Titration curves form Fig. 4.9b (**(a)** [NaCl] $\leqslant$ 100 mM, **(b)** [NaCl] = 500 mM) fitted with eqn. 4.5. Fit results are summarized in Tab. 4.2.

The mean field contributions $\overline{E}$ don't change for both salt concentrations. The fit of the inverse function seemed to be very sensitive to the slope determining parameter $\overline{E}$. In consequence, $\overline{E}$ is affected by a large error. Although the unperturbed $\widetilde{\mathrm{pK}}_\mathrm{a}$ is the same within one salt concentration, the values deduced for different salt concentrations differ significantly: the

$\widetilde{\mathrm{pK}}_\mathrm{a}$ tends to decrease with increasing salt concentration. To exclude the hysteresis affecting the quality of the fit, the curves for increasing and decreasing pH were fitted separately and the resulting parameters were averaged (given in brackets in tab. 4.2). The apparent decrease of the found unperturbed $\widetilde{\mathrm{pK}}_\mathrm{a}$ matches the expected behavior: the stronger the electrostatic screening, the less neighboring carboxylate moieties affect the deprotonation probability at a certain pH.

	Vibrational mode	$\overline{\mathrm{E}}$ **[RT]**	$\mathbf{pK_a}$
[NaCl] $\leqslant$ 100mM	δ(C-O-H)	5.4 $\pm$ 1.7 (5.9 $\pm$ 1.1)	5.5 $\pm$ 0.5 (5.2 $\pm$ 0.4)
	ν_S(COO$^-$)	4.2 $\pm$ 1.5 (4.1 $\pm$ 1.2)	5.8 $\pm$ 0.5 (5.6 $\pm$ 0.3)
[NaCl] = 500mM	δ(C-O-H)	6.4 $\pm$ 1.3 (6.1 $\pm$ 1.7)	4.6 $\pm$ 0.4 (4.6 $\pm$ 0.5)
	ν_S(COO$^-$)	5.3 $\pm$ 0.5 (5.2 $\pm$ 0.7)	4.9 $\pm$ 0.2 (4.8 $\pm$ 0.2)

Table 4.2 Values obtained from the fit of Eqn. 4.5 to the experimental data at [NaCl] leq 100 mM and [NaCl] = 500 mM. The values in brackets indicate that the titration curves for increasing and decreasing pH were fitted separately and then averaged.

Typical densities predicted by different studies are $\sim$5.1 x 10^{-10} mol cm^{-2158} and 7.4 x 10^{-10} mol cm^{-2} (chemisorbed benzoic acid)[160] which translates to a mean nearest neighbor distance of 4.7 - 5.7 Å in a square lattice. Although the theoretical description might fail for distances of the protonatable groups less than $\sim$1 nm,[171] we attempted to estimate the mean nearest neighbor distance of carboxylate residues from the mean-field energy $\overline{E}$. 4-MBA was assumed to be adsorbed in a square lattice with lattice constant r. The mean-field energy can be estimated by summation over the Coulombic interaction $V(r_i)$ between the next-neighbors in a square lattice by

$$\overline{E} = \sum_i V(r_i) = \frac{e^2}{4\pi\epsilon\epsilon_0} \cdot \frac{1}{8}\left(4 + \frac{4}{\sqrt{2}}\right) \cdot \frac{1}{r} \tag{4.6}$$

where ϵ is the dielectric constant of the medium separating the moieties. It is not clear how the interface is microscopically composed and, thus, which ϵ to assign to it. However, assuming water (ϵ $\sim$80) in the intermolecular space yields a distance of r = 1.1 Å (1.4 x 10^{-8} mol cm^{-2}), formic acid (ϵ = 58.5)[173] r = 1.6 Å (6.5 x 10^{-9} mol cm^{-2}) and acetic acid (ϵ = 6.2)[173,174] r = 1.46 nm (7.8 x 10^{-11} mol cm^{-2}). These values scatter more than two orders of magnitude around the above mentioned experimentally determined densities which reflects the large variability of the dielectric constants assumed for the intermolecular space.

It is well known that the carboxylates (anti-)symmetric stretching frequencies $\nu_{s/as}$(COO$^-$) are highly sensitive to their chemical environment. The prominent upshift of the ν_S(COO$^-$) of $\sim$20 cm^{-1} (Fig. 4.9c, black trace) is another indicator for a strong interaction between the carboxylate moieties in the SAM. This observation might have several reasons: (1) due to the local electric field, increasing with the SAMs deprotonation degree ϑ, the diffuse electron density in the carboxylate head group is shifted towards the central carbon atom weakening the C-O bond and, thus, inducing a red shift of this band. (2) the strong electrostatic field, partially screened by interfacial salt, leads to a vibrational stark shift. However, no major vibrational stark effect is expected on the carboxylate moiety.[160] Instead spectral tuning of the $\nu_S(COO^-)$ of chemisorbed benzoic acid was attributed to a change of dipole-dipole coupling upon reorientation.[160] (3) a change of the hydrogen bonding network in close vicinity of the SAM interface with increasing ϑ.

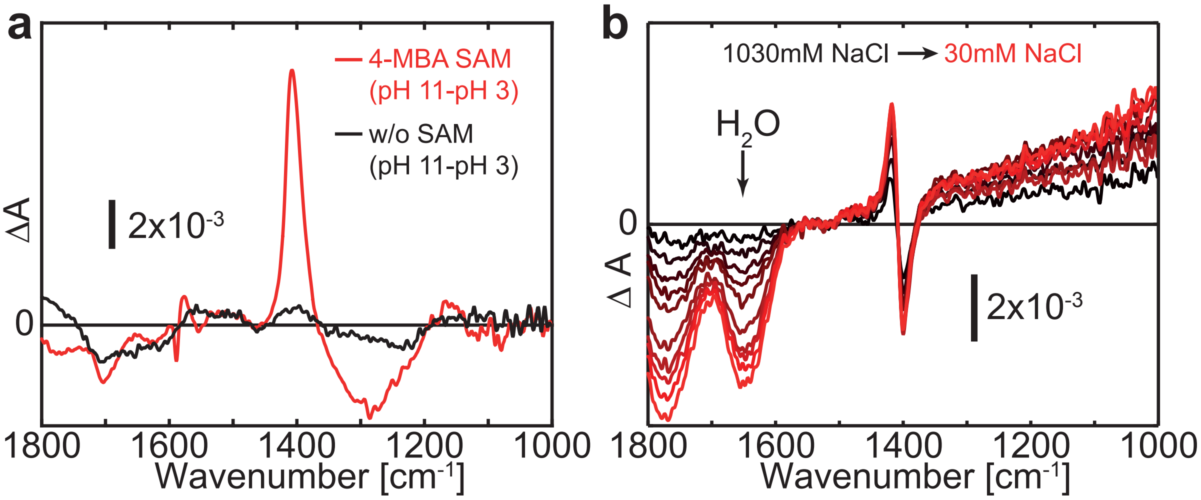

Figure 4.11 (a) Titration of a DAA with (red trace) and without (black trace) an 4-MBA-SAM. **(b)** Titration of the salt concentration (black: 1030 mM NaCl, red: 30 mM NaCl) at pH ~11.

To elucidate this, the titration was repeated with 500 mM NaCl present in the buffer (Fig. 4.9c, red trace and Fig. 4.11b). The red shift can be strongly diminished while the apparent pK_a is shifted towards its bulk value. This suggests that screening of the electrostatic interaction of the negatively charged carboxylate moieties by Na^+ plays a key role in the spectral shift and disfavors a pure hydrogen bonding network change as origin. Unexpectedly, there are additional difference bands in the region 1520 - 1600 cm^{-1} in the pH induced spectra (Fig. 4.9a). Modes arising in this frequency range can typically be assigned to ν(C=C) modes of the benzene ring or to $\nu_{as}(COO^-)$. The first one is not thought to be sensitive to the protonation state of the carboxylic head group whereas for the latter one our experiment is inherently insensitive: the predominantly up-standing orientation of the 4-MBA demands the transition dipole moment of $\nu_{as}(COO^-)$ to be parallel to the surface (see 2.2.3).[158] Reorientation of the SAM as origin of these difference bands is unlikely since the region around 1200 -1000 cm^{-1} shows no difference bands. As well, a reorientation of the molecules within the monolayer would consequently induce a strong contribution of the $\nu_{as}(\mathrm{COO}^-)$ in the spectral region between 1540-1650 cm^{-1} (the extinction coefficient of $\nu_{as}(\mathrm{COO}^-)$ is similar to that of $\nu_s(\mathrm{COO}^-)$).[175]

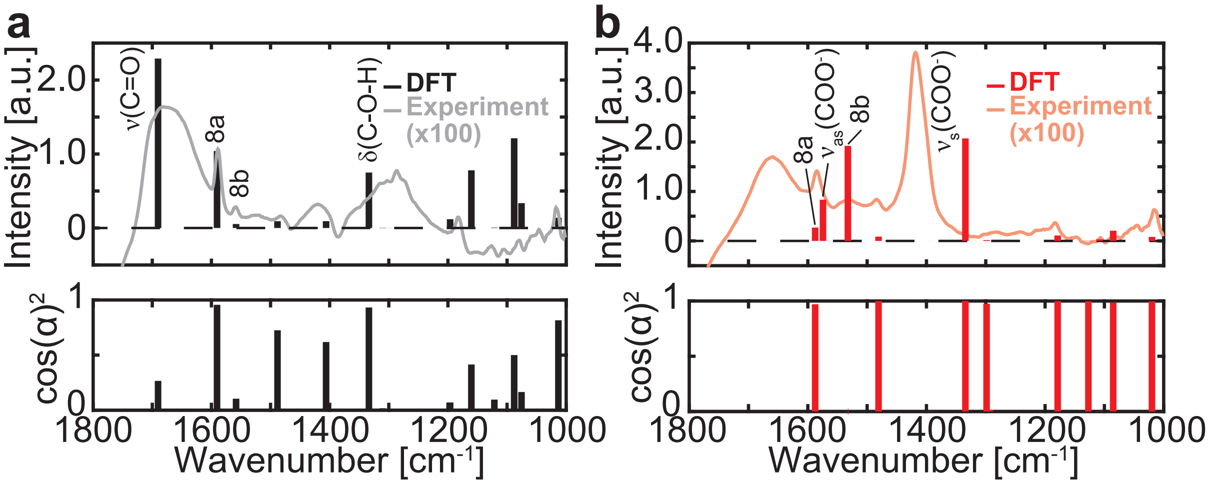

Figure 4.12 Absolute spectrum of 4-MBA in **(a)** protonated form (pH 3) and **(b)** deprotonated form (pH 11) including the calculated frequencies and intensities. Below each mode, a weighting factor indicates its approximate relative contribution along the long molecular axis due to the surface selection rule. α denotes the angle between the long axis and the derivative of the transition dipole moment.

To corroborate the origin of these difference bands and exclude reorientational effects on the $\nu_s(\mathrm{COO}^-)$ frequency, we performed supplementing DFT calculations on both protonation states of 4-MBA (see Sec. A.6). We adsorbed a SAM from a dilute aqueous solution of 4-MBA (see Fig. A.3) which allowed us to acquire absolute spectra of the monolayer at pH 2 (Fig. 4.12a) and pH 11 (Fig. 4.12b). In both spectra the main features can be attributed to 4-MBA. The two modes around 1590 cm^{-1} and 1560 cm^{-1} slightly red shift upon deprotonation. This behavior is reproduced by the DFT calculations. The relative intensities determined by the $\cos(\alpha)^2$ are plotted in Figure 4.9 below each spectrum according to the surface selection rules (see Sec. 2.2.3). α denotes the angle between the local molecular symmetry axis and the transition dipole moment as derived from the DFT computations. In the protonated state the vibrational modes at 1589 cm^{-1} and 1559 cm^{-1} can clearly be assigned to the 8a and 8b ring mode (*vide supra*). In the deprotonated state, however, this assignment is not clear. The DFT calculations predict the frequency of the $\nu_{as}(\mathrm{COO}^-)$ right between the 8a and 8b mode together with a down shift of the two ring modes compared to the protonated frequencies. The transition dipole moment of the 8b and $\nu_{as}(\mathrm{COO}^-)$ modes are perpendicular to the molecular axis and, thus, not visible in our experiments. Hence, the difference bands in the 1520 - 1600 cm^{-1} region are likely to be due to the phenyl ring modes shifting upon deprotonation of the carboxylic moiety. These observations suggest that the monolayer, once established, is conformationally rigid within aqueous environments as previously reported.[114]

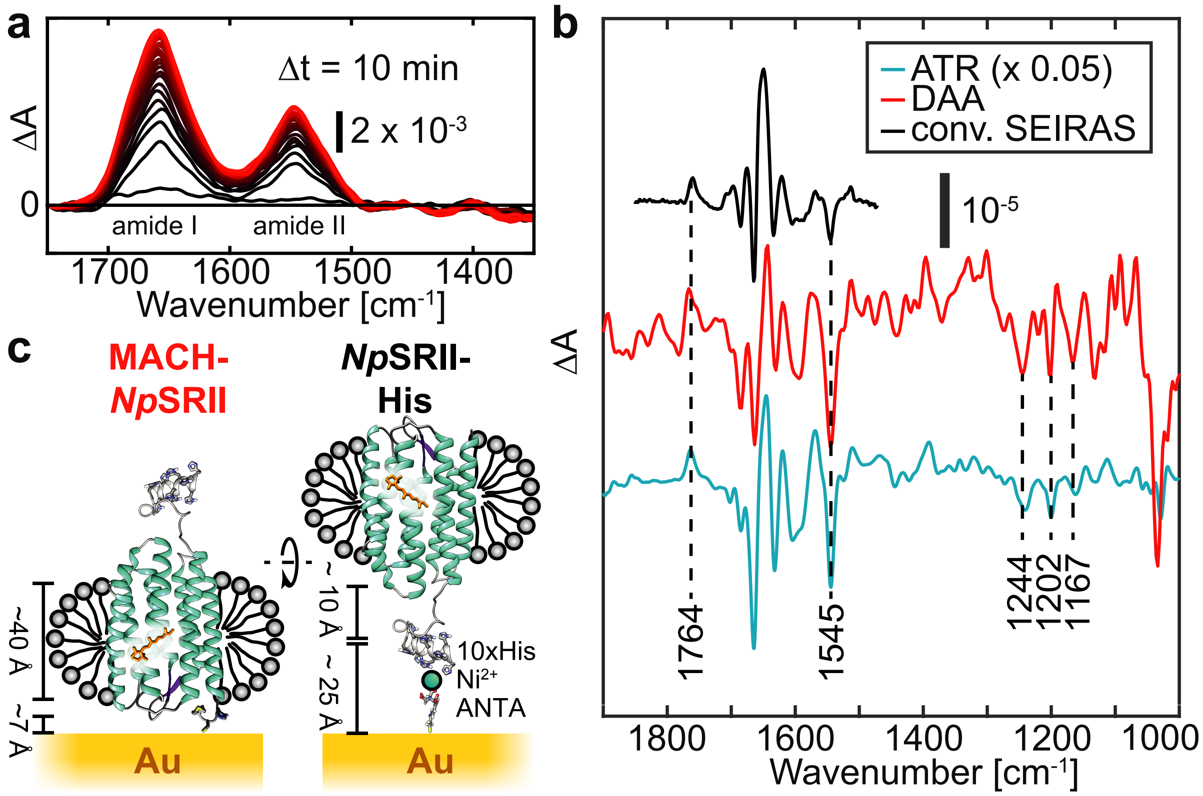

Figure 4.13 (a) Absorbance spectra during adsorption of the *Np*SRII-SAM. **(b)** Light-induced difference spectra of *Np*SRII obtained using DAAs (red), conventional Si-prism base SEIRAS (black) and ATR-FTIR (blue). **(c)** Sketch of the two structures monolayers established by MACH (as with DAA) or His-tag binding (as with conv. SEIRAS).

***Np*SRII adsorption and light-induced difference spectroscopy** To proof the effective applicability of the presented DAAs in sensing biological systems, we attempted to show functionality of an adsorbed monolayer of a light-sensitive membrane protein: sensory rhodopsin II from *Natromonas pharaonis* (*Np*SRII) (see Sec. 3.1). A monolayer of the detergent solubilized protein was attached covalently via its cysteins sulfur of a genetically engineered N-terminal MACH tag as described in Section 3.1.[121] The adsorption of the protein to the gold-water interface was followed over at least four hours *in situ* to guarantee a monolayer coverage (Fig. 4.13a). Light-induced difference spectra were recorded as described in Section 3.1 (Fig. 4.13b, red trace). The use of CaF_2 as substrate allowed us to acquire light-induced difference spectra in the range from 1100 - 1850 cm^{-1} without spectral artifacts due to excitons or phonons from the typically used Si substrate. Below 1100 cm^{-1} the noise increases significantly due to the increasing absorption of CaF_2. Features in this range will not be interpreted in the following paragraph. The three negative bands at 1244 cm^{-1}, 1202 cm^{-1} and 1167 cm^{-1}, clearly visible in both the ATR and DAA spectrum, can be assigned to ν(C-C) of the retinal co-factor of the protein in its all-*trans* isomer.[122] Additionally, the two bands at 1202 cm^{-1} and 1167 cm^{-1} were observed in resonance Raman spectra and consistently assigned to an all-*trans* retinal.[176] The main negative band at 1545 cm^{-1} was assigned to ν(C=C) of the all-*trans* retinal.[122] It is known that the co-factor isomerizes after photoexcitation from its all-*trans* conformation in the resting state to a 13-*cis* conformation.[122] This leads to a loss of those four typical bands during the photoreaction of *Np*SRII.

Difference bands between 1600 cm^{-1} and 1700 cm^{-1} indicate a structural rearrangement of the protein backbone. These are thought to be relevant for the signal transduction to the transducer domain,[177] which is absent in these experiments. The positive band at 1764 cm^{-1} can be assigned to the ν(C=O) of Asp 75.[122] Together with the retinals isomeriazation, this indicates that the protein accumulates the M state under the present monolayer conditions.

For comparison a light-induced difference spectrum of an earlier work using conventional Si-prism based SEIRAS (Fig. 4.13b, black trace)[22] and a far-field light-induced difference spectrum using ATR configuration (blue trace) are depicted. Overall, the difference spectra obtained by ATR-FTIR and with the DAAs correspond well by means of their vibrational frequencies and relative amplitudes of the specific bands. Compared to the prism-based SEIRAS spectra, the noise is higher using DAAs. The use of an infrared microscope in reflection mode decreases the photon flux significantly leading to an drastic increase in noise. Replacing the thermal globar with a more brilliant light source (e.g. synchrotron radiation[178] or fiber-based IR laser[139]) can restore the SNR. For the prism-based SEIRA spectrum *Np*SRII was attached via an oligo-histidine tag attached to a Nickel-nitrilo-triacetic acid linker SAM[19] (Fig. 4.13a, black trace, replotted from[22]). This immobilization strategy leads to an inverted attachment of the *Np*SRII-His protein and a different spacing as indicated in Figure 4.13c, since the His-tag is located at the C terminus. Yet, the difference spectrum is hardly affected except for the relative intensities of the amide I and retinal related bands. Bearing in mind that the near-field enhancement decays within several nm[32,179] these results suggest that the orientational freedom of the His-tag tethered protein results in alterations of the relative intensities.

Estimating the probed area of the gold discs to 90 μm x 90 μm x 0.5 (the latter factor considers the abundance of gold in the investigated region) which is fully covered by protein (the area of a single protein can be approximated by ~2nm x 3nm), we were able to detect <1 femtomole (10^{-15} Mole) of active membrane protein. This demonstrates the utility of the DAAs in life science as biosensors with utmost sensitivity for minute amounts of analyte.

4.2 Towards Single-Molecules: IR Near-Field Imaging and Spectroscopy

In the following section basic results accomplished with the constructed scattering-type scanning near-field optical microscope (*s*SNOM) (see Sec. 3.5) will be demonstrated and discussed. This includes nanoscopic imaging as well as nanospectroscopy of biological samples (purple membrane (PM) of *Halobacterium salinarum* and individual *H. salinarum* cells) at a lateral resolution of 30 nm. Combination of substrate induced near-field enhancement via resonant gold antennas and *s*SNOM for potentially enhanced nanospectroscopy will be investigated and critically discussed. Finally, a new sensing scheme will be presented using our home-built SNOM. Temperature gradients induced by the optical near-field were used to generate caloritronic currents in (anti-)ferromagentic thin films which were electronically read out. This read out will be used to extend our *s*SNOMs capabilities towards imaging of (anti-)ferromagentic domains.

4.2.1 Nanoscopic Imaging and Spectroscopy of Purple Membrane of *H. salinarum*

PM was used in several experimental works employing IR-*s*SNOM[44,45] and AFM-IR[135] as a model system and is, thus, perfectly suited as a bench-mark for the previously described home-built *s*SNOM (see Sec. 3.5). In the following section, I will present and discuss single-frequency imaging of individual PM patches using a QCL as light source and spectral broadband nanospectroscopy using a femtosecond fiber laser.

Single Frequency Imaging Mode PM patches spread on TSAu were prepared as described in Section 3.5.5. Membrane patches with a height of 4.7 ± 0.4 nm, characteristic for dried PM,[180] were found covering the surface on each sample (Fig. 4.14a). It is known that slowly drying PM results in cracks in the membrane patches due to shrinking, which are observed here as well.[181] Resolving the trimeric structure of bR inside the patches was never achieved. Imaging the fine structure with a lattice constant of 6.2 nm requires imaging in liquid phase.[181] Tips with a 25 nm thick Pt-Ir coating were used for spectroscopic enhancement, which additionally decreases the maximal achievable lateral resolution.

For comparison an ATR-FTIR spectrum of dried PM is shown in Figure 4.14b. Along with the topography, light scattered by the tip is interferometrically detected and demodulated by the LIA (see Sec. 2.3.2 and Sec. 3.5) at n = 3. The resulting near-field amplitude s_3 and near-field phase φ_3 is registered while scanning. Figure 4.14c-f shows the corresponding amplitude (c

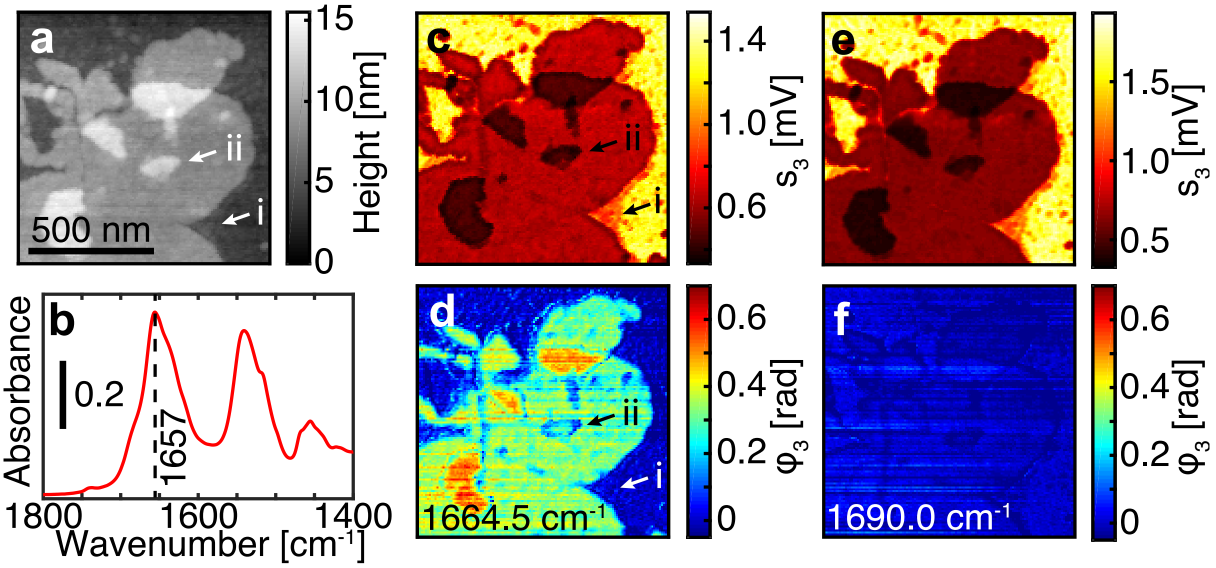

Figure 4.14 (a) Topography and *s*SNOM maps of PM on TSAu. **(b)** ATR absorbance spectrum of a dry film of PM. Amplitude (**(c)** and **(e)**) and phase (**(d)** and **(f)**) maps of a PM patch at 1664.5 cm^{-1} (**(c)** and **(d)**) and at at 1690.0 cm^{-1} (**(e)** and **(f)**) (demodulation order n = 3). The phase maps were offset line-by-line as described in the text.

and e) and phase (d and f) maps when the QCL is tuned to 1664.5 cm^{-1} (c and d) and 1690.0 cm^{-1} (e and f), respectively. The line rate k_{line} of scanner had to be set to 0.25 Hz, limited by the frequency M of the piezo driven phase modulation mirror. Typically a modulation frequency of M = 200-300 Hz was used. Higher phase modulation frequencies lead to a cross-talk of the mirror drive and the AFM which could be observed in the topographies. Slow thermal drifts in the relative length of the interferometer arms induced artificial drifts in the phase maps, which were corrected as described in Section A.9. While for the amplitude maps s_3 no obvious change in the contrast was found between maps recorded at 1664.5 cm^{-1} and 1690.0 cm^{-1}, the contrast in the phase maps φ_3 vanishes completely when the laser is tuned to 1690.0 cm^{-1} (note the same color scale in Fig. 4.14b-e). PM is densely filled with the protein bR and, thus, dominates its refractive index. For weakly dispersive oscillators like molecular oscillators of organic molecules, the near-field phase is proportional to the samples imaginary part ϵ_2 of the complex dielectric function. This is in turn proportional to its extinction coefficient k (see Eqn. 2.34).[45]

$$\varphi_n \propto \epsilon_2 = 2nk \tag{4.7}$$

Comparing the absorbance spectrum of PM (Fig. 4.14b, it becomes clear that there is no strong absorbance at 1690 cm^{-1} were as at 1664.5 cm^{-1} the extinction of the amide I vibration is almost maximal. Thus, the phase map at 1664.5 cm^{-1} is proportional to the protein content in the membrane patch. On several positions individual PM patches partially overlapped, leading to an approximate doubling of the phase. It is worth noting that the magnitude of the near-field phase contrast depends strongly on the tip sample-interaction and, thus, on the tip dithering amplitude and demodulation order n. However, it does not change the contrast qualitatively.[182, 183]

The two arrows in Figure 4.14a,c-d indicate positions in which the topography is not proportional to the phase information. At arrow i the topography and amplitude do not yet reach values typical for PM. However, the phase shows the same value as on gold. This suggests that at this particular position the integrity of the membrane is affected which might arise from interaction with gold.[45] It might as well resemble artifacts introduced by shrinking of the patch while drying the sample.[181] At arrow ii a small patch can be identified with height of ~5 nm. According to the topography, it could be interpreted as a second layer of PM deposited ontop of the big patch. The absence of an additional contrast in the phase, however, indicates that the material cannot consist of protein. The topographic feature at ii might be a contamination or lipid extrusion ontop or below the PM patch.

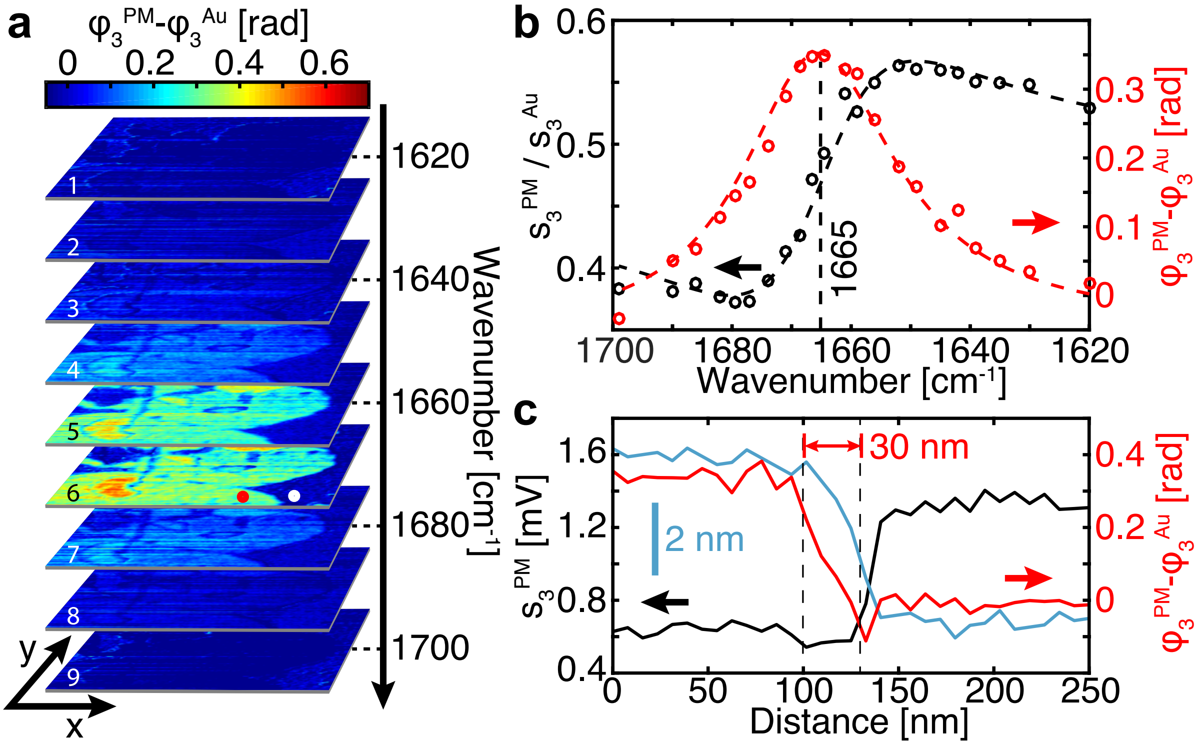

Figure 4.15 (a) Selection of nine (total 22) phase maps of PM recorded at different wavenumbers. **(b)** Amplitude and phase spectra extracted from the red dot in **(a)** (white dot indicates reference on Au). The dashed lines represent the point dipole model according to Eqn. 2.32 assuming a single Lorentzian oscillator as ϵ_{subs} fitted to the data. **(c)** Amplitude (black), phase (red) and topography (blue) extracted between red and white dot in **(a)**.

Figure 4.15a shows nine sequentially recorded phase maps of the PM patch shown in Figure 4.14 between 1620 - 1700 cm^{-1}. All maps were laterally aligned. The shift was determined by cross-correlating their corresponding amplitude maps. Qualitatively the same behavior can be extracted as seen before. Only when the QCL is tuned to the amide I mode of bR, a phase contrast can be seen. Amplitude and phase spectra were extracted from these maps at the locations indicated in map 6. The red spectrum (on PM) was referenced to the white one (on gold) (Fig. 4.15b). The characteristic lineshape of the amplitude and phase was fitted by the complex effective polarizability yielded by the point dipole model (Eqn. 2.32, see Sec. 2.3.2). For ϵ_{subs} a single Lorentzian oscillator was assumed. Figure 4.15a, b correspond very well to near-field spectra shown in literature.[44,45,135] The maximum of the absorptive phase was determined to be 1665 cm^{-1}, which is shifted by 8 cm^{-1} to higher frequencies compared to the far-field absorption maximum of PM (Fig. 4.14b). It was shown that organic thin films, depending on their thickness, deposited on highly reflective substrates induce a blue shift of several cm^{-1} in the phase.[184]

In Figure 4.15c cross-sections of the amplitude (black trace), phase (red trace) and topography (blue trace) along the line connecting the red and white dots in Figure 4.15a are shown. The topography rises from the substrate level to the PM level within ~30 nm. Correspondingly, the contrast in the amplitude decreases within the same distance. In contrast, the phase is slightly offset from both and the rise is wider spread. A minute negative dip on the onset of the rise can be seen. This artificial contrast can be sometimes seen in *s*SNOM phase maps, however, the origin of it is not yet clear and might be related to the nanoscopic structure of the tip. However, a chemical map by means of near-field phase of the PM patches at a lateral resolution of ~30 nm can be inferred from Fig. 4.15c (indicated by the dashed lines).

An additional slight negative phase contrast is obtained in the off-resonance maps in Figure 4.15a, 1& 9. It is unclear where this negative phase contrast emerges from. It was speculated that the tips antenna mode is more loaded upon approaching on the PM which induces an additional phase delay in the scattered field. Alternatively, the topography-dependent illumination of the tip by reflections on the surface was suggested as source of this delay.[132] This artifact will be discussed for *s*SNOM maps archeal cells with much higher non-resonant features (see Sec. 4.2.2).

Improving Imaging Speed The phase-modulation scheme, as reported in literature[97] and discussed in Section 3.5.2, is realized by a mirror, actuated by a piezo drive (phase modulation frequency M). For a stable interferometer it is necessary to be constructed as compact as possible which leads to potential mechanical coupling of the mirror drive and the AFM. The artificial modulation of the AFM at the mirror drive frequency M adds signals on the sidebands $n\Omega \pm M$

and strongly affects the reconstructed phase (see Fig. 2.12). Due to this considerations the modulation frequency has to be limited to 200 - 300 Hz in previous measurements, which in turn limited the imaging speed to 50 pixels per second. As described in Section 3.5.2 I placed an PEM in the reference arm with its modulation direction oriented along the polarization of the incident light, thus, acting as a phase modulator operating at ∼50 kHz.

Figure 4.16a, b display the amplitude s_4 and phase φ_4 maps of the same PM patch at 1665 cm^{-1}, recorded with the piezo phase-modulation (a, M = 300 Hz) or PEM phase-modulation (b, M = 50 kHz). The imaging parameters were previously optimized for maximal imaging speed with the former one (LIA time constant t_c = 500 μs, line rate of the AFM scanner k_{line} = 0.25 Hz). Note that all colorbars are kept constant throughout the whole figure. Qualitatively, the four maps match perfectly and show exactly the same contrast in both amplitude and phase. Only the slightly lower amplitude in the PEM phase-modulation can be noted. This might be due to an imperfect alignment of the reference beam to the light scattered from the tip. Figure 4.16c and d show the amplitude and phase maps recorded with the LIA settings optimized for the piezo-based phase modulation but with a 20 times increased imaging speed. As expected all four maps show still the same contrast but are strongly blurred. The low-pass filter of the LIA limits the highest detectable spatial frequency and induces that blurring. Decreasing the low-pass filter cut-off frequency by an order of magnitude, the LIA is not anymore able to correctly demodulate the signal and the contrast in the amplitude and the phase is deteriorated (Fig. 4.16e). Only the higher modulation frequency of the PEM allows to operate the demodulation scheme at this short time constants. The contrast in the two maps in Figure 4.16f is quantitatively the same as in 4.16a, b although the maps in 4.16f are recorded 20 times faster. Importantly, the SNR is not reduced by faster scanning. In Figure 4.16a,b,f the black (slow acquisition rate) and red (fast acquisition rate) solid lines indicate near-field phase cross sections taken along the corresponding dashed lines. The SNR slightly increases by introducing the PEM. Surprisingly, the noise stays virtually constant in the maps recorded using the PEM (black and red solid lines in Fig. 4.16b,f) despite the drastically decreased time constant of the LIA and increased imaging speed. When comparing Figure 4.16b and 4.16f, the former exhibits horizontal stripe like artifacts. The faster image acquisition is less sensitive to slow phase variations induced by thermal drift of the relative length of both interferometer arms and a constant phase offset per line yields a cleaner image. Figure 4.16g shows the corresponding topography. In 4.16h the QCL was tuned to 1710 cm^{-1} and the contrast vanishes and get slightly negative as discussed above.

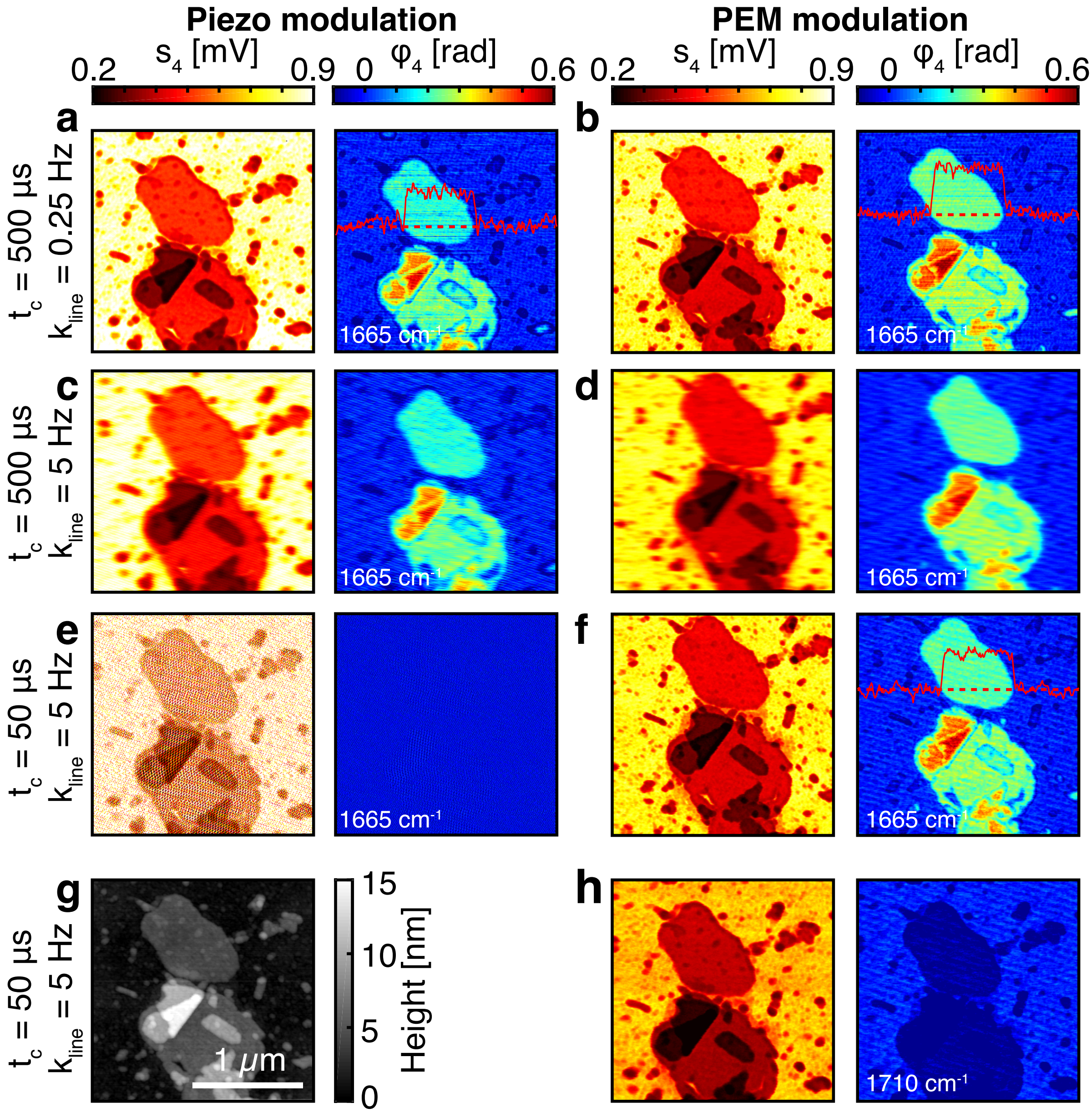

Figure 4.16 Amplitude and phase maps of PM patches recorded with piezo (**(a)**, **(c)**, **(e)**) or PEM (**(b)**, **(d)**, **(f)**) phase modulation at different line rates (k_{line} = 0.25 Hz and k_{line} = 5 Hz) and LIA settings on resonance ($\tilde{\nu}$ = 1665 cm^{-1}). The dashed lines in **(a)**,**(b)** and **(f)** indicate where the near-field phase cross sections (solid black/red lines) were taken. **(g)** shows a typical topography. **(h)** Amplitude and phase map off resonance ($\tilde{\nu}$ = 1710 cm^{-1}) recorded at k_{line} = 5 Hz using the PEM. All images show a 2x2 μm^2 field of view (256x256 px).

Considering the SNR of the near-field phase φ_4 at 1665 cm^{-1} across the PM patch (red dashed line in Fig. 4.16f), a lateral resolution of 30 nm and the size of a single bR molecule in the patch of 2x3 nm^2, ~400 individual molecules can be detected at an SNR of ~10 with an integration time of 390 μs per pixel. Besides the faster imaging capabilities this modulation technique allows the acquisition of time-resolved near-field responses at μs temporal resolution.

Towards IR *s*SNOM in aqueous environments Aqueous environments pose a challenge in IR spectroscopy due the high extinction coefficient of its bending (δ(O-H)) and stretching ($\nu_{\mathrm{s,as}}$(O-H)) modes which cover most of the relevant modes of biological macro-molecules. The major challenge in the experimental realization of an IR *s*SNOM operating in aqueous environment is coupling of light to the metallized AFM tip and collecting the scattered light without the interference of water. Although alternative methods for IR near-field microscopy in liquid were presented – either covering the sample of interest with a graphene monolayer and using *s*SNOM[48] or AFM-IR[185] – no work was published on *s*SNOM in arbitrary aqueous environments. In the following, a novel approach based on an evanescent field will be presented accompanied by preliminary data.

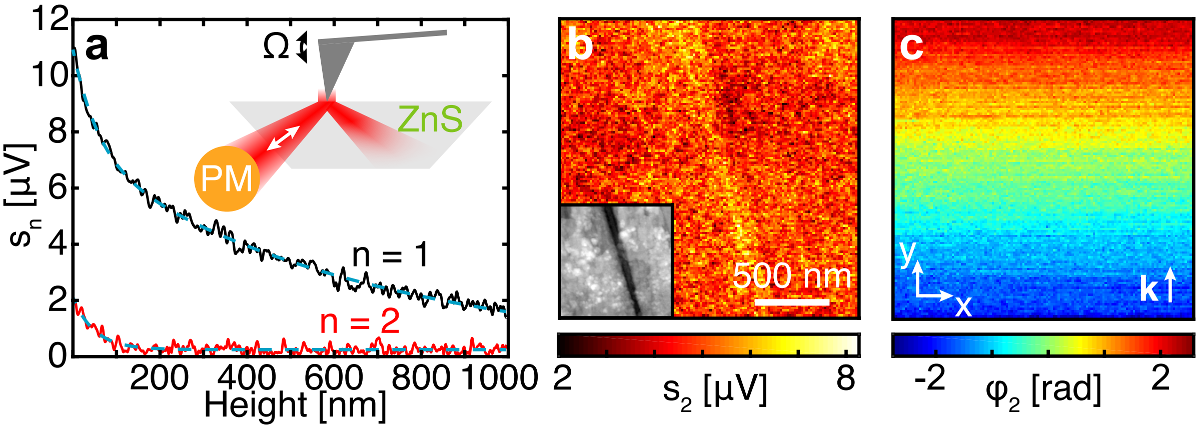

Figure 4.17 (a) Approach curves for n = 1 and (black trace) and n = 2 (red trace). Cyan traces indicate bi-exponential fit (for n = 1) with $d^2_{n=1}$ = 662 nm, $d^1_{n=1}$ = 57.7 nm and single exponential fit (for n = 2) with ${d_{n=2}}^1$ = 49.5 nm. **(b)** Amplitude map s_2 and topography as inset (50 nm maximal height). **(c)** Phase map φ_2 evaluated according to ref.[98] and Eqn. 2.29

Figure 4.17a shows the basic principle of the suggested setup. Instead of illuminating the tip by an OAP from the side through air, a OAP is adjusted such that the focused radiation is totally reflected on an total internal reflection (TIR) element made from ZnS. The tip is placed in the evanescent wave and the scattered photons are detected through the same OAP as in the conventional *s*SNOM scheme. Approach curves are shown in Figure 4.17a when the scattered light is demodulated at n = 1 (black) or 2 (red). Already for n = 2 a clear near-field behavior is apparent which is confirmed by the fast decay to $1/e$ at ${d_{n=2}}^1$ = 49.5 nm. The signal demodulated at the tips fundamental frequency decays slower and was fitted with a bi-exponential decay to account for the evanescent scattering on the tip shaft as well as the pure near-field contribution. The two decay lengths are $d^1_{n=1}$ = 57.7 nm and $d^2_{n=1}$ = 662 nm. The former decay length corresponds well to the decay length seen for n = 2 where as the latter reflects the decay length of the evanescent field at the ZnS / air interface of $\sim$ 600 nm at 1664 cm^{-1} (AOI: $\sim$45°, refractive index at 1664 cm^{-1} was calculated by a linear regression from the values for 5 and 8 μm found in ref.[186]).

Figure 4.17b and c show pseudo-heterodyne amplitude s_2 (b) and phase φ_2 (c) maps recorded when the prism is scanned by 2 x 2 μm^2 underneath the steady dithering tip (n = 2). A slight contrast is visible in the amplitude due to the scratch on the surface of the ZnS (see inset in Fig. 4.17b). Otherwise the amplitude stays constant. Replacing the ZnS by a polished Si TIR element will yield much smoother surfaces complying with the AFMs utmost height sensitivity.

In Figure 4.17c the phase increases linearly with displacement of the prism. The full phase retrieval algorithm was used (see Sec. A.8 and 2.3.1 and ref.[98]). The increasing phase delay is related to the fact that by displacing the TIR element to the y-direction, which is the direction of the incident radiation $\mathbf{k}$ in this experiment, the optical path difference will be increased. This background can be reduced by applying the full phase retrieval algorithm and subtracting a planar phase which is a common task in scanning probe microscopy (SPM) data analysis.

Due to limited time, the experiments needed to be stopped at that stage. However, the transfer to aqueous environment is straight forward and planned. The AFM can be routinely operated in liquid. The evanescent illumination of the tip circumvents the strong absorption of the aqueous phase above the TIR element and the scattered photons can be conveniently collected through the same focusing optics.

Broadband Spectroscopy Near-field microscopy at single frequencies is a powerful tool for selective imaging of certain domains which exhibit a specific vibrations. Yet, this vibrational fingerprint is generally not known a priori. Clearly identifying a characterisitc spectral fingerprint of a sample requires extension of the spectral bandwidth. The reference arm of the interferometer of our home-built near-field microscope can easily be modified by a flip mirror such that a movable retroreflector can scan through OPDs (Fig. 3.7). This enables broadband spectroscopy with a suited spectrally broadband light source. In our case radiation from DFG fs-laser system can be coupled to the *s*SNOM, which emits an average power of up to 2 mW with a bandwidth of several 100 cm^{-1} (see Fig. 3.8b).

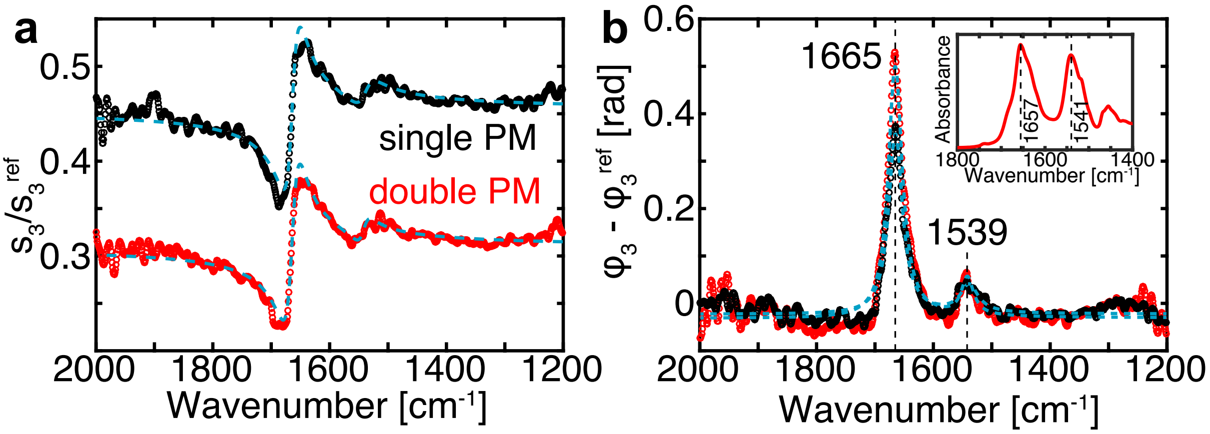

Figure 4.18 nano-FTIR amplitude **(a)** and phase **(b)** spectra of a single (black) and double (red) layer of PM referenced to its gold support. The cyan dashed line indicates a point dipole model fit assuming two Lorentzian oscillators for the spectral response of the PM. All spectra are an average of 50 individual spectra at 4 cm^{-1} resolution (scanner speed: 0.6 kHz, n = 3).

To investigate the functionality of the spectrometer, spectra of single and double layers of PM adsorbed on a TSAu were recorded (Fig. 4.18) over a spectral range covering almost the whole diagnostically relevant mid-IR fingerprint region from 2000 to 1200 cm^{-1}. Both spectra show the typical lineshape for an amide I and amide II mode. The maximum of the phase for the amide I (1665 cm^{-1}) is the same as in the previous single frequency maps (Fig. 4.15b). The most apparent difference is the relative intensity of amide I and II. Typically the extinction coefficients of these two modes are very similar (see inset of Fig. 4.18b). In the present spectra the amide II is about an order of magnitude weaker than the amide I mode as seen in near-field spectra in literature.[44,135] This is owing to the fact that PM consist of highly oriented lattice of bR which is aligned on the substrate surface by the drying process. The transition dipole moment of the amide I mode is oriented to the membrane normal, whereas the transition dipole moment for the amide II lies in the membrane plane. Due to the dipole interaction of the tip with the sample, the vibrational modes are probed in a polarized fashion. Only vibrational modes with a component normal to the surface are efficiently sampled which results in the much stronger contrast of the amide I.

Spectra of a single and double layer show the same spectral features and relative band intensities. However, the amplitude contrast is slightly decreased whereas the phase contrast is increased by ∼30%. Although the amount of probed protein in the near-field can be assumed to be twice for the double layer spectrum, the phase of the amide I phase band is not doubled. This can be attributed to the near-field decaying from the tips apex exponential with decay lengths in the order of tens of nm.[187] The lower membrane layer contributes less to the phase spectrum as the upper one.

The resulting amplitude and phase spectra were fitted with the point dipole model (Eqn. 2.32) assuming two harmonic oscillators with Lorentzian lineshape contributing to the signal. Again the point dipole model reproduces the experimental results very well. Minor deviations might be due to the assumed Lorentzian lineshape of the two oscillators. Typically the lineshape of organic substances in the infrared is represented by a Lorentzian convoluted with a Gaussian (termed Voigtian). The upshift of the amide I frequency compared to far-field FTIR is in accordance with reported blue shifts for thin films in *s*SNOM phase spectra.[184] This is not the case for the amide II vibration which might be related to the insufficient SNR in those spectra. Alternatively, the shift might be related to vibrational anisotropy of PM. The maxima of the amide I and II bands shift upon probing it along the membrane normal up and down, respectively, as seen in transmission-FTIR spectra of highly oriented PM patches.[144] Both effects might be mixed here and are difficult to disentangle.

A spectrally resolved line scan was acquired across the edge of a purple membrane (Fig. 4.19a) to determine the lateral resolution of the presented apparatus. 40 individual spectra were acquired along 100 nm of which each took approximately 30 seconds (n = 3, 8 cm^{-1} spectral resolution, 5 coadditions per pixel) (Fig. 4.19b,c). The only spectral feature observable is the amide I mode. The SNR does not allow to observe the amide II as seen in Figure 4.18b. The average of the phase between 1670 and 1660 cm^{-1} along the edge is displayed together with the height profile in Figure 4.19d. The phase increase is wider spread in contrast to the topography which is in line with the observations made on the single frequency maps (Fig. 4.15c). From the line scan a lateral resolution of ∼30 nm can be inferred. This value is comparable to others found in literature for near-field spectroscopy on PM or PMMA.[44,100] Assuming the area of a single bR protein of 2 x 3 nm^2, I could estimate the number of proteins probed in such experiments to

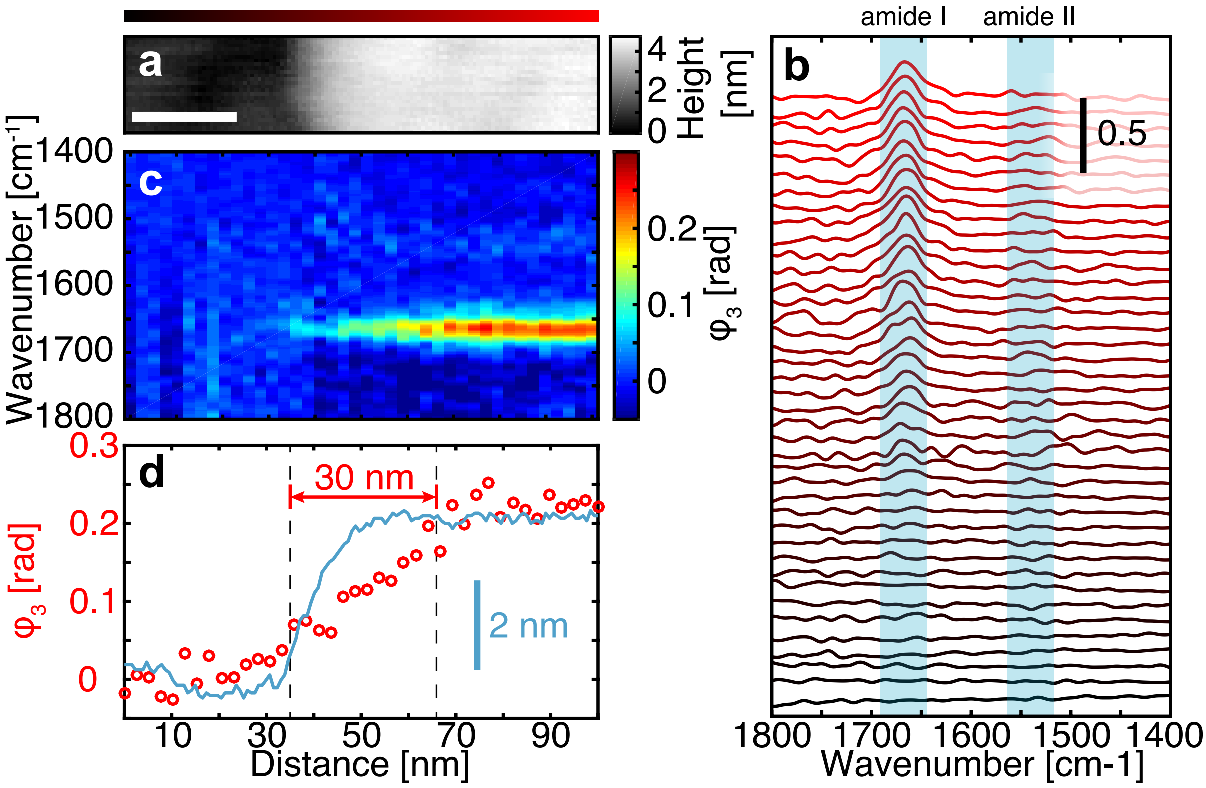

Figure 4.19 **(a)** Topography across an edge of PM dried on TSAu (scale bar: 20 nm). **(b)** Spectral line-scan (ϕ_3) across the PM edge shown in **(a)** in steps of 2.5 nm. **(c)** Spectra of the line-scan in **(b)** (offset for clarity). **(d)** Average phase (1660 cm^{-1} to 1670 cm^{-1}) across the edge (red) and integrated height profile (blue).

few hundreds (~ 400). Comparing this to the data shown in Figure 4.18b, the absorptive phase signature of 400 molecules (7 x 10^{-22} mol) were observed at a SNR of ~40 (within 6 minutes acquisition time). This results give rise to the expectation that *s*SNOM might be the method of choice for future single molecule IR absorption spectroscopy studies.[14,51] The line scan capability can be easily extended to a 2D mapping of arbitrary samples, thereby acquiring a hyperspectral image. It is noted that long-term drifts of the relative tip-sample position while mapping needs to be checked in regular intervals. If the position has changed, a manual realignment will be necessary.[46]

4.2.2 Nano Spectroscopic Investigation of Dried Individual *Halobacteria salinara*

The archaea *H. salinarum* is found in ponds which temporarily dry out. It can survive these dry periods by adapting a state, in which the metabolism is slowed down.[188] Accordingly, this archaeon requires very high salt concentrations ($c_{\mathrm{NaCl\ or\ KCl}} > 2$ M) to survive and maintain its native morphology.[151,189–191] Under low oxygen tension, *H. salinarum* expresses the membrane protein bR.[192] However, the organization and potential lateral segregation of the highly oriented PM patches in the membrane of *H. salinarum* is under debate.[193] In previous unpublished work, E. Hubrich (Experimental Molecular Biophysics, Freie Universität Berlin, Germany) and Iban Amenabar (CIC Nanogune, Spain) tried to resolve locations of enriched bR in the cells membrane by means of *s*SNOM. However, they either found cells with a homogeneous distribution of the amide I mode (~1660 cm^{-1}) or cells exhibiting a strong unusual absorption at ~1740 cm^{-1} at the cells poles, locally depleting the amide I band. In the following, IR near-field maps of individual dried archeal cells, acquired with the above introduced *s*SNOM and nano-FTIR setup, will be presented and discussed, particularly to verify the mentioned preliminary findings.

Samples of two strains S9 and L33 were prepared (see Sec. 3.5.5) of which L33 did not express bR in the form of PM while S9 overexpresses bR to form PM. After spinning down the culture, the pellets had a light brown color for the L33 samples, common for cells containing no chromophore and a distinctive purple color typical for PM for the S9 samples. Liquid cultures were generously provided by Kirsten Hoffmann, Dorothea Heinrich and Dr. Ramona Schlesinger (Genetic Biophysics, Freie Universität Berlin, Germany).

Figure 4.20 shows two exemplary topographies, *s*SNOM amplitude and phase maps of individual cells for each of the two strains L33 (Fig. 4.20a) and S9 (Fig. 4.20b) dried on Si. A comprehensive overview of the imaged *H. salinara* is presented in Section A.10. Both were imaged at ~1670 cm^{-1}, which mainly captures the amide I and liquid water contribution, and 1740 cm^{-1}, for which a strong contrast has been seen at the cells poles in previous work (see above). The morphology of both strains is summarized in Table 4.3. All cells exhibited a rod like structure with an aspect ratio of ~3 - 5. The cells often appeared thicker at their poles and thinner in the central region as seen in early AFM scans by Butt et al.[188] The morphology of cells of both strains is very similar within the present data set as well as to previous reports.[188,189] Components in the buffer (4.3 M NaCl, 80 mM $MgSO_4$, 10 mM tri-sodium citrate, 27 mM KCl) typically crystallized on top of the archaea and yielded structures eventually exceeding 1 μm in height. Only few cells were found uncovered.

The amplitude s_3 and phase φ_3 maps at 1670 cm^{-1} did not differ significantly among the

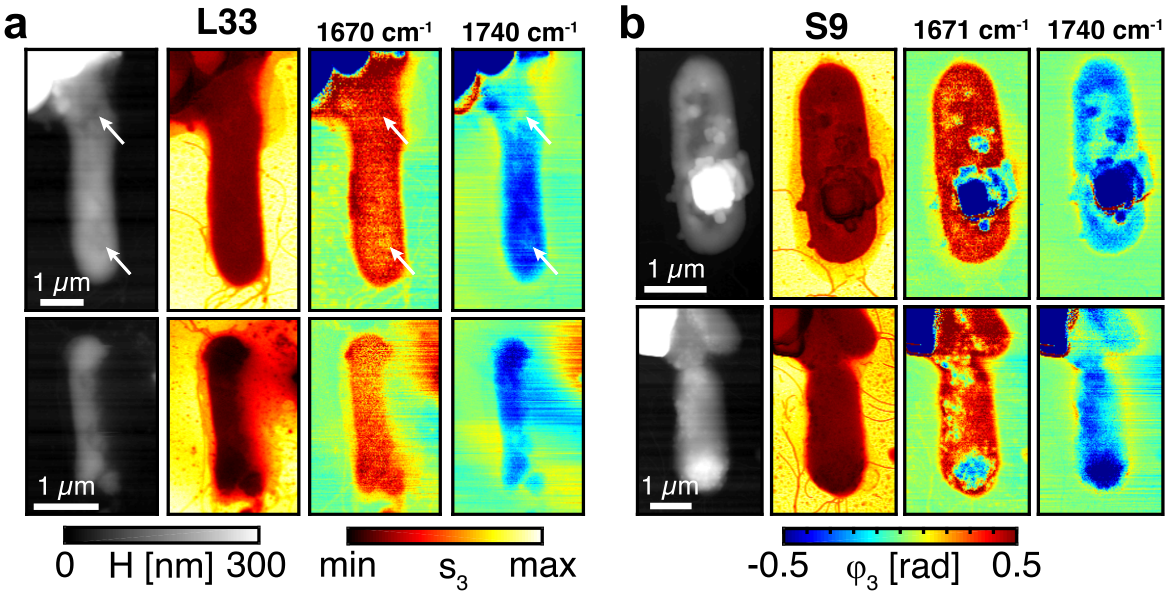

Figure 4.20 *s*SNOM maps of *H. salinara* of the strain L33 **(a)** and S9 **(b)**. Topography, amplitude s_3 map and phase φ_3 maps recorded with the QCL tuned to ~ 1670 cm^{-1} and 1740 cm^{-1} (n = 3). The full phase retrieval algorithm was used (see Sec. 2.3.1).[98] The white arrows in **(a)** indicate spots with a slight positive phase contrast at 1740 cm^{-1} and will be addressed spectroscopically in Fig. 4.23.

Strain	**Length** [μm]	**Width** [μm]	**Height** [nm]	**# of cells**
L33	3.4 ± 0.3	1.0 ± 0.2	179 ± 17	28
S9	3.1 ± 0.3	1.1 ± 0.2	146 ± 20	19

Table 4.3 Morphology of gathered from individual *H. salinara* cells of the strain L33 and S9.

different cells and strains despite the fact that the membrane of the S9 cells should be heavily loaded with bR in the form of PM. Besides the cells' rod-like body, their flagella could be clearly seen in the topography, amplitude and in some occasions in the 1670 cm^{-1} phase map. The phase φ_3 at 1670 cm^{-1} is mainly homogeneous within the cells body except for spots, where the archaea are covered with crystalline residuals. This result indicates an even protein distribution at least in the cells membrane. Since the sensing volume of *s*SNOM decays within ~30-80 nm in z-direction,[194,195] this homogeneity might also reflect the protein distribution in the cells interior. Similarly, a homogeneous protein distribution in gram-negative *Escherichia coli* (*E. coli*) cells was reported inferred from AFM-IR sub-wavelength mapping of the amide I absorption band.[196,197] A patch like arrangement of the bR in patches[193] could not be confirmed by the near-field phase maps at 1670 cm^{-1}.

The amplitude in the near-field maps at 1740 cm^{-1} and the ones at 1671 cm^{-1} did not differ except for the absolute intensity. Accordingly, only the amplitude maps at 1670 cm^{-1} are further shown. In the phase maps at 1740 cm^{-1} an overall negative contrast is apparent on the cell which correlates to topography (see Sec. 4.2.1).[132] Structures which exhibit a decreased phase on the cells body at 1671 cm^{-1}, however, appear to have a lower near-field phase at 1740 cm^{-1}, as well. Spots with a slightly positive phase contrast at 1740 cm^{-1} and no noticeable increase in height could seldom be found (see arrows in Fig. 4.20a) and were addressed spectroscopically (see below, Fig. 4.23). A strong positive phase contrast at 1740 cm^{-1}, as previously reported, could not be identified on any of the imaged cells (# of cells = 27).

For both strains, most cells were covered by crystalline residuals. The decreased amount of protein in the sensed volume accounts for the diminished phase contrast at 1670 cm^{-1}. Some crystals appear to have a cubic shape with heights > 300 nm (white areas in the topography maps in Fig. 4.20). The phase heavily decreases for both frequencies at this locations due to the topographic crosstalk at this gigantic structures.[132] It is noteworthy that the residuals of the buffer strongly affected the acquisition process. Often, the optical amplitude suddenly dropped due to loose particles contaminating the tip. Additionally, the microscopic roughness of the sample led occasionally to interference patterns, visible in some near-field maps despite the higher harmonic demodulation.[187]

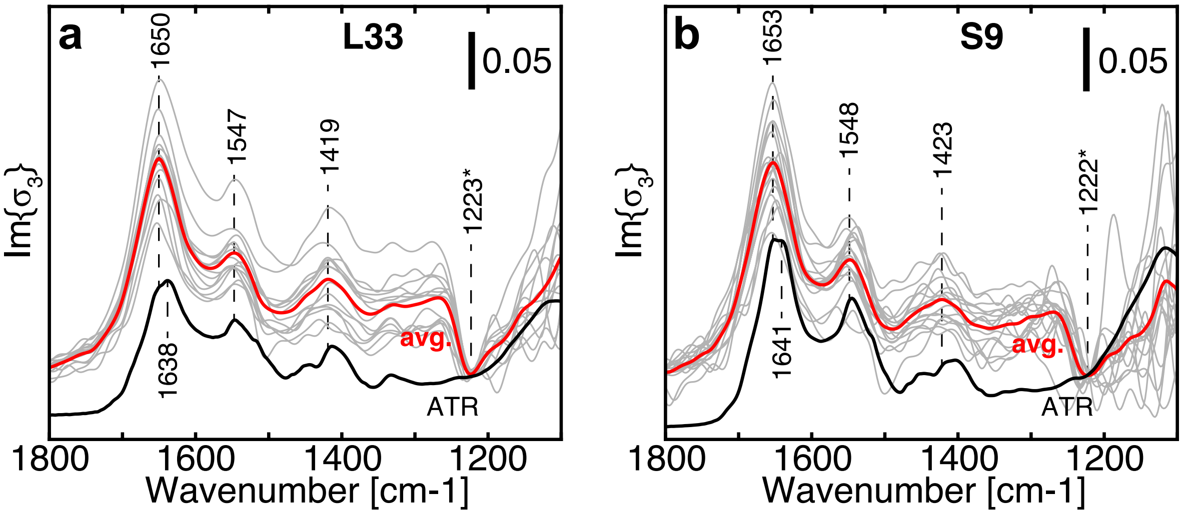

Figure 4.21 nano-FTIR spectra acquired on homogeneous spots on individual *H. salinara* from the strain **(a)** L33 (# of cells = 6) and **(b)** S9 (# of cells = 8) at 8 cm^{-1} resolution (0.3 kHz scanner speed, n = 3). A linear baseline was fitted through the range 1850 - 1800 cm^{-1} and 1200 - 1250 cm^{-1}. The lower red spectrum represents the average of all near-field spectra of one species. The black spectrum corresponds to the far-field spectrum of the dried cell culture in recorded by ATR-FTIR.

To access the spectroscopic characteristics of individual cells and, moreover, spots which showed an heterogeneous phase contrast at 1740 cm^{-1}, nano-FTIR spectra were recorded on individual *H. salinara*. Figure 4.21 displays spectra acquired on spots exhibiting a homogeneous amide I distribution of individual cells of the two strains L33 (Fig. 4.21a) and S9 (Fig. 4.21b).

The average of all homogeneous near-field spectra (red trace) corresponds well with the far-field spectrum recorded with ATR-FTIR (black trace) of a dried film of a concentrated cell culture except for minor shifts in the frequency. To distinguish the amide I contribution (1650/1653 cm^{-1}, L33/S9) from eventual δ(O-H) of liquid water (1638/1641 cm^{-1}), the ATR spectra (recorded with 2 cm^{-1} resolution) were treated by Fourier-self-deconvolution (Lorentzian width 8 cm^{-1}, quadratic triangular apodization).[50, 198]

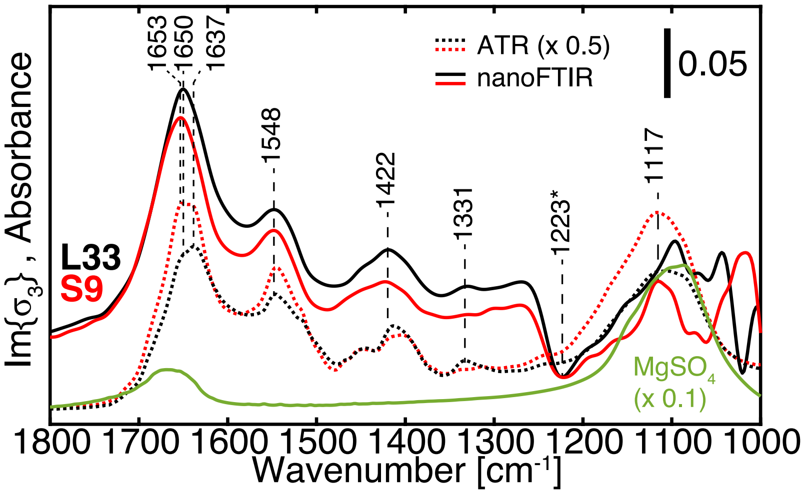

Figure 4.22 Solid lines: average nano-FTIR spectra of both strains at homogeneous locations (black: L33, red: S9 ,8 cm^{-1} resolution, 0.3 kHz scanner speed, n = 3). Dashed lines ATR-FTIR spectra of both strains (black: L33, red: S9). Green line: KBr spectrum of $MgSO_4 \cdot 7\,H_2O$.

Figure 4.22 shows the average of those spectra recorded on homogeneous spots (solid lines) along with the ATR spectra of both strains. As pointed out by Mastel et al. the peak positions in the imaginary part of the near-field spectra $\mathfrak{Im}(\sigma_n)$ corresponds very well to far-field FTIR peak positions.[184] Accordingly, for the following spectra only $\mathfrak{Im}(\sigma_n)$ will be discussed. The frequencies of the amide I (1650 / 1653 cm^{-1}, L33 / S9) and amide II (1547 / 1548 cm^{-1}, L33 / S9) vibrations of the proteins backbone are very close to the ones in the far-field spectra (1649 / 1652 cm^{-1} for L33 and 1547 / 1545 cm^{-1} for S9). Despite the fact that the strain S9 expresses bR and L33 does not, the spectra of both strains are very similar to each other and correspond well to previously reported far-field ATR-FTIR spectra.[199] Similar frequencies have been seen for *E. coli* in near-field spectra acquired by AFM-IR (amide I: 1648 cm^{-1}, amide II: 1548 cm^{-1}).[200] The relative amplitude of the amide I and amide II in the far-field spectra is $I_{\text{amide I}}$ / $I_{\text{amide II}} \sim 1.4$, which is common in infrared spectra of whole bacterial cells.[201] In the near-field spectra, however, this ratio increases to $I_{\text{amide I}}$ / $I_{\text{amide II}} \sim 1.8$. Although contributions of δ(O-H) of liquid water at 1638 cm^{-1} can be seen in the far-field spectra, which would lead to an artificial increase of that ratio, they appear to be minor (see Sec. A.11 and Fig. A.8). AFM-IR studies report as well on this unusual high ratio and attribute it to an instrumental artifact.[200] In contast, the increased relative amplitude might as well be attributed to the high amount of trans-membrane α-helices sensed by the *s*SNOM, primarily aligned vertical to the membrane plane. Accordingly, the amide I mode is mainly sensed due to the selection rule for modes aligned along the z-axis, as seen for PM as an extreme case (see Sec. 4.2.1).[44,45]

The bands in the region of 1500 - 1100 cm^{-1} are typically difficult to assign because many coupled vibrations contribute to these bands. The bands around 1422 cm^{-1} might be assigned to to δ(C-H) of CH_2 or ν_s(O-C-O) of carboxylates, whereas at 1310 - 1240 cm^{-1} the amide III vibration of the proteins backbone is typically found.[201] The ν_{as}(P=O) of PO_2^- (1250 - 1220 cm^{-1})[201] is overlapped by a prominent negative band at 1222 cm^{-1} marked with an asterisk (*) in the near-field spectra. This is due to the stretching vibration of the native SiO_2 layer formed on the Si substrate against which all spectra of the cells are referenced.[202,203] This becomes apparent when looking at the phase spectra of reference and sample separately (see Sec. A.13 and Fig. A.10).

In the far-field and near-field spectra on crystallized residuals (see below, Fig. 4.24) a strong band around 1117 cm^{-1} can be seen. In this region ν(C-O), ν(C-C), δ(C-O-H) and δ(C-O-C) modes of carbohydrates mainly contribute.[201] Yet, this band might be attributed to vibrations of the SO_4^{2-}. It might either be due to $MgSO_4$ of the used buffer (see green trace in Fig. 4.22)[204] or sulfate covalently attached to the archeal surface layer (S-layer).[199,205]

Near-field spectra recorded on irregular spots on the archaea (Fig. 4.23a, b) are shown in Figure 4.23c. Although rarely observed (# of cells = 3), these spots exhibited an increased contrast in the 1740 cm^{-1} phase maps and two of them show morphological alterations of the cell (the corresponding locations are marked by circles in Fig. 4.23a, b). At location 1 and 3 the cell wall seems to be partially disintegrated or ruptured. This might be either due to the two adjacent cells in each region adsorbed on the Si during division or a lesion occurred in consequence of drying. Location 2 appears to be topographically smooth. All of these irregular near-field spectra show a common, altered composition of bands. A slight shoulder around 1709 cm^{-1} appears which is the reason for these spots being localized in the 1740 cm^{-1} φ_3 maps with a positive contrast. A strong band around 1620 cm^{-1} arises which either obscures the typically present amide II mode or corresponds to a different compound as protein. Another strong band appears at the lower end of the spectral range, starting from 1200 cm^{-1}. For comparison the KBr-FTIR spectra of the major IR active components of the buffer ($MgSO_4$ (solid), Na-tricitrate (dot-dashed) and buffer mix (dashed)) are displayed in Figure 4.23c. The increased bands at the mentioned frequencies

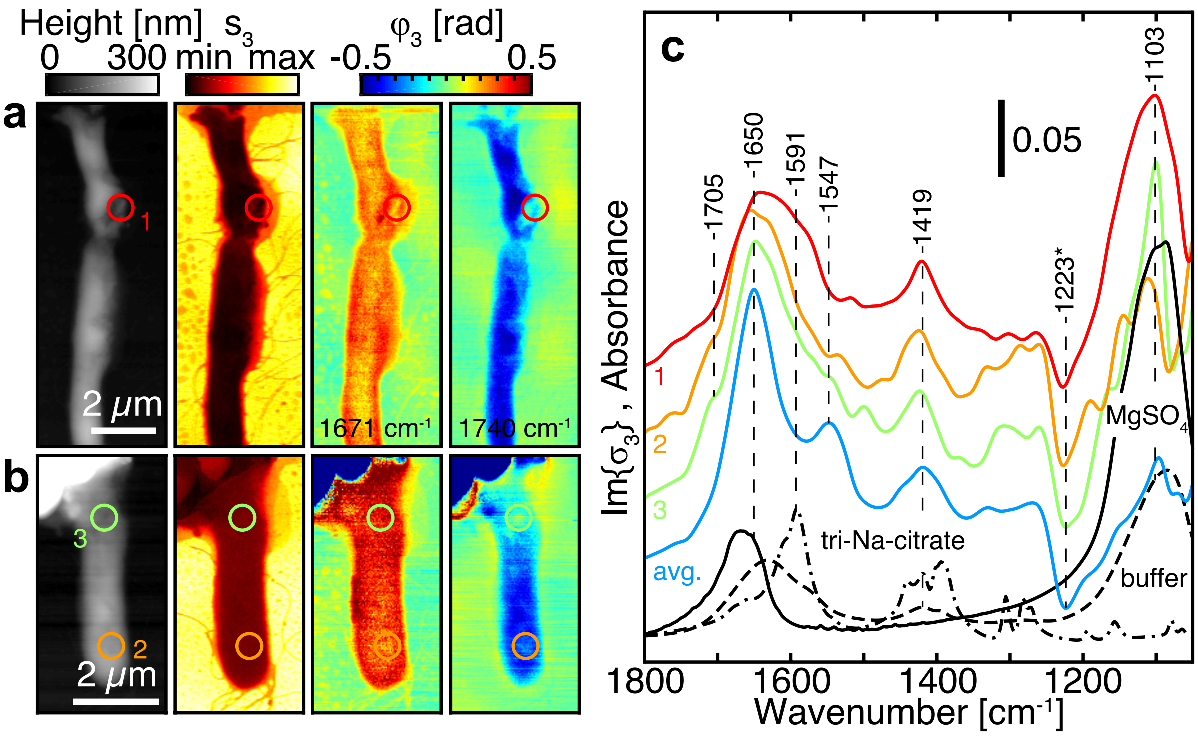

Figure 4.23 (a) & (b) Topography, amplitude s_3 and phase φ_3 maps at 1671 and 1740 cm^{-1} of two individual *H. salinara* of the strain L33. The full phase retrieval was applied to *s*SNOM maps (see Sec. 2.3.1).[98] **(c)** nano-FTIR spectra of heterogeneous spots on L33 cells (red,orange, green, 8 cm^{-1} resolution, 0.3 kHz scanner speed, n = 3) and average nano-FTIR spectrum on homogeneous spots (cyan). KBr-FTIR spectra (black lines) of $MgSO_4 \cdot 7\ H_2O$ (solid), tri-Na-citrate (dot-dashed) and ATR-FTIR spectrum (black dashed) of the used buffer. Absorbance spectra were scaled (x 0.5).

might resemble a composition of ν(C=O) (1709 cm^{-1}, protonated) and ν_{as}(O-C-O) (1591 cm^{-1}, deprotonated) of the citrate[206] and modes from SO_4^{2-} (< 1200 cm^{-1})[204] crystallized on top of the cell. In contrast to that, it is not apparent why citrate should co-crystallize with $MgSO_4$ at only few locations (compare discussion of Fig. 4.24 below).

Alternatively, bands besides the protein related amide I or amide II modes might be associated with vibrations of localized DNA or glycoprotien from the S-layer. Since all irregular spots found are located in cells which seem to stick next to another cell, this could mean that they just have divided and the DNA is still in a condensed, localized state. Although DNA shows corresponding bands around 1720 cm^{-1} (ν(C=O) of purine and pyrimidine) and 1660 cm^{-1} (ν(C=O) & δ(N-H)), it should as well exhibit two very strong bands of the ν_{as}(PO_2^-) ($\sim$ 1225 cm^{-1}) and ν_s(PO_2^-) ($\sim$1080 cm^{-1}) of its phosphate backbone, of which the first one not present.[207] To exclude that the negative band of SiO_2 is obscuring the asymmetric stretching band, the phase spectra of the substrate and sample were inspected separately (Fig. A.8). The sample phase spectrum does not show the ν_{as}(PO_2^-). Additionally, there is no rational to assume a non-random orientation of the phosphate groups of DNA which would justify that the asymmetric stretching vibration is not probed due to the surface selection rules. Those observations disfavor the assignment of those spots to DNA.

The glycoprotein in the S-layer of those archaea is loaded with metabolized sulfate,[199] which could be an alternative origin of the absorption around 1103 cm^{-1}. This hypothesis might be supported by the fact that polysaccharides (of deep-sea bacteria) exhibit a strong band around 1630 cm^{-1} and relative to that weaker contribution around 1730 cm^{-1} as well as contributions between 1200-900 cm^{-1}.[208] This interpretation could not be verified due to lacking spectroscopic data on the isolated S-layer. Furthermore, the S-layer surrounds the archeal cells homogeneously, stabilizing it in a rod-like shape at optimal salt concentrations[209] and, thus, would need to be found in all near-field spectra on the homogeneous spots to a similar extent. Yet, the S-layer is prone to get "lost during prolonged cultivation under laboratory conditions"[210] and those irregular sites are exhibit residuals of the S-layer. Concluding on the chemical composition or biological origin of these sites, thus, remains not feasible.

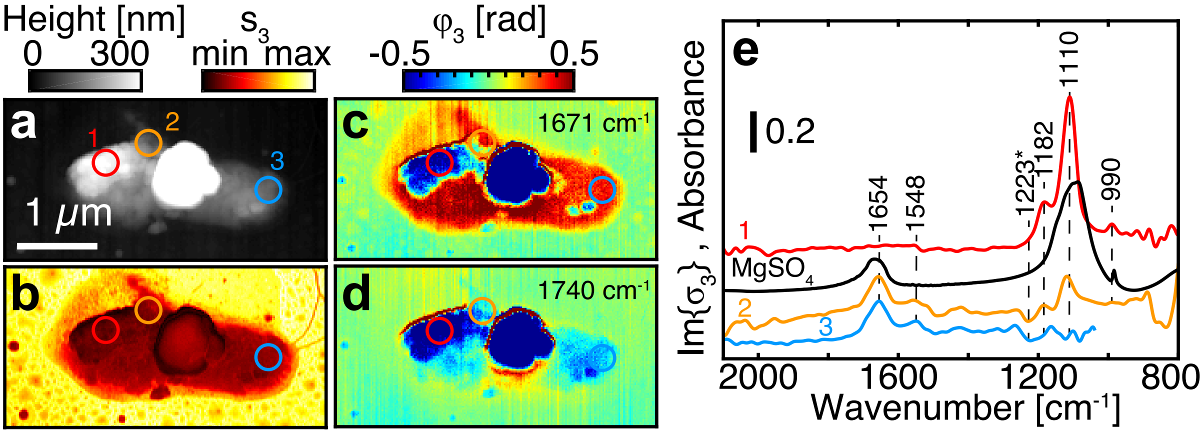

Figure 4.24 Topography (a), amplitude s_3 (b) and phase φ_3 maps at 1671 cm^{-1} (c) and 1740 cm^{-1} (d) of an individual *H. salinarum* cell of the strain S9. The full phase retrieval was applied to *s*SNOM maps (see Sec. 2.3.1).[98] **(e)** nano-FTIR spectra of different spots (red, orange, cyan, 8 cm^{-1} resolution, 0.3 kHz scanner speed, n = 3). KBr-FTIR spectrum (black) of $MgSO_4 \cdot 7\ H_2O$ (scaled x 0.5).

Figure 4.24a-d shows topography (a) and *s*SNOM amplitude s_3 (b) and phase φ_3 maps at 1671 cm^{-1} (c) and 1740 cm^{-1} (d) of an individual S9 cell heavily covered by crystalline residuals. The topography clearly shows a large crystal in the cells center (∼600 nm) and a thinner crust on the left edge. Although the amplitude s_3 does not discriminate between salt and cell the phase decreases drastically as seen before. Correlating the phase φ_3 at 1740 cm^{-1} with the height at each pixel shows a steady decrease of the phase with increasing tip-substrate separation (see Sec. A.12 & Fig. A.9). The higher the non-resonant feature, the lower the phase. The decrease of the phase is approximately linear upto features as high as 600 nm. This could indicate that the suggested shift of the antenna resonance upon loading with the salts dielectric environment is less probable than a phase delay due to indirect illumination paths[132] (as discussed in Sec. 4.2.1) since the antenna resonance will be affected only by matter within its near-field which typically decays exponentially within tens of nm.[194,195]

Near-field spectra were acquired on the crystals with an extended spectral range of 800 - 2000 cm^{-1} (Fig. 4.24e) as described in ref[46] to resolve the $SO_4{}^{2-}$ modes in the range of 900 - 1200 cm^{-1} attributed to the $MgSO_4$ present in the used buffer. Spectra at the specified spots were recorded with two different emission characteristics of the DFG laser and spectrally cross-faded during post-processing (red and orange trace in Fig. 4.24e). The composite spectra, both on and near the crystalline debris (1 & 2), show two major bands at 1182 cm^{-1} and 1110 cm^{-1}. Both can be assigned to $SO_4{}^{2-}$ stretching modes, although they appear to be sharper in the KBr-FTIR spectrum (black trace).[199,204] A third weak band rises only for the spectrum taken on the high crust at 990 cm^{-1} which corresponds well to the far-field spectrum and literature of $MgSO_4$.[199] Interestingly, the crystalline substances covering the cells only show bands specific to $SO_4{}^{2-}$ but not to citrate as previously speculated (see above, Fig. 4.23c). This result might discourage the interpretation of the near-field spectra of the irregular spots shown in Fig. 4.23c as crystalline citrate but favors either of the interpretations as condensed DNA or residuals of the S-layer.

4.2.3 Near-Field Spectroscopy on Resonant Plasmonic Antennas

As described above, IR-*s*SNOM provides a promising platform for IR nanospectroscopy with potential single-molecule sensitivity. Still, it lacks approximately one to two orders of magnitude of SNR to detect single proteins (see Sec. 4.2.1). Thus, strategies for increasing the SNR are necessary, many of which were reported in the last years. Light sources with higher brilliance and lower noise were tested (e.g. synchrotron radiation,[211] DFG based fs-laser system[137] and laser-driven plasma sources[212]). For most of these sources the output power is sufficient to operate the commonly used MCT detectors in saturation.[213] Although alternatives like single-photon detectors are already being tested for various mid-infrared applications,[214–216] they are not yet commercially available or need expensive cryogenic cooling to liquid helium temperatures. As a consequence, MCTs are almost exclusively used in IR near-field spectroscopy. Alternative strategies are tuning the tip-sample interaction by engineering the tip or the substrate. The use of full metal resonant tips showed only a minor increase of about a factor of two in amplitude.[94] Using resonant substrates instead of resonant tips will be discussed in the following paragraphs. All measurements shown in the following section were performed together with Dr. Marta Autore in the group of Prof. Dr. Rainer Hillenbrand at CICnanoGune in San Sebastian (Spain, 2016). For these measurements a commercially available *s*SNOM system from NeaSpec was used. The samples were kindly provided by Dr. Saül Vélez (CICnanoGune, San Sebastian, Spain).

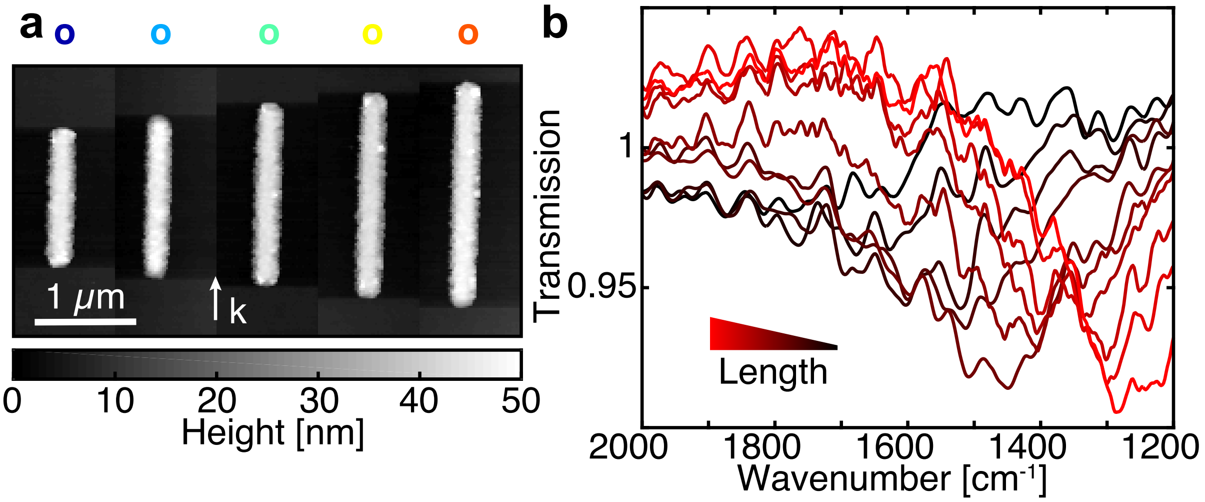

Figure 4.25 (a) Concatenated AFM topographies of single linear gold antennas evaporated on CaF_2. **(b)** Transmission FTIR spectra using a microscope. The antennas could not be identified by length due to insufficient resolution of the Cassegrain objective.

The optical antennas with length ranging from 1.4 μm to 2.2 μm (Fig. 4.25a) were defined by electron-beam lithography followed by physical vapor deposition of gold on the CaF_2 substrate. Acquisition of transmission spectra on single antennas was attempted (Fig. 4.25b). The individual spectra could not be assigned to a definite antenna length, due to the low magnification objective used. However, we can appreciate a trend correlating a length increase to the transition from the black to the red spectrum. The expected decrease of the plasmonic resonance frequency ω_{res} for longer antennas clearly resembles such a trend.

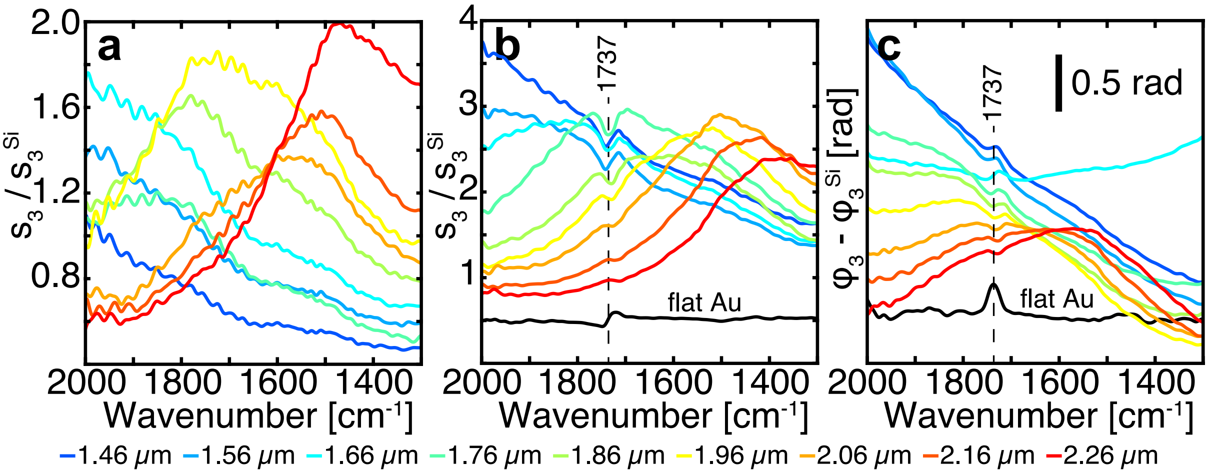

Figure 4.26 **(a)** nano-FTIR amplitude spectra s_3/s_3^{Si} normalized to silicon of bare linear gold antennas with lengths L = 1.46 ... 2.26 μm (see color code). **(b)** nano-FTIR ampltude spectra of linear gold antennas of the same length coated with 20 nm of PMMA. The black spectrum depicts the spectrum acquired on a flat, unstructured gold surface. **(c)** nano-FTIR phase spectra $\varphi_3 - \varphi_3^{Si}$ of the PMMA coated antennas.

For near-field spectroscopy on single optical antennas, the antennas were placed such that the long axis points along the k-vector of the incident light. Due to an AOI of $\sim 60°$, the phase retardation makes the antenna tip averted from the source appear brighter in the near-field amplitude maps (see Sec. A.11).[217] To acquire spectra with the highest intensity, all following spectra were recorded on the bright end of each antenna. Figure 4.26a shows amplitude spectra s_3 of those linear antennas whose lengths range from 1.46 μm to 2.26 μm. The spectra are referenced to a spectrum recorded on silicon which might introduce a certain ambiguity in the absolute intensity due to different alignment of the system, but offered a spectrally flatter reference. The relative intensities of the antennas' spectra are not homogeneous and the lineshape of their resonance follows a typical Lorentzian-like one, although corrupted by noise. However, the linear scaling of the antennas' resonance wavelength λ_{res} with its length, as common for optical antennas,[68] can be inferred by fitting a Lorentzian profile to Figure 4.26a, b (see Fig. A.12).

To understand the benefit of using resonant linear optical antennas as an enhancing substrate for nano-FTIR, a set of antennas with the same dimensions (but coated with a homogeneous 20 nm thick layer of PMMA) was investigated. Figure 4.26b-c shows amplitude (b) and phase (c) spectra of those antennas. The color code was chosen such that the nominal length corresponds to the ones from Figure 4.26. As a reference, the spectrum of a PMMA film of the same thickness deposited on an unstructured flat gold surface is plotted in both panels (black, referenced against bare flat gold). In both graphs, a clear feature at 1737 cm^{-1} can be observed. This is typical for the ν(C=O) (= ω_{vib}) of PMMA, although slightly upshifted by ∼5 cm^{-1} due to the low thickness (∼20 nm) of the film,[184] as discussed above (Sec. 4.2.1). The dispersive lineshapes (black trace in Fig. 4.26) in the amplitude spectra typical for *s*SNOM spectra are converted to asymmetric Fano-type lineshapes (Sec. 2.2.4), which are often found for vibrational bands, enhanced by resonant optical antennas.[77,78] Here, the lineshape critically depends on the coupling of the vibrational band and the broad plasmonic resonance as well as the tuning ratio $\omega_{\text{vib}}/\omega_{\text{res}}$. The closer the antennas mode is tuned to the ν(C=O), the more intense its contrast gets in the near-field amplitude spectra. Interestingly, the contrast in the phase spectrum is apparently reduced over the one on bare gold and seems to be less affected by the antennas resonance frequency. The maximal scattering near-field amplitude is increased by a factor of up to three when ω_{vib} and ω_{res} are well in alignment (cyan trace in Fig. 4.26b).

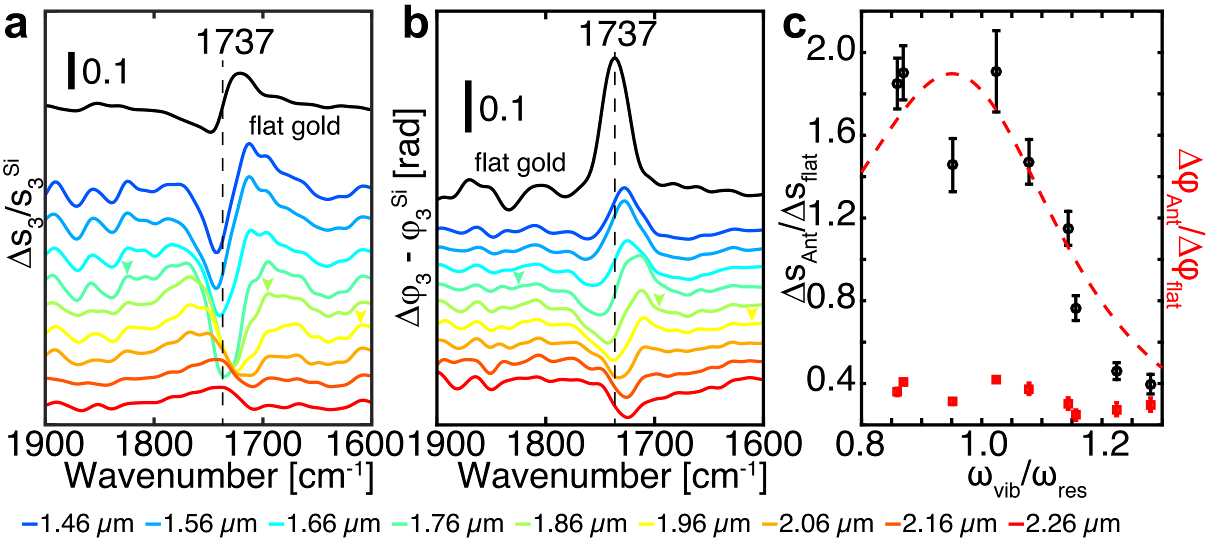

Figure 4.27 Baseline subtracted lineshapes of the ν(C=O) of the amplitude **(a)** and phase **(b)** spectra for different antenna length. The arrows indicate the resonance frequency of the PMMA coated antenna (for the blue and red spectra the resonance frequency is out of range in this graph). The black line indicates the spectra acquired on a flat unstructured gold substrate. **(c)** Amplitude (black) and phase (red) contrast normalized to the contrast of PMMA on an unstructured gold surface.

Figure 4.27 displays the lineshape of the ν(C=O) at the individual tuning ratios. For clarity, a polynomial baseline was subtracted from the amplitude and phase spectra in Figure 4.26b & c. For tuning ratios $\omega_{\text{vib}}/\omega_{\text{res}} > 1$ the maximum near-field amplitude signal is blue shifted compared to ω_{vib}. For decreasing tuning ratios, the lower frequency minimum exhibits a blue shift instead. In the phase spectra the lineshape evolves from an anti-absorptive, over dispersive to absorptive lineshape with decreasing the tuning ratio. The amplitude spectra qualitatively coincide with what is expected from far-field experiments.[78]

To compare the near-field amplitude contrast $\Delta s = s_{max} - s_{min}$ and phase contrast $\Delta\varphi = \varphi_{\text{max}} - \varphi_{\text{min}}$ of the vibrational signal, they are normalized to the contrast Δs_{flat} and $\Delta\varphi_{\text{flat}}$ of PMMA on a flat unstructured gold surface (Fig. 4.27c). The near-field amplitude contrast is almost enhanced by a factor of two at a tuning ratio $\omega_{\text{vib}}/\omega_{\text{res}}$ close to 1. Detuning the antennas' resonance off the molecular vibration rapidly decreases the relative contrast enhancement below 1. This means that the antennas enhancement is worse than the unstructured gold's. The red dashed line indicates a Lorentzian fitted to the relative amplitude contrasts as guide to the eye. The maximum relative enhancement is shifted by 5 % to lower tuning ratios. This behavior was already predicted in earlier theoretical and experimental work on resonant optical antennas.[78,218] However, the relative phase contrast is less affected by the tuning ratio and stays, even for matching both the molecular oscillator and plasmonic resonance, below 0.5.

These results indicate that the spectra are mainly showing features attributed to the antennas in this experiments, although the dipolar antenna resonance is disturbed by the metallic tip.[219] If this is the case, the antenna reports its dielectric environment to the far-field via the tip. This suggests that the amount of sensed PMMA is substantially larger than the volume sensed by the tip itself. Assuming a half-sphere with radius of 30 nm (typical lateral resolution of *s*SNOM) for the volume sensed by the tip. Even if just the tips of the resonant antenna were to contribute to the enhanced signal (first 100 nm of the antennas tip)[220] and the whole 20 nm of PMMA surrounding it were sensed homogeneously, the contrast in spectra of the antenna would correspond to ~20 times more molecules compared to the tip placed on a continuous, 20 nm thick film of PMMA. This deteriorates the figure of merit using resonant metal antennas in a *s*SNOM, particularly for single-molecule detection. Additional experiments will be necessary to verify this.

In addition to the moderate enhancement of amplitude contrast and diminished phase contrast, one might consider the distorted lineshape as another parameter when comparing antenna enhanced near-field spectra with near-field spectra acquired on a flat gold substrate. For non-resonant substrates, theory explaining most band shapes observed in the experiments is already available.[90,101,221] In contrast, an *a priori* interpretation of vibrational frequencies and relative band intensities is complicated by the Fano-type band shape due to the sample-antenna interaction.

4.2.4 Near-Field-Induced Magneto-Caloritronic Nanoscopy of Ferromagnetic Domains

The development of high-density magnetic storage and spintronic devices calls for microscopic magnetic techniques, enabling the investigation of nanoscale magnetic phenomena at relevant length and time scales.[222,223] Although ultrafast X-ray microscopy offers the desired specifications,[224] it's limited to expensive synchrotron beamlines. Alternatives like the magneto-optical Kerr effect (MOKE) are spatially limited by diffraction, and magnetic force microscopy (MFM)[225] or nitrogen vacancy center microscopy[226] potentially affect pinned DWs. As already suggested in theoretical studies,[227] using the optical near-field at the apex of a SPM probe generates a local heater. The local magnetization state can then be read out via the ANE (see Sec. 2.4) with a lateral resolution beyond 100 nm.

The following section describes the working principle and outlines first results achieved with sub-wavelength imaging of magnetic domains. The data presented here were acquired together with Bernd Kästner (Physikalisch Technische Bundesanstalt, Berlin, Germany) using the *s*SNOM described in this thesis. The samples were prepared and previously analyzed by Murat Cubukcu (Cavendish Laboratory, University of Cambridge, Cambridge, UK) and Joerg Wunderlich (Hitachi Cambridge Laboratory, Cambridge, UK and Institute of Physics ASCR, Praha, Czech Republic)

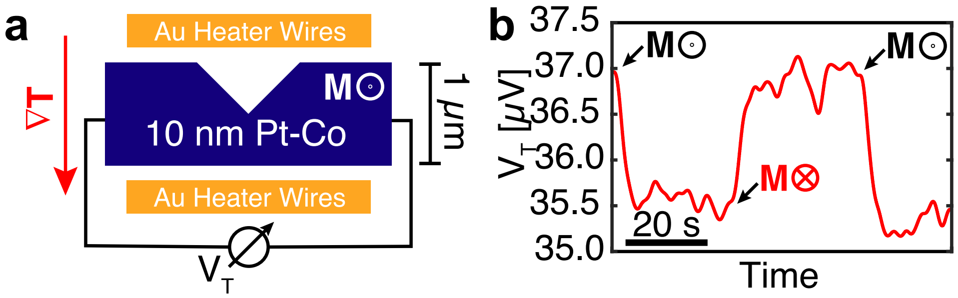

Figure 4.28 (a) Schematic layout or the magnetic device used in the following experiments. Gold heaters are additionally placed close to the magnetic wire, in order to generate a thermal gradient by resistive heating of the gold wires. **(b)** EMF V_T demodulated at the frequency of the switching temperature gradient induced by the gold heaters. The magnetization of the Pt-Co bar was switched between $\pm M_S \mathbf{e}_z$ by approaching a hand held magnet (arrows).

Before carrying out near-field mapping of the EMF, V_T, we tested the device for response to an external temperature gradient *in situ* on the AFM stage. Each device had gold wires deposited next to the magnetic wire (Fig. 4.28a). Applying an alternating voltage to the upper or lower heater gold wire generates an external temperature gradient ∇T. The heater wires were switched on and off with a frequency of ω = 310 Hz. The generated EMF was analyzed by a LIA (Fig. 4.28b). The magnetization of the Pt-Co wire was externally switched between its saturation magnetizations $\pm M_S \mathbf{e}_z$ by approaching a hand held magnet to the wire. The moments corresponding to the switching are indicated by the arrows in Figure 4.28b. The reversible switching of V_T upon reversal of $\mathbf{M}$ suggests that the ANE effect can be properly observed. The large offset, approximately $\sim$ 20 times the difference between switching the magnetization, might be due to capacitive or inductive coupling of the heater wires to the magnetic wire.

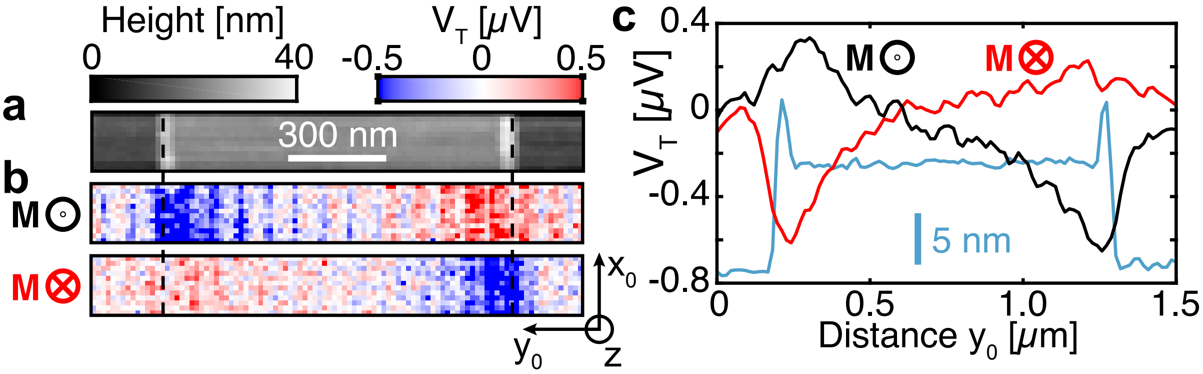

Figure 4.29 (a) Topography of the magnetic wire. **(b)** EMF ($V_T^{\uparrow\downarrow}$) maps far off the notch for two opposing magnetizations $\mathbf{M}^{\uparrow\downarrow} = \pm M_S \mathbf{e}_z$ ($\mathbf{M}^{\downarrow}$ red and $\mathbf{M}^{\uparrow}$ black). A constant background was subtracted from the data. **(c)** The EMF maps of (b) are averaged and smoothed. The blue line indicates the cross-section of the magnetic microbar averaged along the x_0-axis.

Figure 4.29a shows the topography of the wire taken far off the triangular notch. Simultaneously to scanning the wire underneath tip, the generated EMF ($V_T^{\uparrow\downarrow}$) is demodulated at the tips mechanical resonance frequency Ω and registered for two opposing magnetizations $\mathbf{M}^{\uparrow\downarrow} = \pm M_S \mathbf{e}_z$ (Fig. 4.29b). A constant background was subtracted from the data. Similar to the offset in Figure 4.28b, the present offset might originate from capacitive or inductive coupling. The magnitude of the offset varied between experiments, which might be a result of the tips being slightly charged, since the tip is mounted on an electrically isolated glass holder. However, the offset stayed constant throughout a single measurement. Qualitatively, the contrast can be understood by focusing only on the contribution of the ANE to Eqn. 2.37

$$V_T(x_0, y_0) = \int_{-l/2}^{l/2} \mathrm{d}x \frac{1}{w(x)} \int_{-w(x)/2}^{w(x)/2} \mathrm{d}y \{-S_\perp \left[\nabla T(x, y, x_0, y_0)\right]_x + \cos\theta(x) S_N \left[\nabla T(x, y, x_0, y_0)\right]_y\} \tag{4.8}$$

where x, y denote the coordinate across the bar and x_0, y_0 the position of the local temperature gradient (i.e. the AFM tip) relative to the magnetic bar with width w and length l. When the tip is in the center of the wire, the induced temperature gradient is symmetric and the EMF generated by the ANE cancels. Once the tip approaches an edge of the wire, the temperature distribution is not symmetric across the wire anymore and the integral yields a finite EMF. The side on which the temperature gradient is diminished, determines the sign of the ANE contribution to the measured EMF. Since the ANE is linear in the magnetization, its reversal delivers the same V_T map, but with opposite sign. When the irradiating laser is blocked, thus, switching off our local heater, the gradient vanishes and only topography-induced edge artifacts reside (Fig. A.13). This result indicates that the contrast in our V_T maps has indeed a magneto-thermal origin. In particular the inversion upon reversal of the magnetic moment strongly suggests that the ANE is the major contribution.

For clarity the EMF maps in Figure 4.29b were averaged along the x_0-direction and smoothed with a 10 point Savitzky-Golay filter (Fig. 4.29c). The cross-section across the wire is indicated by the blue line. The trace is asymmetric towards negative values of the EMF. This asymmetry might be induced by the negative edge artifacts which are present even without illumination thereby adding a negative voltage only at the edges, irrespective of the magnetization. Numerical simulations yield the same anti-symmetric lineshape as seen in Figure 4.29c with comparable absolute amplitudes.[104] A moderate temperature increase of 20-30 K could be inferred from the simulations.

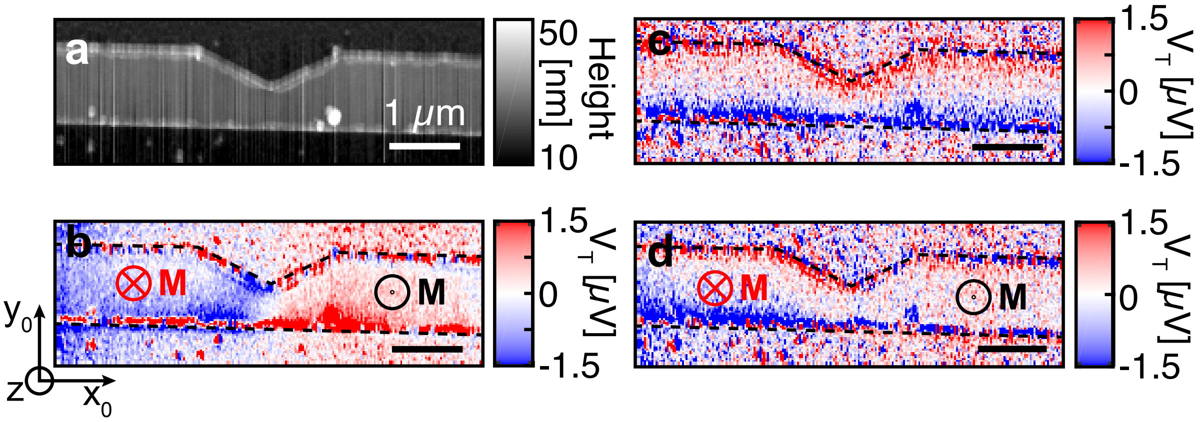

Figure 4.30 (a) Topography of the ferromagnetic device with central notch. **(b)** Simultaneously acquired V_T map when the DW is present. **(c)** Difference of the EMF maps for two opposing (homogeneously) magnetized bars $V_T(\mathbf{M}^{\downarrow}) - V_T(\mathbf{M}^{\uparrow})$. **(d)** Difference of the EMF maps of the bar with a pinned DW and the homogeneously magnetized bar.

To extend this method to the imaging of magnetic domains, a DW was introduced at the central notch (Fig. 4.30a) by applying an external magnetic field.[153] Consequently, the magnetization points out-of-plane (into the image plain, $\mathbf{M}^{\downarrow} = -M_S\mathbf{e}_z$) on the left side of the notch and on the right side out of the image plain ($\mathbf{M}^{\uparrow} = M_S\mathbf{e}_z$). Figure 4.30b shows the EMF $V_T(\mathbf{M}^{\downarrow\uparrow})$ map. Far off the constriction the gradient $[\nabla V_T]_y$ is positive on the left side whereas it is negative on the right side. This is in perfect accordance with the measurements presented in Figure 4.29b-c. In addition to the inverted gradient, another contrast evolves close to the notch. We observed a negative EMF on its left and, positive on its right side. Homogeneously magnetizing the whole bar either $\mathbf{M}^{\downarrow}$ or $\mathbf{M}^{\uparrow}$ and subtracting the corresponding V_T maps, yields Figure 4.30c. Here the contrast around the DW vanishes and only a homogeneous gradient $\left[\nabla V_T\right]_y$ due to the ANE remains. Close to the notch, contributions of the Seebeck effect $S_{\perp}\left[\boldsymbol{\nabla} T\right]_x$ (Eqn. 2.37) do not compensate across the wire and govern the contrast in Figure 4.30b. This contribution is independent of the magnetization and cancels upon subtraction of the two maps $V_T(\mathbf{M}^{\uparrow})$ - $V_T(\mathbf{M}^{\downarrow})$ while the ANE contribution doubles (Fig. 4.30c). This indicates that the contrast close to the notch in Figure 4.30b is indeed due to the Seebeck effect $S_{\perp}$. The position of the DW gets most clear when the $V_T(\mathbf{M}^{\uparrow})$ map of the homogeneously magnetized bar is subtracted from the $V_T(\mathbf{M}^{\downarrow\uparrow})$ map with the DW (Fig. 4.30d). As seen in Figure 4.30c, the additional contribution of the Seebeck effect is eliminated by the subtraction and only the ANE contribution remains. The difference map shows the gradient $\left[\nabla V_T\right]_y$ on the left side of the constriction, whereas the right side appears homogeneous. From this map it can be inferred that the DW must be close to the constriction (at least within one scale bar). However, the SNR in these measurements do not allow to quantify the spatial resolution. Unpublished magneto-caloritronic nanoscopy on anti-ferromagnetic domains yields a sub-wavelength resolution verifying the localization of the near-field induced temperature gradient (oral communication by B. Kästner). This shows the great potential of this method, since it is difficult to spatially resolve the domain structure in antiferromagnetic thin films on the nanoscale with conventional techniques.[222]

5

Conclusion

So far, vibrational spectroscopy of single molecules is exclusively feasible using surface- or tip-enhanced Raman scattering.[26,27] However, this technique is limited mainly to resonantly excited molecules and suffers from photobleaching due to the strong electromagnetic fields in the hot spots.[228] Infrared (IR) spectroscopy is a non-invasive absorption technique that offers vibrational information complementary to Raman spectroscopy.[12,229] In this work, I have presented strategies to push the sensitivity of IR spectroscopy towards the single-molecule regime. Two fundamental approaches – surface-enhancement and tip-enhancement – were applied alongside a novel magneto-caloritronic sensing scheme.

Surface-enhanced IR absorption spectroscopy (SEIRAS) offers the potential to probe the vibrational fingerprint of self-assembled monolayer (SAM) of biomolecules.[17,58] The production of resonant SEIRAS substrates with high enhancement factors (EFs) is typically accompanied by high costs. A low-cost method for preparing resonant substrates was established in this work (Sec. 4.1).[121] Fourier-transform infrared (FTIR) microspectroscopy and finite-difference time-domain computations of the resonant disc antenna arrays (DAAs) suggest a great potential for SEIRAS. The EF of the DAAs is comparable to the enhancement reported for resonant rod-shaped antennas manufactured by expensive and time-consuming methods like electron beam lithography or direct laser writing.[56,74,161,162] pH-induced difference spectra of a 4-mercaptobenzoic acid SAM adsorbed onto the DAAs were acquired. A pH-dependent composition of the vibrational modes of the conjugated phenyl ring was corroborated together with supporting density functional theory computations and mechanical rigidity of the SAMs was verified.[114] In a next step, the DAAs were applied to a complex biological system. Light-induced difference spectra of the membrane protein sensory rhodopsin II from *Natromonas* *pharaonis* (*Np*SRII) were acquired in the extended spectral range from 1800 to 1100 cm^{-1}, inaccessible before.[22] This allowed detecting the photo-stationary M state of $< \sim 6x10^9$ (10^{-15} mol) of active *Np*SRII. The reliable applicability of the DAAs in a wide range of biologically relevant environments (e.g. organic solvents, alkaline and acidic aqueous solutions, exposure to visible light) as well as the broad spectral range 1800 - 1100 cm^{-1} demonstrates their utility in life science. The adaption to setups lacking focusing optics or usage of more brilliant light sources (e.g. synchrotron[55] or difference frequency generation based laser sources[139]) will increase the throughput of photons and the signal-to-noise ratio (SNR), accordingly.

Even better control over local electromagnetic fields can be achieved by a scattering-type scanning near-field optical microscope (*s*SNOM). Here, light scattered by an atomic force microscope (AFM) tip is interferometrically detected, which enables the retrieval of the near-field amplitude and phase.[90,97] The nanoscopic resolution inherited from the AFM makes *s*SNOM a promising tool for single-molecule IR spectroscopy.[14] In this work, I have designed and built a custom *s*SNOM, specialized for life science applications (Sec. 4.2.1). A protein-loaded purple membrane (PM) patch of the archeon *Halobacterium salinarum* (*H. salinarum*)[44,45] was used to characterize its nanoimaging and nanospectroscopic (nano-FTIR) capabilities. Limited by the tip apex radius of ∼25 nm, a lateral resolution of ∼30 nm both in near-field imaging and near-field spectroscopy was routinely achieved.[42] This offered the opportunity to detect ∼400 bacteriorhodopsin (bR) molecules ($\sim 10^{-21}$ mol) with a SNR of ∼10 in imaging mode (*s*SNOM, 390 μs / px) or SNR of ∼40 in spectroscopy mode (nano-FTIR, 6 minutes acquisition time, 1200 - 2000 cm^{-1} spectral range, 4 cm^{-1} spectral resolution). Implementation of a photo-elastic phase modulation was proven to increase the acquisition rate by a factor of 20 compared to conventional piezo-driven phase modulation[97] with no significant decrease in SNR. This paves the way for μs time-resolved nanospectroscopy using *s*SNOM. The use of faster modulators will facilitate video rate *s*SNOM or boost the sensitivity due to stronger averaging. Additionally, a total internal reflection illumination and detection scheme for *s*SNOM was established. I could show that the tip/sample dependency of the demodulated scattered light clearly showed the near-field characteristic exponential decay within ∼60 nm. The strong absorption of the scattered light by bulk water can be avoided with this configuration and, thus, sets the basis for IR-*s*SNOM experiments in aqueous environments.

The halophilic archeon *H. salinarum* carries one the best-studied membrane proteins (bR), which arranges in PM patches in its cellular membrane.[193] Two strains of *H. salinarum* are available of which S9 expresses bR whereas L33 does not. Previous attempts to localize PM patches in single archeal cells by *s*SNOM suggested a homogeneous distribution of the amide I near-field absorption. Interestingly, a near-field absorption at 1740 cm^{-1} at the poles of individual cells was found, atypical for *H. salinara*. To verify these results, S9 and L33 whole cells were nanoimaged by *s*SNOM and individual sub-diffraction spots were spectroscopically characterized by nano-FTIR (Sec. 4.2.2). A homogeneous amide I near-field phase across the *H. salinara* was observed indicating an even protein distribution at least within the cell walls of both strains. This finding is surprising since the membrane of S9 cells should contain highly condensed bR[193] whereas this should not be the case for L33 cells. Near-field spectra acquired locally on those homogeneous spots show high similarity to the far-field spectra supporting a homogeneous protein distribution. Both observations were in line with near-field spectroscopy reported for the topologically similar gram-negative bacterium *Escherichia coli* (*E. coli*).[197,200] In contrast to the spectra of *E. coli*, bands at ∼1100 cm^{-1} were observed and could be attributed to sulfate stretching modes $\nu(\text{SO}_4{}^{2-})$ specific for the used MgSO_4 buffer or the so-called surface layer (S-layer) of *H. salinara*.[199] Irregular spots in the near-field maps showed a vibrational mode composition different to the homogeneous ones. These locations might be attributed to the archeal S-layer, condensed DNA or residual crystallized MgSO_4 or citrate buffer molecules. This set of experiments demonstrates the advantages of the combination of both IR nanoimaging by *s*SNOM and broadband nanospectroscopy by nano-FTIR on complex biological systems.

A combination of surface-enhancement mediated by resonant rod-shaped metal antennas and tip-enhancement through *s*SNOM was evaluated to further enhance the sensitivity of IR spectroscopy (Sec. 4.2.3). Near-field spectra of single antennas of varying length covered with a 20 nm thick poly(methyl methacrylate) (PMMA) layer were acquired. A Fano-like band shape of the near-field phase and near-field amplitude of the enhanced ν(C=O) of PMMA was found. This band shape is typical for enhanced vibrational bands using resonant metal antennas.[28,77] This may indicate that the near-field response of the antenna/tip system is dominated by the far-field characteristics of the antenna. Often, the Fano-like band shape prevents an unambiguous interpretation of complex spectra. Despite the moderate increase of near-field scattered photons and increase in the near-field amplitude contrast, a decrease of the absorptive phase contrast was observed. Thus, the increase in the number of detectable photons is compensated by the decrease of the relevant observable phase contrast. In addition to the lowered contrast, the amount of probed molecules is increased due to the antennas interaction with its surrounding environment further diminishing the figure of merit of this approach. Yet, materials like graphene-covered SiC[230] or graphene resonators[231–233] as an enhancing substrate might bear alternatives to reinforce the sensitivity of *s*SNOM.

New strategies to enhance the contrast in *s*SNOM are indispensable. Nanoimaging the magnetization, a magneto-caloritronic method[227] was established for which the illuminated tip serves as a nanoscopic "heater" (Sec. 4.2.4).[104] The resulting temperature gradient induces an electromotive force due to the anomalous Nernst effect, which can be read out electronically while scanning the tip across the magnetic device. A single domain wall (DW) was localized in a ferromagnetic micro-device as a model system. Our unprecedented thermo-caloritronic technique is non-invasive (in contrast to magnetic force microscopy, which can shift the DWs via stray fields of the magnetic probe)[225] and allows imaging of magnetic domains in ferromagnetic[104] and even antiferromagnetic systems. The temperature rise underneath the tip in a typical *s*SNOM experiment was estimated to be 20-30 K at 50 mW laser power by comparison to computational modeling. This concept will be extended to vibrational nanospectroscopy. A sample of interest is applied to the magnetic device and enhances the temperature gradient when the quantum cascade laser (QCL) is tuned to an IR absorption band specific to sample. In contrast, the temperature gradient is diminished when the QCL is detuned from the absorption band.

The strategies to boost the sensitivity and spatial resolution of IR spectroscopy presented here pave the way towards new spectroscopic modalities in general and for single-molecule vibrational spectroscopy in particular.

References

[1] Overington, J. P., Al-Lazikani, B. & Hopkins, A. L. How many drug targets are there? *Nat. Rev. Drug Discov.* **5**, 993–996 (2006).

[2] Walter, N. G., Huang, C. Y., Manzo, A. J. & Sobhy, M. A. Do-it-yourself guide: How to use the modern single-molecule toolkit. *Nat. Methods* **5**, 475–489 (2008).

[3] Yu, J. Single-Molecule Studies in Live Cells. *Annu. Rev. Phys. Chem.* **67**, 565–585 (2016).

[4] Khademi, S. Mechanism of Ammonia Transport by Amt/MEP/Rh: Structure of AmtB at 1.35 A. *Science* **305**, 1587–1594 (2004).

[5] Adachi, M. *et al.* Structure of HIV-1 protease in complex with potent inhibitor KNI-272 determined by high-resolution X-ray and neutron crystallography. *Proc. Natl. Acad. Sci. U. S. A.* **106**, 4641–6 (2009).

[6] Merk, A. *et al.* Breaking Cryo-EM Resolution Barriers to Facilitate Drug Discovery. *Cell* **165**, 1698–1707 (2016).

[7] Aquila, A. *et al.* Time-resolved protein nanocrystallography using an X-ray free-electron laser. *Opt. Express* **20**, 2706 (2012).

[8] Nogly, P. *et al.* Retinal isomerization in bacteriorhodopsin captured by a femtosecond x-ray laser. *Science* **0094**, 1–15 (2018).

[9] Chen, B. *et al.* Structural Dynamics of Ribosome Subunit Association Studied by Mixing-Spraying Time-Resolved Cryogenic Electron Microscopy. *Structure* **23**, 1097–1105 (2015).

[10] Fitzpatrick, A. W. P., Vanacore, G. M. & Zewail, A. H. Nanomechanics and intermolecular forces of amyloid revealed by four-dimensional electron microscopy. *Proc. Natl. Acad. Sci. U. S. A.* **112**, 3380–3385 (2015).

[11] Byler, D. M. & Susi, H. Examination of the secondary structure of proteins by deconvolved FTIR spectra. *Biopolymers* **25**, 469–487 (1986).

[12] Barth, A. Infrared spectroscopy of proteins. *BBA - Bioenergetics* **1767**, 1073–1101 (2007).

[13] Neumann-Verhoefen, M.-K. *et al.* Ultrafast infrared spectroscopy on channelrhodopsin-2 reveals efficient energy transfer from the retinal chromophore to the protein. *J. Am. Chem. Soc.* **135**, 6968–76 (2013).

[14] Xu, X. G., Rang, M., Craig, I. M. & Raschke, M. B. Pushing the Sample-Size Limit of Infrared Vibrational Nanospectroscopy: From Monolayer toward Single Molecule Sensitivity. *J. Phys. Chem. Lett.* **3**, 1836–1841 (2012).

[15] Lasch, P. & Naumann, D. Spatial resolution in infrared microspectroscopic imaging of tissues. *BBA - Biomembranes* **1758**, 814–829 (2006).

[16] Rigler, P. *et al.* Downscaling Fourier Transform Infrared Spectroscopy to the Micrometer and Nanogram Scale: Secondary Structure of Serotonin and Acetylcholine Receptors. *Biochemistry* **42**, 14017–14022 (2003).

[17] Hartstein, A., Kirtley, J. R. & Tsang, J. C. Enhancement of the Infrared Absorption from Molecular Monolayers with Thin Metal Overlayers. *Phys. Rev. Lett.* **45**, 201–204 (1980).

[18] Osawa, M. Dynamic Processes in Electrochemical Reactions Studied by Surface-Enhanced Infrared Absorption Spectroscopy (SEIRAS). *Bull. Chem. Soc. Jpn.* **70**, 2861–2880 (1997).

[19] Ataka, K. *et al.* Oriented attachment and membrane reconstitution of his-tagged cytochrome c oxidase to a gold electrode: In situ monitoring by surface-enhanced infrared absorption spectroscopy. *J. Am. Chem. Soc.* **126**, 16199–16206 (2004).

[20] Kunimatsu, K., Senzakib, T., Tsushimac, M. & Osawaa, M. C. A combined surface-enhanced infrared and electrochemical kinetics study of hydrogen adsorption and evolution on a Pt electrode. *Chem. Phys. Lett.* **401**, 451–454 (2005).

[21] Barriet, D., Yam, C. M., Shmakova, O. E., Jamison, A. C. & Lee, T. R. 4-mercaptophenylboronic acid SAMs on gold: Comparison with SAMs derived from thiophenol, 4-mercaptophenol, and 4-mercaptobenzoic acid. *Langmuir* **23**, 8866–8875 (2007).

[22] Jiang, X. *et al.* Resolving voltage-dependent structural changes of a membrane photoreceptor by surface-enhanced IR difference spectroscopy. *Proc. Natl. Acad. Sci. U. S. A.* **105**, 12113–7 (2008).

[23] Baumann, A. *et al.* In-Situ Observation of Membrane Protein Folding during Cell-Free Expression. *PLoS One* **11**, e0151051 (2016).

[24] Harris, N. J. *et al.* Structure formation during translocon-unassisted co-translational membrane protein folding. *Sci. Rep.* **7**, 8021 (2017).

[25] Bao, W.-J., Li, J., Cao, T.-Y., Li, J. & Xia, X.-H. Chain-length dependent interfacial immunoreaction kinetics on self-assembled monolayers revealed by surface-enhanced infrared absorption spectroscopy. *Talanta* **176**, 124–129 (2018).

[26] Kneipp, K. *et al.* Single Molecule Detection Using Surface-Enhanced Raman Scattering (SERS). *Phys. Rev. Lett.* **78**, 1667–1670 (1997).

[27] Zhang, R. *et al.* Chemical mapping of a single molecule by plasmon-enhanced Raman scattering. *Nature* **498**, 82–6 (2013).

[28] Neubrech, F., Huck, C., Weber, K., Pucci, A. & Giessen, H. Surface-enhanced infrared spectroscopy using resonant nanoantennas. *Chem. Rev.* **117**, 5110–5145 (2017).

[29] Rotenberg, N. & Kuipers, L. Mapping nanoscale light fields. *Nat. Photonics* **8**, 919–926 (2014).

[30] Maier, S. A. *Plasmonics: Fundamentals and Applications* (Springer US, New York, NY, 2007).

[31] Neubrech, F. *et al.* Spatial extent of plasmonic enhancement of vibrational signals in the infrared. *ACS Nano* **8**, 6250–6258 (2014).

[32] Limaj, O. *et al.* Infrared Plasmonic Biosensor for Real-Time and Label-Free Monitoring of Lipid Membranes. *Nano Lett.* **16**, 1502–1508 (2016).

[33] Abbe, E. Beiträge zur Theorie des Mikroskops und der mikroskopischen Wahrnehmung. *Arch. für Mikroskopische Anat.* **9**, 456–468 (1873).

[34] Zayats, A. & Richards, D. (eds.) *Nano-Optics and Near-Field Optical Microscopy* (Artech House, Norwood, MA 02062, 2009).

[35] Synge, E. A suggested method for extending microscopic resolution into the ultra-microscopic region. *London, Edinburgh, Dublin Philos. Mag. J. Sci.* **6**, 356–362 (1928).

[36] Synge, E. An application of piezo-electricity to microscopy. *London, Edinburgh, Dublin Philos. Mag. J. Sci.* **13**, 297–300 (1932).

[37] Ash, E. A. & Nicholls, G. Super-resolution aperture scanning microscope. *Nature* **237**, 510–512 (1972).

[38] Pohl, D. W., Denk, W. & Lanz, M. Optical stethoscopy: Image recording with resolution $\lambda/20$. *Appl. Phys. Lett.* **44**, 651–653 (1984).

[39] Zenhausern, F., O'Boyle, M. P. & Wickramasinghe, H. K. Apertureless near-field optical microscope. *Appl. Phys. Lett.* **65**, 1623–1625 (1994).

[40] Zenhausern, F., Martin, Y. & Wickramasinghe, H. K. Scanning interferometric apertureless microscopy: optical imaging at 10 angstrom resolution. *Science* **269**, 1083–5 (1995).

[41] Huber, A. J., Keilmann, F., Wittborn, J., Aizpurua, J. & Hillenbrand, R. Terahertz Near-Field Nanoscopy of Mobile Carriers in Single Semiconductor Nanodevices. *Nano Lett.* **8**, 3766–3770 (2008).

[42] Mastel, S. *et al.* Understanding the Image Contrast of Material Boundaries in IR Nanoscopy Reaching 5 nm Spatial Resolution. *ACS Photonics* **5**, 3372–3378 (2018).

[43] Ballout, F. *et al.* Scanning near-field IR microscopy of proteins in lipid bilayers. *Phys. Chem. Chem. Phys.* **13**, 21432 (2011).

[44] Amenabar, I. *et al.* Structural analysis and mapping of individual protein complexes by infrared nanospectroscopy. *Nat. Commun.* **4**, 2890 (2013).

[45] Berweger, S. *et al.* Nano-Chemical Infrared Imaging of Membrane Proteins in Lipid Bilayers. *J. Am. Chem. Soc.* **135**, 18292–18295 (2013).

[46] Amenabar, I. *et al.* Hyperspectral infrared nanoimaging of organic samples based on Fourier transform infrared nanospectroscopy. *Nat. Commun.* **8**, 14402 (2017).

[47] Gamage, S. *et al.* Probing structural changes in single enveloped virus particles using nano-infrared spectroscopic imaging. *PLoS One* **13**, 1–12 (2018).

[48] Khatib, O. *et al.* Graphene-based Platform for Infrared Near-Field Nano-Spectroscopy of Water and Biological Materials in an Aqueous Environment. *ACS Nano, Accept.* **9**, 7968–7975 (2015).

[49] Adato, R. & Altug, H. In-situ ultra-sensitive infrared absorption spectroscopy of biomolecule interactions in real time with plasmonic nanoantennas. *Nat. Commun.* **4**, 2154 (2013).

[50] Griffiths, P. R. & de Haseth, J. A. *Fourier Transform Infrared Spectrometry* (John Wiley & Sons, Inc., Hoboken, NJ, USA, 2007).

[51] Muller, E. A., Pollard, B. & Raschke, M. B. Infrared chemical nano-imaging: Accessing structure, coupling, and dynamics on molecular length scales. *J. Phys. Chem. Lett.* **6**, 1275–1284 (2015).

[52] Osawa, M. Surface-Enhanced Infrared Absorption Spectroscopy. In Chalmers, J. M. & Griffiths, R. P. (eds.) *Handb. Vib. Spectrosc.*, 785–799 (Wiley, Chichester, 2002), 1 edn.

[53] Bao, W.-J. *et al.* Distance-determined sensitivity in attenuated total reflection-surface enhanced infrared absorption spectroscopy: aptamer–antigen compared to antibody–antigen. *Chem. Commun.* **50**, 7787 (2014).

[54] Bochterle, J., Neubrech, F., Nagao, T. & Pucci, A. Angstrom-Scale Distance Dependence of Antenna-Enhanced Vibrational Signals. *ACS Nano* **6**, 10917–10923 (2012).

[55] Neubrech, F. *et al.* Resonant plasmonic and vibrational coupling in a tailored nanoantenna for infrared detection. *Phys. Rev. Lett.* **101**, 2–5 (2008).

[56] Adato, R. *et al.* Ultra-sensitive vibrational spectroscopy of protein monolayers with plasmonic nanoantenna arrays. *Proc. Natl. Acad. Sci. U. S. A.* **106**, 19227–19232 (2009).

[57] Weber, K. *et al.* Wavelength Scaling in Antenna-Enhanced Infrared Spectroscopy: Toward the Far-IR and THz Region. *ACS Photonics* **4**, 45–51 (2017).

[58] Ataka, K., Stripp, S. T. & Heberle, J. Surface-enhanced infrared absorption spectroscopy (SEIRAS) to probe monolayers of membrane proteins. *BBA - Biomembranes* **1828**, 2283–2293 (2013).

[59] Mayerhöfer, T. G. & Popp, J. Periodic array-based substrates for surface-enhanced infrared spectroscopy. *Nanophotonics* **7**, 39–79 (2018).

[60] Li, J. *et al.* Attenuated Total Reflection Surface-Enhanced Infrared Absorption Spectroscopy: a Powerful Technique for Bioanalysis. *J. Anal. Test.* **1**, 8 (2017).

[61] Osawa, M., Ataka, K.-i., Yoshii, K. & Yotsuyanagi, T. Surface-enhanced infrared ATR spectroscopy for in situ studies of electrode/electrolyte interfaces. *J. Electron Spectros. Relat. Phenomena* **64-65**, 371–379 (1993).

[62] Nishikawa, Y., Nagasawa, T., Fujiwara, K. & Osawa, M. Silver island films for surface-enhanced infrared absorption spectroscopy: effect of island morphology on the absorption enhancement. *Vib. Spectrosc.* **6**, 43–53 (1993).

[63] Kratz, C., Oates, T. W. H. & Hinrichs, K. Optimization and quantification of surface enhanced infrared absorption using gradient gold island films. *Thin Solid Films* **617**, 33–37 (2015).

[64] Ataka, K. & Heberle, J. Biochemical applications of surface-enhanced infrared absorption spectroscopy. *Anal. Bioanal. Chem.* **388**, 47–54 (2007).

[65] Bao, W.-J. *et al.* Au/ZnSe-Based Surface Enhanced Infrared Absorption Spectroscopy as a Universal Platform for Bioanalysis. *Anal. Chem.* **90**, 3842–3848 (2018).

[66] Enders, D. & Pucci, A. Surface enhanced infrared absorption of octadecanethiol on wet-chemically prepared Au nanoparticle films. *Appl. Phys. Lett.* **88**, 184104 (2006).

[67] Adato, R., Aksu, S. & Altug, H. Engineering mid-infrared nanoantennas for surface enhanced infrared absorption spectroscopy. *Mater. Today* **18**, 436–446 (2015).

[68] Novotny, L. Effective wavelength scaling for optical antennas. *Phys. Rev. Lett.* **98**, 1–4 (2007).

[69] Adato, R., Yanik, A. A., Wu, C.-H., Shvets, G. & Altug, H. Radiative engineering of plasmon lifetimes in embedded nanoantenna arrays. *Opt. Express* **18**, 4526 (2010).

[70] Neuman, T. *et al.* Importance of Plasmonic Scattering for an Optimal Enhancement of Vibrational Absorption in SEIRA with Linear Metallic Antennas. *J. Phys. Chem. C* **119**, 26652–26662 (2015).

[71] Liberman, V. *et al.* Angle-and polarization-dependent collective excitation of plasmonic nanoarrays for surface enhanced infrared spectroscopy. *Opt. Express* **19**, 11202 (2011).

[72] Vogt, J. *et al.* Chemical Identification of Individual Fine Dust Particles with Resonant Plasmonic Enhancement of Nanoslits in the Infrared. *ACS Photonics* **4**, 560–566 (2017).

[73] Bagheri, S., Giessen, H. & Neubrech, F. Large-Area Antenna-Assisted SEIRA Substrates by Laser Interference Lithography. *Adv. Opt. Mater.* **2**, 1050–1056 (2014).

[74] Bagheri, S. *et al.* Fabrication of Square-Centimeter Plasmonic Nanoantenna Arrays by Femtosecond Direct Laser Writing Lithography: Effects of Collective Excitations on SEIRA Enhancement. *ACS Photonics* **2**, 779–786 (2015).

[75] Aksu, S. *et al.* High-Throughput Nanofabrication of Infrared Plasmonic Nanoantenna Arrays for Vibrational Nanospectroscopy. *Nano Lett.* **10**, 2511–2518 (2010).

[76] D'Andrea, C. *et al.* Optical Nanoantennas for Multiband Spectroscopy. *ACS Nano* **7**, 3522–3531 (2013).

[77] Giannini, V., Francescato, Y., Amrania, H., Phillips, C. C. & Maier, S. A. Fano resonances in nanoscale plasmonic systems: a parameter-free modeling approach. *Nano Lett.* **11**, 2835–40 (2011).

[78] Vogt, J. *et al.* Impact of the plasmonic near- and far-field resonance-energy shift on the enhancement of infrared vibrational signals. *Phys. Chem. Chem. Phys.* **17**, 21169–21175 (2015).

[79] Taflove, A. & Hagness, S. C. *Computational Electrodynamics: The Finite-Difference Time-Domain Method* (Artech: Norwood, MA, 2000).

[80] Oskooi, A. F. *et al.* Meep: A flexible free-software package for electromagnetic simulations by the FDTD method. *Comput. Phys. Commun.* **181**, 687–702 (2010).

[81] Kane Yee. Numerical solution of initial boundary value problems involving maxwell's equations in isotropic media. *IEEE Trans. Antennas Propag.* **14**, 302–307 (1966).

[82] Maß, T. W. W. & Taubner, T. Incident Angle-Tuning of Infrared Antenna Array Resonances for Molecular Sensing. *ACS Photonics* **2**, 1498–1504 (2015).

[83] Koglin, J., Fischer, U. C. & Fuchs, H. Material contrast in scanning near-field optical microscopy at 1–10 nm resolution. *Phys. Rev. B* **55**, 7977–7984 (1997).

[84] Ruiter, A. G. T., Moers, M. H. P., van Hulst, N. F. & de Boer, M. Microfabrication of near-field optical probes. *J. Vac. Sci. Technol. B.* **14**, 10–15 (1996).

[85] Betzig, E. & Trautman, J. K. Near-field optics: microscopy, spectroscopy, and surface modification beyond the diffraction limit. *Science* **257**, 189–95 (1992).

[86] Andrae, P., Song, M., Haggui, M., Fumagalli, P. & Schmid, M. Mapping near-field plasmonic interactions of silver particles with scanning near-field optical microscopy measurements. In Boardman, A. D. & Tsai, D. P. (eds.) *Proc. SPIE*, vol. 9547, 95470E (2015).

[87] Bethe, H. A. Theory of diffraction by small holes. *Phys. Rev.* **66**, 163–182 (1944).

[88] Atkin, J. M., Berweger, S., Jones, A. C. & Raschke, M. B. Nano-optical imaging and spectroscopy of order, phases, and domains in complex solids. *Adv. Phys.* **61**, 745–842 (2012).

[89] Veerman, J. A., Otter, A. M., Kuipers, L. & Van Hulst, N. F. High definition aperture probes for near-field optical microscopy fabricated by focused ion beam milling. *Appl. Phys. Lett.* **72**, 3115–3117 (1998).

[90] Hillenbrand, R. & Keilmann, F. Complex optical constants on a subwavelength scale. *Phys. Rev. Lett.* **85**, 3029–3032 (2000).

[91] Taubner, T., Hillenbrand, R. & Keilmann, F. Performance of visible and mid-infrared scattering-type near-field optical microscopes. *J. Microsc.* **210**, 311–4 (2003).

[92] Knoll, B. & Keilmann, F. Infrared conductivity mapping for nanoelectronics. *Appl. Phys. Lett.* **77**, 3980 (2000).

[93] Schnell, M., Carney, P. S. & Hillenbrand, R. Synthetic optical holography for rapid nanoimaging. *Nat. Commun.* **5**, 3499 (2014).

[94] Huth, F. *et al.* Resonant antenna probes for tip-enhanced infrared near-field microscopy. *Nano Lett.* **13**, 1065–1072 (2013).

[95] Keilmann, F. & Hillenbrand, R. Near-field microscopy by elastic light scattering from a tip. *Philos. Trans. A. Math. Phys. Eng. Sci.* **362**, 787–805 (2004).

[96] Knoll, B. & Keilmann, F. Enhanced dielectric contrast in scattering-type scanning near-field optical microscopy. *Opt. Commun.* **182**, 321–328 (2000).

[97] Ocelic, N., Huber, A. & Hillenbrand, R. Pseudoheterodyne detection for background-free near-field spectroscopy. *Appl. Phys. Lett.* **89**, 101124 (2006).

[98] Moreno, C., Alda, J., Kinzel, E. & Boreman, G. Phase imaging and detection in pseudo-heterodyne scattering scanning near-field optical microscopy measurements. *Appl. Opt.* **56**, 1037–1045 (2017).

[99] Taubner, T., Hillenbrand, R. & Keilmann, F. Nanoscale polymer recognition by spectral signature in scattering infrared near-field microscopy. *Appl. Phys. Lett.* **85**, 5064 (2004).

[100] Huth, F. *et al.* Nano-FTIR absorption spectroscopy of molecular fingerprints at 20 nm spatial resolution. *Nano Lett.* **12**, 3973–8 (2012).

[101] Cvitkovic, a., Ocelic, N. & Hillenbrand, R. Analytical model for quantitative prediction of material contrasts in scattering-type near-field optical microscopy. *Opt. Express* **15**, 8550–65 (2007).

[102] v. Ettingshausen, A. & Nernst, W. Ueber das Auftreten electromotorischer Kräfte in Metallplatten, welche von einem Wärmestrome durchflossen werden und sich im magnetischen Felde befinden. *Ann. der Phys. und Chemie* **265**, 343–347 (1886).

[103] Slachter, A., Bakker, F. L. & van Wees, B. J. Anomalous Nernst and anisotropic magnetoresistive heating in a lateral spin valve. *Phys. Rev. B* **84**, 020412 (2011).

[104] Pfitzner, E. *et al.* Near-field magneto-caloritronic nanoscopy on ferromagnetic nanostructures. *arXiv* (2018).

[105] Häkkinen, H. The gold-sulfur interface at the nanoscale. *Nat. Chem.* **4**, 443–455 (2012).

[106] Miyake, H., Ye, S. & Osawa, M. Electroless deposition of gold thin films on silicon for surface-enhanced infrared spectroelectrochemistry. *Electrochem. commun.* **4**, 973–977 (2002).

[107] Biswas, D. R. Deposition processes for films and coatings. *J. Mater. Sci.* **21**, 2217–2223 (1986).

[108] Reichelt, K. & Jiang, X. The preparation of thin films by physical vapour deposition methods. *Thin Solid Films* **191**, 91–126 (1990).

[109] Weng, D. & Landau, U. Direct Electroplating on Nonconductors. *J. Electrochem. Soc.* **142**, 2598–2604 (1995).

[110] Johnson, P. B. & Christy, R. W. Optical Constants of the Noble Metals. *Phys. Rev. B* **6**, 4370–4379 (1972).

[111] Burger, G. *et al.* High-resolution shadow-mask patterning in deep holes and its application to an electrical wafer feed-through. *Sensor. Actuat. A.-Phys* **54**, 669–673 (1996).

[112] Luecke, H. Crystal Structure of Sensory Rhodopsin II at 2.4 Angstroms: Insights into Color Tuning and Transducer Interaction. *Science* **293**, 1499–1503 (2001).

[113] Pettersen, E. F. *et al.* UCSF Chimera - A visualization system for exploratory research and analysis. *J. Comput. Chem.* **25**, 1605–1612 (2004).

[114] Creager, S. E. & Steiger, C. M. Conformational rigidity in a self-assembled monolayer of 4-mercaptobenzoic acid on gold. *Langmuir* **11**, 1852–1854 (1995).

[115] Rosendahl, S. M. & Burgess, I. J. Electrochemical and infrared spectroscopy studies of 4-mercaptobenzoic acid SAMs on gold surfaces. *Electrochim. Acta* **53**, 6759–6767 (2008).

[116] Liu, Y., Yuan, H., Fales, A. M. & Vo-Dinh, T. PH-sensing nanostar probe using surface-enhanced Raman scattering (SERS): Theoretical and experimental studies. *J. Raman Spectrosc.* **44**, 980–986 (2013).

[117] Li, R. *et al.* Vibrational spectroscopy and density functional theory study of 4-mercaptobenzoic acid. *Spectrochim. Acta. A.* **148**, 369–374 (2015).

[118] Hirayama, J. *et al.* Photocycle of phoborhodopsin from haloalkaliphilic bacterium (Natronobacterium pharaonis) studied by low-temperature spectrophotometry. *Biochemistry* **31**, 2093–2098 (1992).

[119] Hein, M., Wegener, A. A., Engelhard, M. & Siebert, F. Time-Resolved FTIR Studies of Sensory Rhodopsin II (NpSRII) from Natronobacterium pharaonis: Implications for Proton Transport and Receptor Activation. *Biophys. J.* **84**, 1208–1217 (2003).

[120] Radu, I. *et al.* Signal relay from sensory rhodopsin I to the cognate transducer HtrI: Assessing the critical change in hydrogen-bonding between Tyr-210 and Asn-53. *Biophys. Chem.* **150**, 23–28 (2010).

[121] Pfitzner, E., Seki, H., Schlesinger, R., Ataka, K. & Heberle, J. Disc Antenna Enhanced Infrared Spectroscopy: From Self-Assembled Monolayers to Membrane Proteins. *ACS Sensors* **3**, 984–991 (2018).

[122] Engelhard, M., Scharf, B. & Siebert, F. Protonation changes during the photocycle of sensory rhodopsin II from Natronobacterium pharaonis. *FEBS Lett.* **395**, 195–198 (1996).

[123] Moore, H. H. Refractive index of alkaline earth halides and its wavelength and temperature derivatives. *J. Phys. Chem. Ref. Data* **9**, 161–290 (1982).

[124] Binnig, G., Quate, C. F. & Gerber, C. Atomic Force Microscope. *Phys. Rev. Lett.* **56**, 930–933 (1986).

[125] García, R. Dynamic atomic force microscopy methods. *Surf. Sci. Rep.* **47**, 197–301 (2002).

[126] Giessibl, F. J. Advances in atomic force microscopy. *Rev. Mod. Phys.* **75**, 949–983 (2003).

[127] Lieb, M. A. & Meixner, A. J. A high numerical aperture parabolic mirror as imaging device for confocal microscopy. *Opt. Express* **8**, 458 (2001).

[128] Hillenbrand, R., Knoll, B. & Keilmann, F. Pure optical contrast in scattering-type scanning near-field microscopy. *J. Microsc.* **202**, 77–83 (2001).

[129] Jasperson, S. N. & Schnatterly, S. E. An Improved Method for High Reflectivity Ellipsometry Based on a New Polarization Modulation Technique. *Rev. Sci. Instrum.* **40**, 761–767 (1969).

[130] Faist, J. *et al.* Quantum Cascade Laser. *Science* **264**, 553–556 (1994).

[131] Lu, F. & Belkin, M. a. Infrared absorption nano-spectroscopy using sample photoexpansion induced by tunable quantum cascade lasers. *Opt. Express* **19**, 19942 (2011).

[132] Yoxall, E., Schnell, M., Mastel, S. & Hillenbrand, R. Magnitude and phase-resolved infrared vibrational nanospectroscopy with a swept quantum cascade laser. *Opt. Express* **23**, 13358 (2015).

[133] Gilburd, L., Xu, X. G., Bando, Y., Golberg, D. & Walker, G. C. Near-Field Infrared Pump–Probe Imaging of Surface Phonon Coupling in Boron Nitride Nanotubes. *J. Phys. Chem. Lett.* **7**, 289–294 (2016).

[134] Nowak, D. *et al.* Nanoscale chemical imaging by photoinduced force microscopy. *Sci. Adv.* **2**, e1501571–e1501571 (2016).

[135] Giliberti, V. *et al.* Heterogeneity of the Transmembrane Protein Conformation in Purple Membranes Identified by Infrared Nanospectroscopy. *Small* **13**, 1701181 (2017).

[136] Schultz, B.-J., Mohrmann, H., Lorenz-Fonfria, V. A. & Heberle, J. Protein dynamics observed by tunable mid-IR quantum cascade lasers across the time range from 10 ns to 1 s. *Spectrochim. Acta. A.* **188**, 666–674 (2018).

[137] Amarie, S. & Keilmann, F. Broadband-infrared assessment of phonon resonance in scattering-type near-field microscopy. *Phys. Rev. B* **83**, 045404 (2011).

[138] Keilmann, F. & Amarie, S. Mid-infrared frequency comb spanning an octave based on an er fiber laser and difference-frequency generation. *J. Infrared Millim. Te.* **33**, 479–484 (2012).

[139] Gambetta, A. *et al.* Tunable high repetition-rate mid-infrared optical combs from a compact amplified Er-doped fiber oscillator. In *2008 Conf. Lasers Electro-Optics*, vol. 33, 1–2 (IEEE, 2008).

[140] Lozier, R., Bogomolni, R. & Stoeckenius, W. Bacteriorhodopsin: a light-driven proton pump in Halobacterium Halobium. *Biophys. J.* **15**, 955–962 (1975).

[141] Stoeckenius, W. & Bogomolni, R. A. Bacteriorhodopsin and related pigments of halobacteria. *Annu. Rev. Biochem.* **51**, 587–616 (1982).

[142] Oesterhelt, D. & Stoeckenius, W. Rhodopsin-like Protein from the Purple Membrane of Halobacterium halobium. *Nat. New Biol.* **233**, 149–152 (1971).

[143] Müller, D. J., Schabert, F. a., Büldt, G. & Engel, a. Imaging purple membranes in aqueous solutions at sub-nanometer resolution by atomic force microscopy. *Biophys. J.* **68**, 1681–6 (1995).

[144] Rothschild, K. J. & Clark, N. A. Polarized infrared spectroscopy of oriented purple membrane. *Biophys. J.* **25**, 473–487 (1979).

[145] Rothschild, K. J., Zagaeski, M. & Cantore, W. A. Conformational changes of bacteriorhodopsin detected by Fourier transform infrared difference spectroscopy. *Biochem. Biophys. Res. Commun.* **103**, 483–489 (1981).

[146] Mendelsohn, R. Resonance Raman spectroscopy of the photoreceptor-like pigment of halobacterium halobium. *Nature* **243**, 22–24 (1973).

[147] Rousso, I. *et al.* Microsecond atomic force sensing of protein conformational dynamics: implications for the primary light-induced events in bacteriorhodopsin. *Proc. Natl. Acad. Sci. U. S. A.* **94**, 7937–41 (1997).

[148] Oesterhelt, F. Unfolding Pathways of Individual Bacteriorhodopsins. *Science* **288**, 143–146 (2000).

[149] Shibata, M., Yamashita, H., Uchihashi, T., Kandori, H. & Ando, T. High-speed atomic force microscopy shows dynamic molecular processes in photoactivated bacteriorhodopsin. *Nat. Nanotechnol.* **5**, 208–212 (2010).

[150] Müller, D. J. & Engel, A. Atomic force microscopy and spectroscopy of native membrane proteins. *Nat. Protoc.* **2**, 2191–7 (2007).

[151] Oren, A. Microbial life at high salt concentrations: phylogenetic and metabolic diversity. *Saline Systems* **4**, 2 (2008).

[152] Thiaville, A., Rohart, S., Jué, É., Cros, V. & Fert, A. Dynamics of Dzyaloshinskii domain walls in ultrathin magnetic films. *EPL Europhys. Lett.* **100**, 57002 (2012).

[153] Krzysteczko, P., Hu, X., Liebing, N., Sievers, S. & Schumacher, H. W. Domain wall magneto-Seebeck effect. *Phys. Rev. B - Condens. Matter Mater. Phys.* **92**, 1–5 (2015).

[154] Yan, X. M., Contreras, A. M., Koebel, M. M., Liddle, J. A. & Somorjai, G. A. Parallel fabrication of sub-50-nm uniformly sized nanoparticles by deposition through a patterned silicon nitride nanostencil. *Nano Lett.* **5**, 1129–1134 (2005).

[155] Rueden, C. T. *et al.* ImageJ2: ImageJ for the next generation of scientific image data. *BMC Bioinformatics* **18**, 1–26 (2017).

[156] Huck, C. *et al.* Gold nanoantennas on a pedestal for plasmonic enhancement in the infrared. *ACS Photonics* **2**, 497–505 (2015).

[157] Cai, D., Neyer, A., Kuckuk, R. & Heise, H. M. Raman, mid-infrared, near-infrared and ultraviolet–visible spectroscopy of PDMS silicone rubber for characterization of polymer optical waveguide materials. *J. Mol. Struct.* **976**, 274–281 (2010).

[158] Pensa, E. *et al.* Are 4-Mercaptobenzoic Acid Self Assembled Monolayers on Au(111) a Suitable System to Test Adatom Models? *J. Phys. Chem. C* **116**, 25765–25771 (2012).

[159] Srajer, J. *et al.* Double-layered nanoparticle stacks for surface enhanced infrared absorption spectroscopy. *Nanoscale* **6**, 127–31 (2014).

[160] Han, B., Li, Z. & Wandlowski, T. Adsorption and self-assembly of aromatic carboxylic acids on Au/electrolyte interfaces. *Anal. Bioanal. Chem.* **388**, 121–129 (2007).

[161] Brown, L. V. *et al.* Surface-Enhanced Infrared Absorption Using Individual Cross Antennas Tailored to Chemical Moieties. *J. Am. Chem. Soc.* **135**, 3688–3695 (2013).

[162] Huck, C. *et al.* Surface-Enhanced Infrared Spectroscopy Using Nanometer-Sized Gaps. *ACS Nano* **8**, 4908–4914 (2014).

[163] Shih, W.-C., Santos, G. M., Zhao, F., Zenasni, O. & Arnob, M. M. P. Simultaneous Chemical and Refractive Index Sensing in the 1–2.5 μm Near-Infrared Wavelength Range on Nanoporous Gold Disks. *Nano Lett.* **16**, 4641–4647 (2016).

[164] Enders, D., Nagao, T., Nakayama, T. & Aono, M. In situ surface-enhanced infrared absorption spectroscopy for the analysis of the adsorption and desorption process of Au nanoparticles on the SiO_2Si surface. *Langmuir* **23**, 6119–25 (2007).

[165] Rahn, J. & Hallock, R. Antibody binding to antigen-coated substrates studied with surface plasmon oscillations. *Langmuir* **1991**, 650–654 (1995).

[166] Max, J.-J. & Chapados, C. Isotope effects in liquid water by infrared spectroscopy. III. H_2O and D_2O spectra from 6000 to 0 cm^{-1}. *J. Chem. Phys.* **131**, 184505 (2009).

[167] Thiel, P. A. & Madey, T. E. The interaction of water with solid surfaces: Fundamental aspects. *Surf. Sci. Rep.* **7**, 211–385 (1987).

[168] Brown, S. E. *et al.* Substituent Effects and Chiral Discrimination in the Complexation of Benzoic, 4-Methylbenzoic and (Rs)-2-Phenylpropanoic Acids and Their Conjugate Bases by Beta-Cyclodextrin and 6(a)-Amino-6(a)-Deoxy-Beta-Cyclodextrin in Aqueous-Solution - Potentiometric . *J. Chem. Soc. Trans.* **89**, 1035–1040 (1993).

[169] Bain, C. D. & Whitesides, G. M. A study by contact angle of the acid-base behavior of monolayers containing .omega.-mercaptocarboxylic acids adsorbed on gold: an example of reactive spreading. *Langmuir* **5**, 1370–1378 (1989).

[170] Aureau, D., Ozanam, F., Allongue, P. & Chazalviel, J. N. The titration of carboxyl-terminated monolayers revisited: In situ calibrated fourier transform infrared study of well-defined monolayers on silicon. *Langmuir* **24**, 9440–9448 (2008).

[171] Borkovec, M. Origin of 1-pK and 2-pK Models for Ionizable Water-Solid Interfaces. *Langmuir* **13**, 2608–2613 (1997).

[172] Kakiuchi, T., Iida, M., Imabayashi, S.-i. & Niki, K. Double-Layer-Capacitance Titration of Self-Assembled Monolayers of ω-Functionalized Alkanethiols on Au(111) Surface. *Langmuir* **16**, 5397–5401 (2000).

[173] Circular, N B S, Arthur A. Maryott, E. R. S. *Table of Dielectric Constants of Pure Liquids* (U. S. Government Printing Office, 1951).

[174] Smyth, C. P. & Rogers, H. E. The dielectric polarization of liquids. VIII. Acetic and butyric acids. *J. Am. Chem. Soc.* **52**, 1824–1830 (1930).

[175] Colthup, N. B. *et al.* Carbonyl Compounds. *Introd. to Infrared Raman Spectrosc.* 289–325 (1990).

[176] Smith, S. O. *et al.* Vibrational Analysis of the all-trans-Retinal Chromophore in Light-Adapted Bacteriorhodopsin. *J. Am. Chem. Soc.* **109**, 3108–3125 (1987).

[177] Inoue, K., Sasaki, J., Spudich, J. L. & Terazima, M. Laser-induced transient grating analysis of dynamics of interaction between sensory rhodopsin II D75N and the HtrII transducer. *Biophys. J.* **92**, 2028–2040 (2007).

[178] Miller, L. M. & Dumas, P. Chemical imaging of biological tissue with synchrotron infrared light. *BBA - Biomembranes* **1758**, 846–857 (2006).

[179] Bochterle, J., Neubrech, F., Nagao, T. & Pucci, A. Angstrom-scale distance dependence of antenna-enhanced vibrational signals. *ACS Nano* **6**, 10917–10923 (2012).

[180] Blaurock, A. & Stoeckenius, W. Structure of the purple membrane. *Nature* **233**, 152–155 (1971).

[181] Butt, H.-J. Imaging purple membranes dry and in water with the atomic force microscope. *J. Vac. Sci. Technol. B.* **9**, 1193 (1991).

[182] Taubner, T., Keilmann, F. & Hillenbrand, R. Effect of tip modulation on image contrast in scattering-type near-field optical microscopy. *J. Kor. Phys. Soc.* **47**, 213–216 (2005).

[183] Krutokhvostov, R. *et al.* Enhanced resolution in subsurface near-field optical microscopy. *Opt. Express* **20**, 593 (2012).

[184] Mastel, S., Govyadinov, A. A., de Oliveira, T. V. A. G., Amenabar, I. & Hillenbrand, R. Nanoscale-resolved chemical identification of thin organic films using infrared near-field spectroscopy and standard Fourier transform infrared references. *Appl. Phys. Lett.* **106**, 023113 (2015).

[185] Jin, M., Lu, F. & Belkin, M. A. High-sensitivity infrared vibrational nanospectroscopy in water. *Light Sci. Appl.* **6**, e17096 (2017).

[186] Debenham, M. Refractive indices of zinc sulfide in the 0.405–13-μm wavelength range. *Appl. Opt.* **23**, 2238 (1984).

[187] O'Callahan, B. T. *et al.* Broadband infrared vibrational nano-spectroscopy using thermal blackbody radiation. *Opt. Express* **23**, 32063 (2015).

[188] Butt, H. J. *et al.* Imaging cells with the atomic force microscope. *J. Struct. Biol.* **105**, 54–61 (1990).

[189] Stoeckenius, W. A morphological study of halobacterium halobium and its lysis in media of low salt concentration. *J. Cell Biol.* **34**, 365–393 (1967).

[190] Vauclare, P. *et al.* Molecular adaptation and salt stress response of Halobacterium salinarum cells revealed by neutron spectroscopy. *Extremophiles* **19**, 1099–1107 (2015).

[191] Bollschweiler, D., Schaffer, M., Lawrence, C. M. & Engelhardt, H. Cryo-electron microscopy of an extremely halophilic microbe: technical aspects. *Extremophiles* **21**, 393–398 (2017).

[192] Oesterhelt, D. & Stoeckenius, W. Functions of a new photoreceptor membrane. *Proc. Natl. Acad. Sci. U. S. A.* **70**, 2853–7 (1973).

[193] Deckert-Gaudig, T. *et al.* Nanoscale distinction of membrane patches - a TERS study of Halobacterium salinarum. *J. Biophotonics* **5**, 582–591 (2012).

[194] Taubner, T., Keilmann, F. & Hillenbrand, R. Nanoscale-resolved subsurface imaging by scattering-type near-field optical microscopy. *Opt. Express* **13**, 8893 (2005).

[195] Muller, E. A., Pollard, B., Bechtel, H. A., van Blerkom, P. & Raschke, M. B. Infrared Vibrational Nano-Crystallography and -Imaging. *Sci. Adv.* **1601006**, 1–7 (2016).

[196] Dazzi, A. *et al.* AFM-IR: Combining atomic force microscopy and infrared spectroscopy for nanoscale chemical characterization. *Appl. Spectrosc.* **66**, 1365–1384 (2012).

[197] Baldassarre, L. *et al.* Mapping the amide I absorption in single bacteria and mammalian cells with resonant infrared nanospectroscopy. *Nanotechnology* **27**, 075101 (2016).

[198] Kauppinen, J. K., Moffatt, D. J., Mantsch, H. H. & Cameron, D. G. Fourier Self-Deconvolution: A Method for Resolving Intrinsically Overlapped Bands. *Appl. Spectrosc.* **35**, 271–276 (1981).

[199] Ede, S. M., Hafner, L. M. & Fredericks, P. M. Structural Changes in the Cells of Some Bacteria During Population Growth: A Fourier Transform Infrared-Attenuated Total Reflectance Study. *Appl. Spectrosc.* **58**, 317–322 (2004).

[200] Kochan, K. *et al.* In vivo atomic force microscopy–infrared spectroscopy of bacteria. *J. R. Soc. Interface* **15**, 20180115 (2018).

[201] Maquelin, K. *et al.* Vibrational Spectroscopic Studies of Microorganisms. In Chalmers, J. M. (ed.) *Handb. Vib. Spectrosc.* (John Wiley & Sons, Ltd, Chichester, UK, 2006).

[202] Olsen, J. E. & Shimura, F. Infrared spectroscopy of thin silicon dioxide on silicon. *Appl. Phys. Lett.* **53**, 1934–1936 (1988).

[203] Ohwaki, T., Takeda, M. & Takai, Y. Characterization of Silicon Native Oxide Formed in SC-1, H_2O_2 and Wet Ozone Processes. *Jpn. J. Appl. Phys.* **36**, 5507–5513 (1997).

[204] Smith, D. H. & Seshadri, K. S. Infrared spectra of $Mg_2Ca(SO_4)_3$, $MgSO_4$, hexagonal $CaSO_4$, and orthorhombic $CaSO_4$. *Spectrochim. Acta. A.* **55**, 795–805 (1999).

[205] Wieland, F., Dompert, W., Bernhardt, G. & Sumper, M. Halobacterial glycoprotein saccharides contain covalently linked sulphate. *FEBS Lett.* **120**, 110–114 (1980).

[206] Floate, S. *et al.* An in-situ infrared spectroscopic study of the adsorption of citrate on Au(111) electrodes. *J. Electroanal. Chem.* **542**, 67–74 (2003).

[207] Wood, B. R. The importance of hydration and DNA conformation in interpreting infrared spectra of cells and tissues. *Chem. Soc. Rev.* **45**, 1980–1998 (2016).

[208] Lijour, Y., Gentric, E., Deslandes, E. & Guezennec, J. Estimation of the Sulfate Content of Hydrothermal Vent Bacterial Polysaccharides by Fourier Transform Infrared Spectroscopy. *Anal. Biochem.* **220**, 244–248 (1994).

[209] Mescher, M. F., Stroming.Jl & Watson, S. W. Protein and carbohydrate composition of cell envelope of Halobacterium salinarium. *J. Bacteriol.* **120**, 945–954 (1974).

[210] Sara, M. & Sleytr, U. B. S-Layer Proteins. *J. Bacteriol.* **182**, 859–868 (2000).

[211] Bechtel, H. a., Muller, E. a., Olmon, R. L., Martin, M. C. & Raschke, M. B. Ultrabroadband infrared nanospectroscopic imaging. *Proc. Natl. Acad. Sci.* **111**, 7191–7196 (2014).

[212] Wagner, M. *et al.* Ultrabroadband Nanospectroscopy with a Laser-Driven Plasma Source. *ACS Photonics* **5**, 1467–1475 (2018).

[213] Hermann, P. *et al.* Enhancing the sensitivity of nano-FTIR spectroscopy. *Opt. Express* **25**, 16574 (2017).

[214] Dam, J. S., Tidemand-Lichtenberg, P. & Pedersen, C. Room-temperature mid-infrared single-photon spectral imaging. *Nat. Photonics* **6**, 788–793 (2012).

[215] Chen, L. *et al.* Mid-infrared Laser-Induced Fluorescence with Nanosecond Time Resolution Using a Superconducting Nanowire Single-Photon Detector: New Technology for Molecular Science. *Acc. Chem. Res.* **50**, 1400–1409 (2017).

[216] Mancinelli, M. *et al.* Mid-infrared coincidence measurements on twin photons at room temperature. *Nat. Commun.* **8**, 1–8 (2017).

[217] Usui, S. *et al.* Near-Field Imaging of Infrared Nanoantenna Modes Under Oblique Illumination. *J. Phys. Chem. C* **121**, 26000–26006 (2017).

[218] Alonso-González, P. *et al.* Experimental verification of the spectral shift between near- and far-field peak intensities of plasmonic infrared nanoantennas. *Phys. Rev. Lett.* **110**, 1–6 (2013).

[219] García-Etxarri, A., Romero, I., García de Abajo, F. J., Hillenbrand, R. & Aizpurua, J. Influence of the tip in near-field imaging of nanoparticle plasmonic modes: Weak and strong coupling regimes. *Phys. Rev. B* **79**, 125439 (2009).

[220] Dregely, D., Neubrech, F., Duan, H., Vogelgesang, R. & Giessen, H. Vibrational near-field mapping of planar and buried three-dimensional plasmonic nanostructures. *Nat. Commun.* **4**, 2237 (2013).

[221] Aizpurua, J., Taubner, T., García de Abajo, F. J., Brehm, M. & Hillenbrand, R. Substrate-enhanced infrared near-field spectroscopy. *Opt. Express* **16**, 1529 (2008).

[222] Freeman, M. R. Advances in Magnetic Microscopy. *Science* **294**, 1484–1488 (2001).

[223] Bartell, J. M., Ngai, D. H., Leng, Z. & Fuchs, G. D. Towards a table-top microscope for nanoscale magnetic imaging using picosecond thermal gradients. *Nat. Commun.* **6**, 1–7 (2015).

[224] Acremann, Y. *et al.* Time-resolved imaging of spin transfer switching: Beyond the macrospin concept. *Phys. Rev. Lett.* **96**, 2–5 (2006).

[225] Krzysteczko, P. *et al.* Nanoscale thermoelectrical detection of magnetic domain wall propagation. *Phys. Rev. B* **95**, 1–6 (2017).

[226] Tetienne, J. P. *et al.* Nanoscale imaging and control of domain-wall hopping with a nitrogen-vacancy center microscope. *Science* **344**, 1366–1369 (2014).

[227] Karsch, J. C., Bartell, J. M. & Fuchs, G. D. Near-field coupling of gold plasmonic antennas for sub-100 nm magneto-thermal microscopy. *Appl. Phys. Lett.* **2**, 086103 (2017).

[228] Le Ru, E. C. & Etchegoin, P. G. Single-Molecule Surface-Enhanced Raman Spectroscopy. *Annu. Rev. Phys. Chem.* **63**, 65–87 (2012).

[229] Ataka, K., Kottke, T. & Heberle, J. Thinner, smaller, faster: IR techniques to probe the functionality of biological and biomimetic systems. *Angew. Chem. Int. Ed. Engl.* **49**, 5416–24 (2010).

[230] Kästner, B. *et al.* Infrared Nanospectroscopy of Phospholipid and Surfactin Monolayer Domains. *ACS Omega* **3**, 4141–4147 (2018).

[231] Li, P., Wang, T., Böckmann, H. & Taubner, T. Graphene-enhanced infrared near-field microscopy. *Nano Lett.* **14**, 4400–4405 (2014).

[232] Rodrigo, D. *et al.* Mid-infrared plasmonic biosensing with graphene. *Science* **349**, 165–168 (2015).

[233] Chen, S. *et al.* Acoustic Graphene Plasmon Nanoresonators for Field-Enhanced Infrared Molecular Spectroscopy. *ACS Photonics* **4**, 3089–3097 (2017).

[234] Wells, M. *et al.* Interactions between organized, surface-confined monolayers and vapor-phase probe molecules. 9. Structure/reactivity relationship between three surface-confined isomers of mercaptobenzoic acid and vapor-phase decylamine. *Langmuir* **12**, 1989–1996 (1996).

[235] Wu, C. *et al.* Fano-resonant asymmetric metamaterials for ultrasensitive spectroscopy and identification of molecular monolayers. *Nat. Mater.* **11**, 69–75 (2012).

[236] Frisch, M. J. *et al.* Gaussian09 {R}evision {E}.01.

[237] Merrick, J. P., Moran, D. & Radom, L. An evaluation of harmonic vibrational frequency scale factors. *J. Phys. Chem. A* **111**, 11683–11700 (2007).

[238] Harris, F. On the use of windows for harmonic analysis with the discrete Fourier transform. *Proc. IEEE* **66**, 51–83 (1978).

A

Supplementary Information

A.1 Water Vapor Correction for FTIR-Spectra

Atmospheric water vapor strongly affects FTIR-spectra due to the wide spread frequency range of its vibrational-rotational bands. One can correct for these strong bands by subtracting a manually recorded water vapor spectrum. A automated script in Matlab was applied to each spectrum acquired with the FTIR-Microscope. Since the water vapor bands are spectrally much more narrow than vibrational bands of solids one can easily distinguish them from each other in the derivative of a spectrum. The following procedure was applied to find automatically a scaling factor to remove major water vapor contributions:

- calculate derivative of the negative decadic logarithm of the spectrum (S) and a reference water vapor spectrum (R) (assuming a reflectance or transmittance spectrum)
- cut both derivative spectra around the two major water vapor vibrational-rotational bands (2000-1300cm^{-1} and 3300-4100cm^{-1})
- find the minimum of $\underset{k}{min}\left\{\sum_{\nu}[S(\nu)-kR(\nu)]^2\right\}$
- subtract the reference water vapor spectrum from the original spectrum with the found scaling factor k by $S_{corr}=\frac{S}{R^k}$ (the correction factor was retrieved for the subtraction of logarithmic spectra)

This procedure turned out to remove all significant water vapor contributions for the most spectra. Note that the reference water vapor spectrum was recorded with the same spectrometer settings on a otherwise spectrally flat sample (e.g. a flat gold surface).

A.2 Dilution Series of 4-MBA

ATR-FTIR spectra were acquired of 4-MBA dissolved in DMSO at different concentrations to extract the absorbance normalized to the concentration of 4-MBA (Fig. A.1a). 5 μl drops of DMSO concentrations of 4-MBA (1 mM (black) - 1 M (red)) were applied to a single reflection diamond ATR crystal ($\varnothing$ = 2 mm, DuraSampleIR II, PIKE Technologies) mounted in a FTIR spectrometer (Tensor 27, Bruker).

The absorbances per concentration for four different band related to ring modes of 4-MBA (Tab. A.1) were derived by a linear regression to the experimentally derived absorbances at different concentrations (Fig. A.1b).

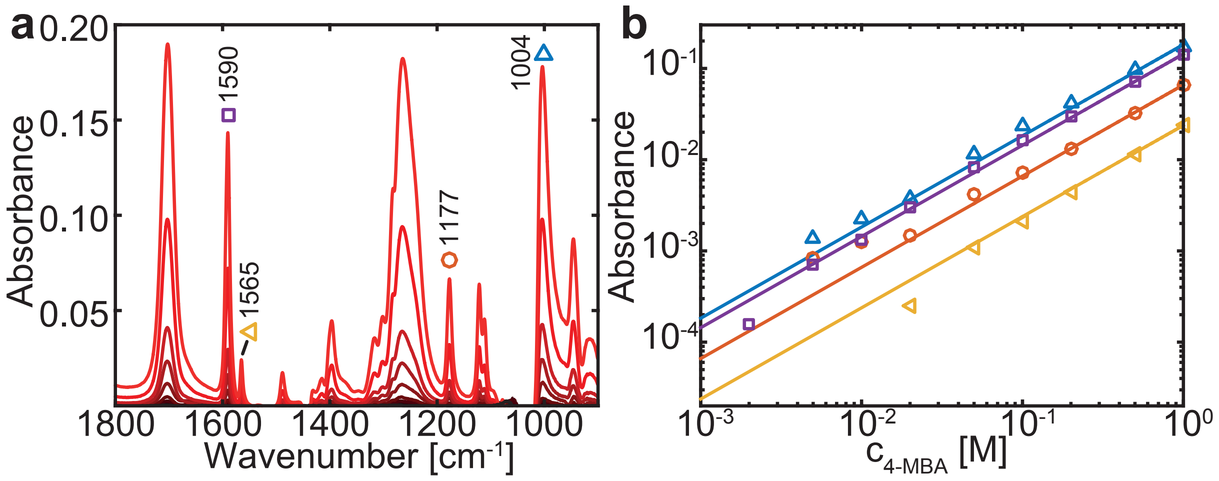

Figure A.1 (a) ATR-FTIR spectra of 4-MBA dissolved in DMSO at concentrations between 1 mM (black) and 1 M (red). **(b)** Absorbances extracted from (a) at the indicated wavenumbers. The solid lines indicate a linear regressions to the data of which the slope is summarized in Tab. A.1.

Vibrational Frequency [cm^{-1}]	**Assignment***	$A^{i}_{\mathbf{ATR}}$ / $c_{\mathbf{ATR}}$ [mol^{-1}]
1590	ring mode (8a)	0.144 ± 0.002
1565	ring mode (8b)	0.024 ± 0.001
1177	δ(C-O) & ring mode (9a)	0.066 ± 0.001
1004	ν(C-H) & ring mode (18)	0.183 ± 0.008

Table A.1 Absorbance normalized to the concentration of 4-MBA in DMSO as inferred from the linear regressions in Fig. A.1b. *Assignment based on ref.[234] Wilson notation for ring modes is used.

A.3 Size of DAAs from Optical Microscopy

The area of the disc antenna arrays (DAAs) was determined from micrographs of Figure 4.1b-d and three more micrographs for better statistics. The micrographs were imported to ImageJ[155] and converted to a binary image. The area of the found individual square shaped DAAs was automatically calculated by ImageJ. The length of one side of each DAA was estimated by the square root of the area.

Array Nr.	**Area** [μm^2]	**Length** [μm]	**Array Nr.**	**Area** [μm^2]	**Length** [μm]
1	8180	90.44	15	7753	88.05
2	8237	90.76	16	7837	88.53
3	8122	90.12	17	7922	89.01
4	8065	89.81	18	8120	90.11
5	8121	90.12	19	8064	89.80
6	7894	88.85	20	7922	89.01
7	8008	89.49	21	7781	88.21
8	8179	90.44	22	8122	90.12
9	7894	88.85	23	7922	89.01
10	7894	88.85	24	8294	91.07
11	7837	88.53	25	8064	89.80
12	7894	88.85	26	7922	89.01
13	7809	88.37	27	8065	89.81
14	7922	89.01	28	7893	88.84
Average	7991± 27	89.39 ± 0.15			

Table A.2 Size determination from the micrographs shown in Fig. 4.1b-d (three more images were included for better statistics). The area was determined with ImageJ.[155] The length of one side was assumed to be the square root of the area.

Array Nr.	**Radius** [μm]	**Projected area** [μm^2]	**Surface area** [μm^2]	**Total area** [μm^2]
1	1.242 ± 0.015	211.8 ± 2.1	212.6 ± 2.1	400
2	1.296 ± 0.016	231.9 ± 2.3	232.7 ± 2.3	400
3	1.371 ± 0.038	251.3 ± 2.5	252.4 ± 2.5	400
4	1.208 ± 0.018	203.9 ± 2.0	205.5 ± 2.1	400
5	1.253 ± 0.016	216.9 ± 2.2	217.7 ± 2.2	400
Average	1.274 ± 0.021	223.2 ± 2.2	224.2 ± 2.2	400

Table A.3 Size estimation from the AFM topography shown in Fig. 4.2b-f. The individual antennas were masked by ImageJ[155] and assumed to be a circular disc. From this area, a disc radius was inferred. Due to dirt on the surfaces, an additional error of 1% was assumed on the masked area.

A.4 Baseline Correction of DAA-FTIR Spectra

It is typical for plasmonic antennas that the resonance frequency is red shifted upon loading the antenna with an external dielectric.[49,235] Figure A.2a shows reflectance spectra of a DAA in dry (black) and while the antennas were immersed in water (red). The red arrow indicates the shift of the antennas resonance due to the increased refractive index of the antennas surrounding from 1 to ∼1.33 (liquid water). Additional to the shift a dip at 1644 cm^{-1} is observed which is attributed to the enhanced δ(OH) of water. The absorbance calculated from the two spectra in (a) leads to a major baseline overlayed with the enhanced δ(OH) (Fig. A.2b). For adsorbtion studies and pH induced difference spectroscopy (Sec. 4.1.2 and Sec. 4.1.3) all spectra were baseline corrected. Each spectrum was smoothed by a moving average filter (width 400 cm^{-1}). The smoothed spectrum was then subtracted from the original one. Figure A.2c shows an absorbance spectrum of a DAA after deposition of a 4-MBA-SAM from an aqueous 4-MBA solution (black) and its smoothed spectrum (red) which serves as baseline.

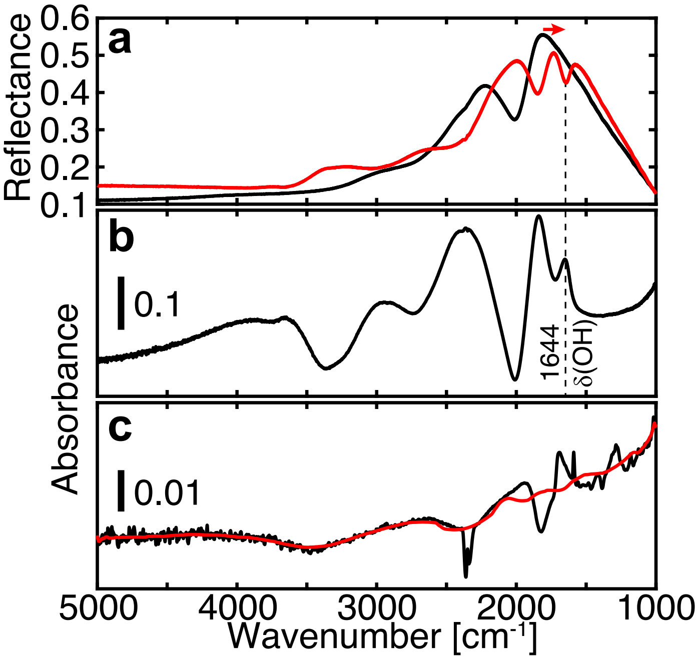

Figure A.2 (a) Reflectance spectra of a DAA in dry (black) and when the antennas are immersed in H_2O (red). The red arrow depicts the shift of the plasmonic resonance. **(b)** The resulting absorbance spectrum of (a). The dashed line marks the bending vibration of of liquid water. **(c)** Absorbance spectrum of the same DAA covered with a 4-MBA-SAM (black) and the baseline (red) obtained by smoothing the black spectrum with a moving average filter (width 400 cm^{-1}).

A.5 Assignment of Vibrational Modes of 4-MBA

Vibrational Frequency [cm^{-1}]			**Assignment***
DAA	conv. SEIRAS	ATR	
1693	1699	1703	ν(C=O)
1587	1585	1590	ring mode (8a)
1558	1554	1565	ring mode (8b)
$\sim$ 1400	$\sim$ 1400	1397	$\nu_S(\mathrm{COO}^-)$
1289†	-	-	δ(C-O-H)‡
1177	1175	1177	δ(C-O) & ring mode (9a)
1015	-	1004	ν(C-H) & ring mode (18)

Table A.4 All spectra were acquired in a DMSO environment. *Assignment based on ref.[234] Wilson notation for ring modes is used. †As seen in pH induced difference spectra (Fig. 4.9a). ‡According to DFT calculations in H_2O.

A.6 DFT Calculations of 4-MBA

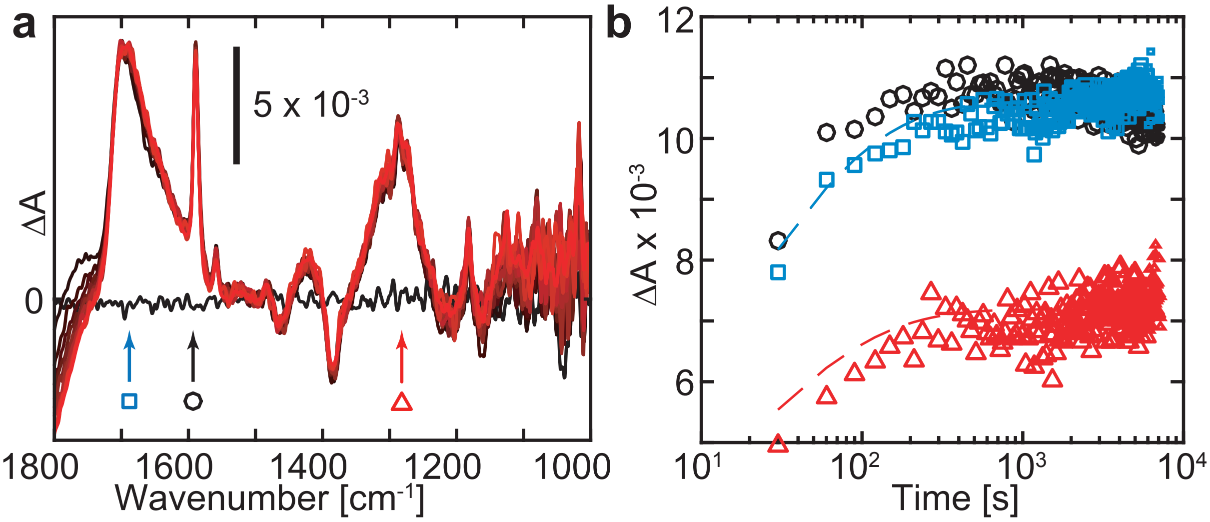

Figure A.3 (a) FTIR spectra after adsorption of 4-MBA in H_2O (red trace) and DMSO (black trace). **(b)** Time evolution of the bands marked in a. The dashed lines indicate a Langmuir adsorption kinetics fitted to the data. Color code follows the same scheme as in a

DFT calculations were performed with Gaussian09.[236] The molecule was set up in gview in the protonated and deprotonated state, respectively. The environment was set to continuous polarizable model (water, $\epsilon = 78.3553$). For both calculations B3LYP/6-311++G** level of theory was used for geometry optimization and calculation of harmonic frequencies.

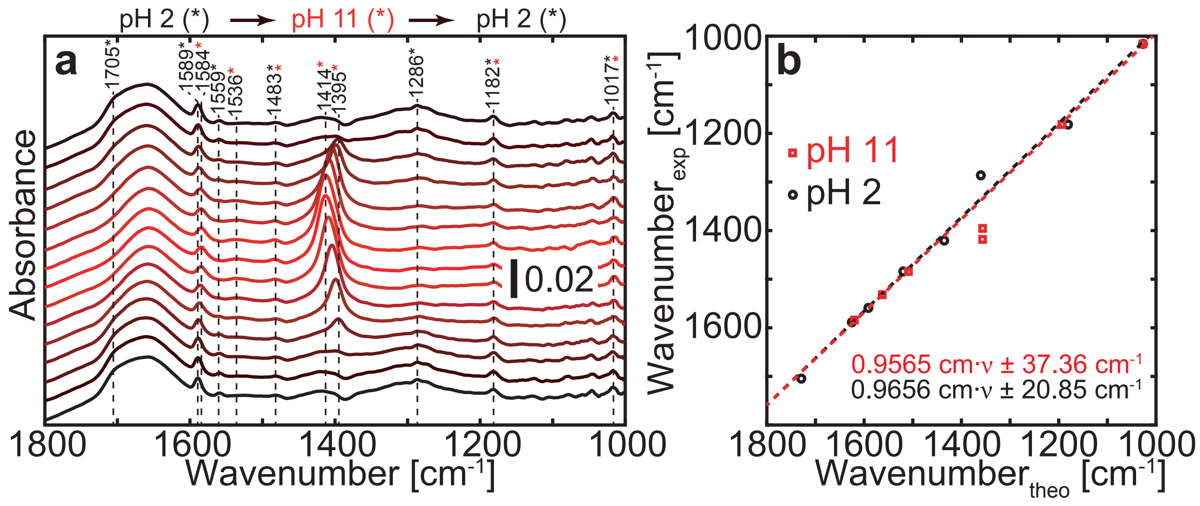

Figure A.4 (a) pH-induced absolute absorbance spectra of 4-MBA adsorbed from an aqueous solution. The experimentally derived frequencies are indicated and attributed to the protonated (*) and deprotonated (*) state. **(b)** Correlation of theoretically predicted and experimentally observed vibrational frequencies in protonated (black) and deprotonated (red) form. The dashed lines indicate linear fits to the correlation plot.

4-MBA was adsorbed from water (Fig. A.3) to acquire absolute pH induced absorbance spectra (Fig. A.4a). Bands attributed to the protonated (*) and deprotonated (*) are indicated along with their experimentally derived frequencies. A linear regression was applied to the correlation of theoretically and experimentally derived frequencies (Fig. A.4b) to determine the shift of the theoretical and experimental vibrational energies. Scaling factors (0.9656 cm^{-1} (protonated) and 0.9565 cm^{-1} (deprotonated)) and offset (20.85 cm^{-1} (protonated) and 37.36 cm^{-1} (deprotonated)) are in a typical range of values found in literature.[237] Frequencies in Figure 4.12 were shifted accordingly.

A.7 4-Term Blackman-Harris Apodization

The 4-term Blackman-Harris apodization is one of the most commonly used ones, especially in FTIR spectroscopy. It was adapted in the following form from ref.[238]

$$w(z) = a_0 - a_1 \cos\left(\frac{2\pi(z - z_{max})}{2z_{max}}\right) + a_2 \cos\left(\frac{4\pi(z - z_{max})}{2z_{max}}\right) - a_3 \cos\left(\frac{6\pi(z - z_{max})}{2z_{max}}\right) \quad \text{(A.1)}$$

with $a_0 = 0.35875$, $a_1 = 0.48829$, $a_2 = 0.14128$ and $a_3 = 0.01168$.

A.8 Full 2π Phase Retrieval in *s*SNOM

In Section 2.3.1 I alluded to the fact that the phase retrieval described via the pseudo-heterodyne modulation in ref.[97] can only yield a phase between 0 and $\pi/2$. Moreno et al. showed an elegant way to retrieve the full 0 to 2π phase by assigning a sign to the heterodyne side-bands (see Fig. 2.12b). They suggest, instead of using the magnitude at the specific side-bands at $n\Omega + mM$ to use the real part of it (see Eqn. 2.29). This is only valid if the complex valued phasors at each side band are completely rotated along the real axis. This could either be done by setting the phase of the demodulators of each side-band to zero in the LIA before acquiring the data or during post-processing. While post-processing it is possible to rotate the complex valued phasors, corresponding to one side-band, onto the real axis. The angle by which the phasors for a side-band in a *s*SNOM map need to be rotated is readily inferred from the covariance of the real part (X) and imaginary part (Y) of the phasors. In this work the covariance was determined line-by-line along the fast axis of the *s*SNOM maps. Those angles were then averaged and the side-band phasors rotated accordingly. This prevents that a drift of the optical phase φ_n (e.g. slow drift in the relative length of the interferometer arms) affect the determined angle. The centering of the phasors is not done, since this is only necessary for strongly resonant structures on a weakly scattering substrate (e.g. plasmonic structures on a glass substrate).[98]

Figure A.5a shows the complex valued phasors demodulated at the first (m = 1, black) and second (m = 2, red) side-bands around the third harmonic of the tip frequency (n = 3). The data corresponds to the *s*SNOM map shown in Fig. 4.24a-d. X denotes the real part whereas Y stands for the imaginary part of the respective side-band. The point clouds are slightly rotated out of the real axis. The phasors after the described correction procedure is shown in Figure A.5b. Apparently, the cloud is rotated completely onto the real axis. Only spreads the points slightly into the complex plane. Figure A.5c,d show the *s*SNOM amplitude s_3 and phase φ_3 maps recovered from the raw data using the algorithm of Ocelic et al.[97] whereas Figure A.5e,f show the maps recovered with the described full phase retrieval. It can clearly be seen that the phase can only be correctly recovered in Figure A.5c for areas on the cell which show strong phase contrasts (big central salt crystal). Otherwise, neither the phase contrast on the cell nor the amplitude contrast throughout the maps d,f are affected by the full phase retrieval.

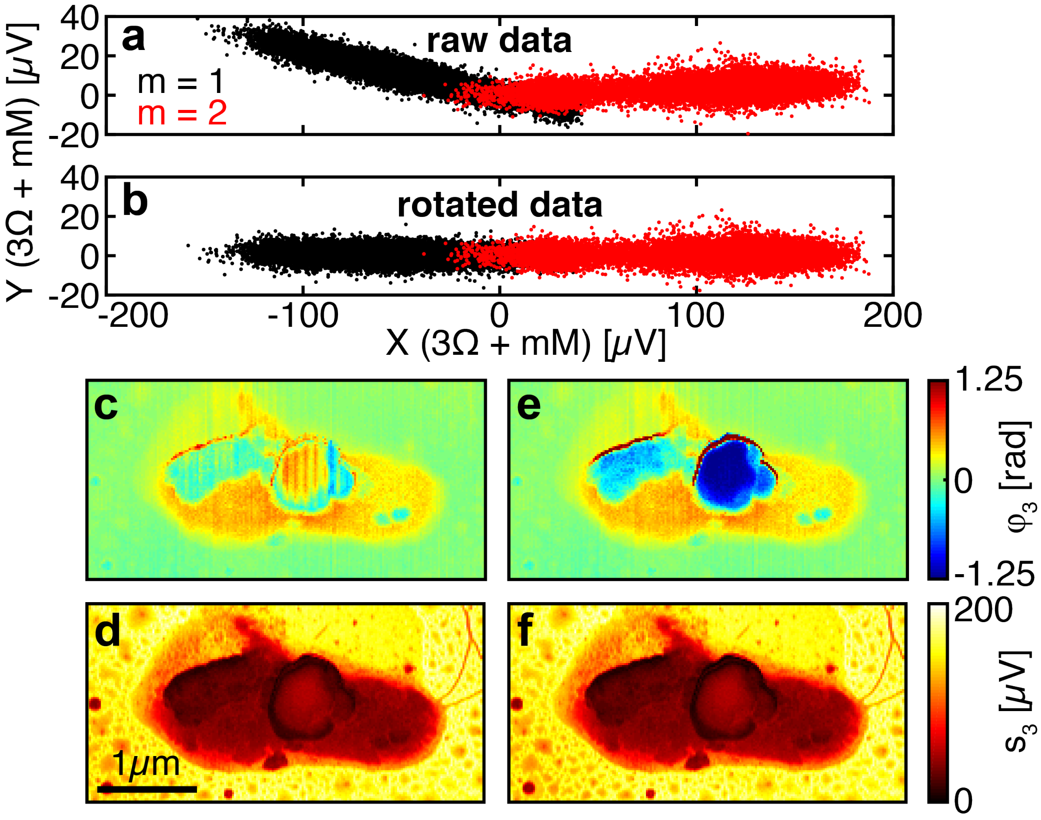

Figure A.5 (a) Raw complex valued phasors demodulated at the first side-band (m = 1, n = 3, black) and second side-band (m = 2, n = 3, red) of the *s*SNOM map shown in Fig. 4.24a-d. **(b)** Rotated side-bands as described in this section. **(c,d)** *s*SNOM amplitude s_3 and phase φ_3 maps of the raw data. **(e,f)** *s*SNOM amplitude s_3 and phase φ_3 maps of the rotated data.

A.9 Line-by-Line Phase Leveling of *s*SNOM Data

Phase drifts, induced by thermally driven relative motion of the interferometer arms, was reduced by the following procedure: A mean phase was obtained line-by-line for the pixels associated with the TSAu substrate. Since the substrate typically showed a good contrast in the amplitude maps, those pixels were assigned to the substrate, for which the amplitude was higher than 80 % of the maximal value in one specific line ($s_n > 0.8 \cdot \max\{s_n\}$). The mean phase was then calculated for theses pixels and subtracted from the phase in the corresponding line.

A.10 Comprehensive Overview of *s*SNOM Maps of *H. salinara*

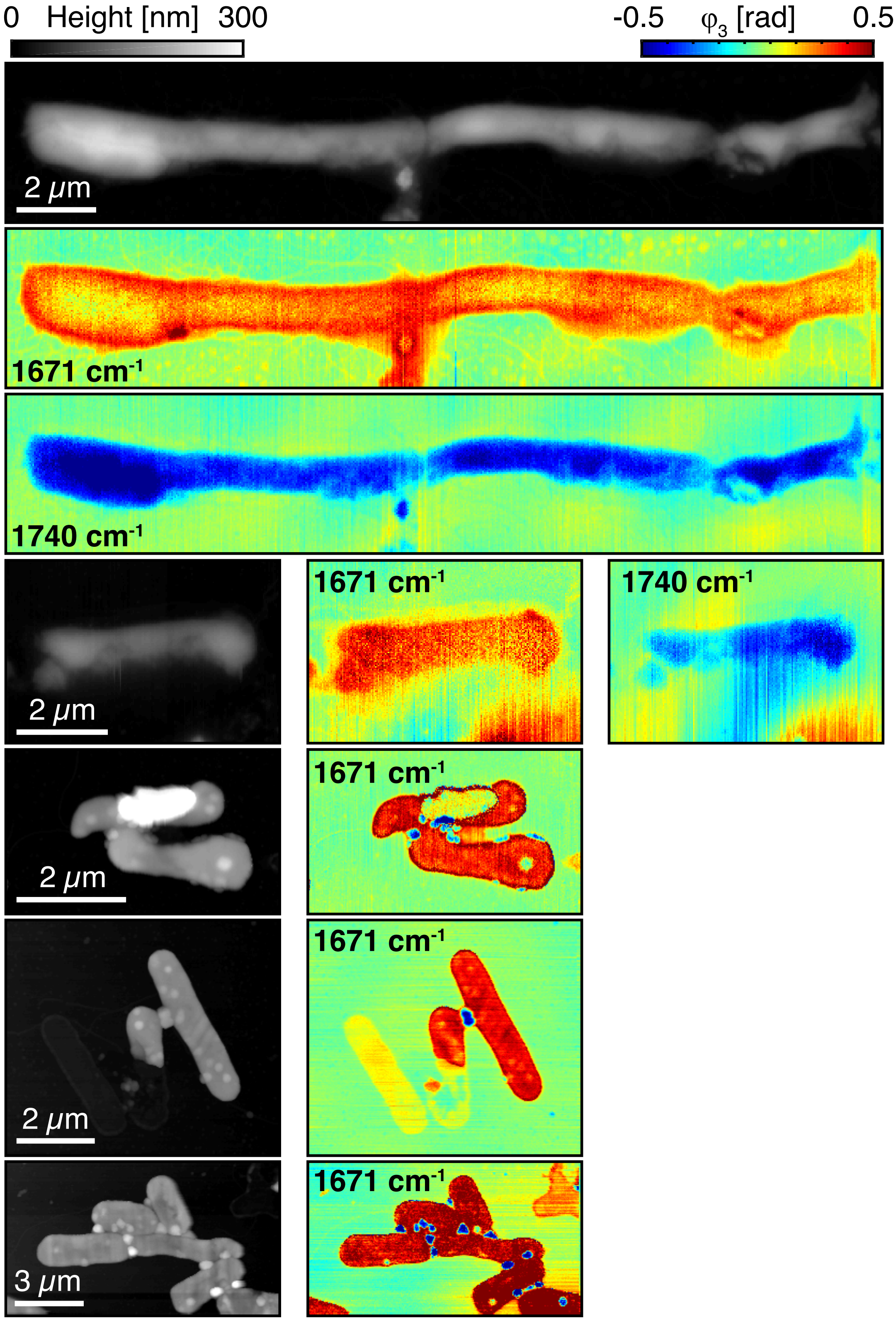

Figure A.6 *s*SNOM maps of *H. salinara* of the strain L33. Topography and near-field phase φ_3 maps recorded with the QCL tuned to 1670 cm^{-1} and 1740 cm^{-1} (n = 3). The full phase retrieval was used (see Sec. 2.3.1).[98] The color scale of the topography and phase is kept constant throughout the figure, respectively.

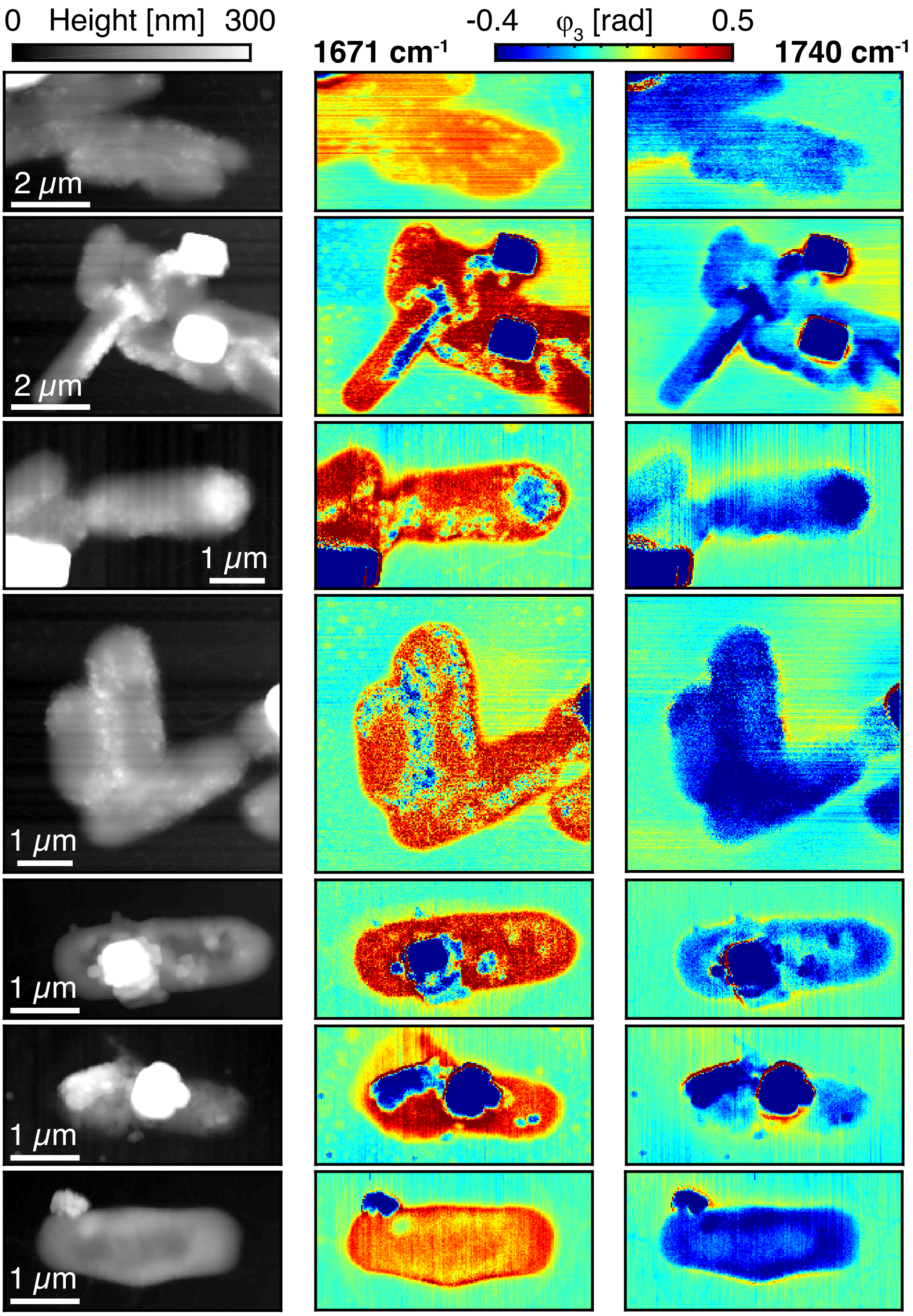

Figure A.7 *s*SNOM maps of *H. salinara* of the strain S9. Topography and near-field phase φ_3 maps recorded with the QCL tuned to 1670 cm^{-1} and 1740 cm^{-1} (n = 3). The full phase retrieval was used (see Sec. 2.3.1).[98] The color scale of the topography and phase is kept constant throughout the figure, respectively.

A.11 Full Range ATR-FTIR Spectra of *H. salinara*

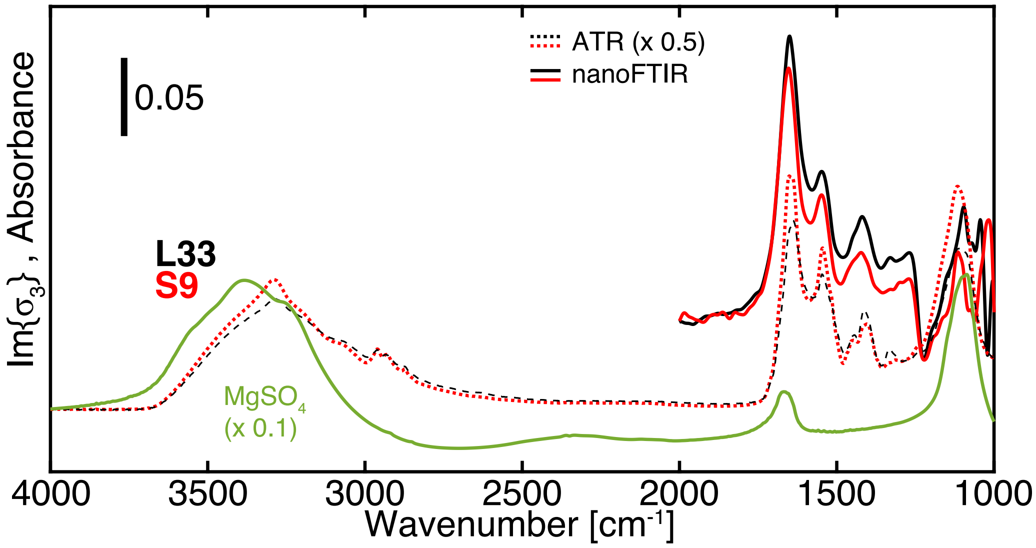

Figure A.8 Full mid-IR ATR-FTIR spectra of L33 (black dashed) and S9 (red dashed) *H. salinara* and KBr spectrum of $MgSO_4$ (green) along with nano-FTIR spectra of the averaged homogeneous spectra acquired on L33 (black solid) and S9 (red solid) *H. salinara*.

A.12 Correlation of Height and Near-Field Phase

The near-field phase φ_3 of the *H. salinarum* shown in Figure 4.24 (depicted for comparison again in Fig. A.9a-d) was correlated with its topographic height (Fig. A.9e). The correlation of φ_3 recorded at 1671 cm^{-1} (red) and 1740 cm^{-1} (blue) was binned into a two dimensional histogram. The intensity of the respective colors indicates $\log(n + 1)$ where n is the number of pixels in one bin. A false-color map (inset in Fig. A.9e) indicates different regions classified according to their height (vertical sections). The phase-height correlation is identical for pixels acquired on Si. The phase increases with height when the QCL is tuned to 1671 cm^{-1} (amide I) and approaches a maximal value. In contrast to that, it decreases steadily with height when the QCL is tuned to 1740 cm^{-1} on the archeon. In the next section (low salt) the phase at 1671 cm^{-1} approaches the phase recorded off-resonance (1740 cm^{-1}). The saturation-like behavior in the section 'halobacterium' and 'low salt' of the on-resonance phase is in agreement with the in z-direction exponentially decaying penetration the sSNOMs. In the highest section the phase-height correlation at both wavenumbers identically decreases linearly. Interestingly, the linear decrease in the 'high salt' section is offset from the one in lower sections. However, the origin of this additional phase offset on the highest section is unclear. The approximately linear decrease of the off-resonance phase might resemble a phase shift introduced by indirect illumination paths as discussed in the main text in Section 4.2.2 and in ref.[132] From the correlation it can be clearly inferred that the near-field phase maps are affected by the topography for samples exhibiting height differences on the order of $\lambda/20$. This demonstrates the great advantage of broadband spectrally resolved nano-FTIR since spectral features (e.g. amide I) can be identified atop of a constant phase offset.

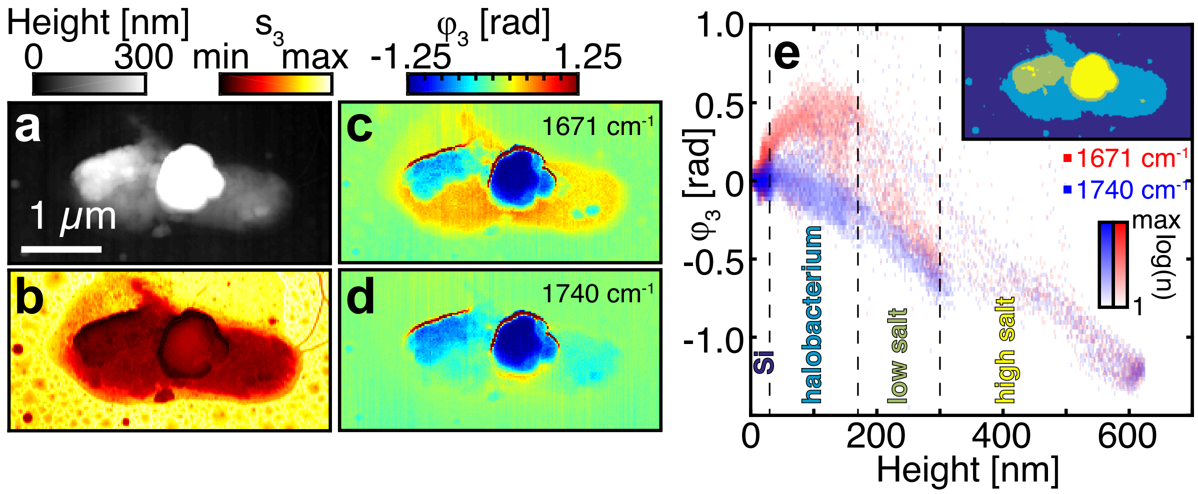

Figure A.9 **(a)** Topography **(b)** near-field amplitude s_3 and **(c,d)** near-field phase maps φ_3 of an individual *H. salinarum* (S9, see Fig. 4.24). **(e)** Histogram of the correlation of the near-field phase recorded at 1671 cm^{-1} (red) and 1740 cm^{-1} (blue) with the topographic height. The intensity of the color indicates the number n of pixels found in one bin (displayed logarithmically). A false-color image (inset) displays sections classified according to the height of the *H. salinarum*.

A.13 Si Reference in Near-Field Spectra

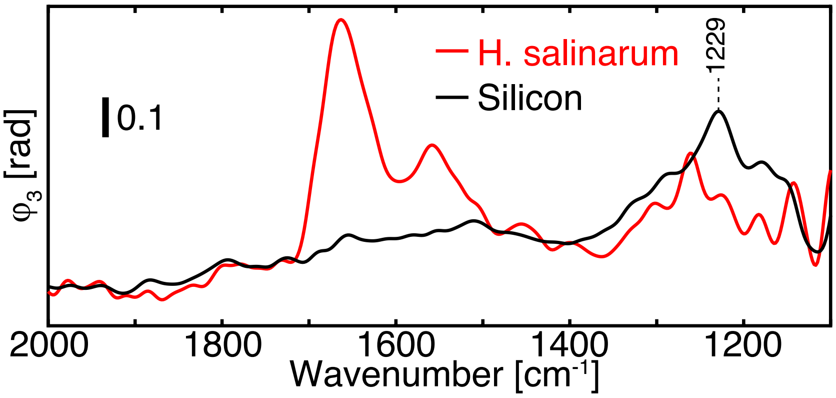

Figure A.10 Unreferenced phase spectra φ_3 taken on the silicon substrate (black trace) and on *H. salinarum* (red trace). The 1229 cm^{-1} band of SiO$_2$ appears only in the silicon spectrum but not in the *H. salinarum* spectrum. Referencing, thus, yields the negative band seen in the spectra in Section 4.2.2.

A.14 Near-Field Maps of Resonant Plasmonic Antennas

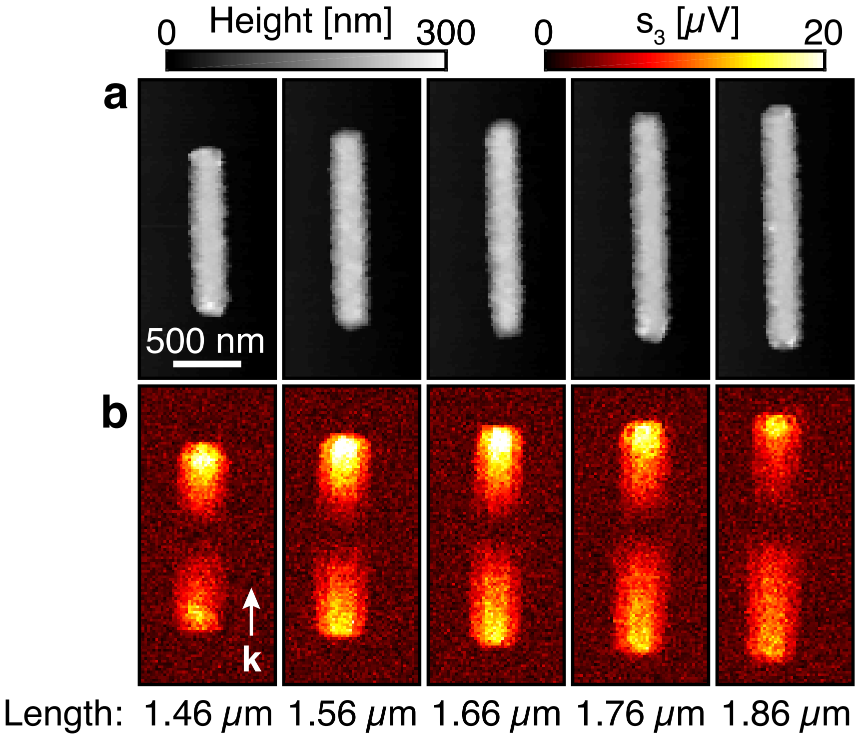

Figure A.11 (a) Topography and **(b)** homodyne near-field amplitude (s_3) maps of antennas of length 1.46 μm - 1.86 μm recorded with a broadband source. The color scale is kept constant throughout all antenna lengths. The projection of **k** of the incident light is indicated by the white arrow. The nominal angle of incidence was 30° out of the plane.

A.15 Linear Scaling of Resonance Wavelength of Linear Antennas

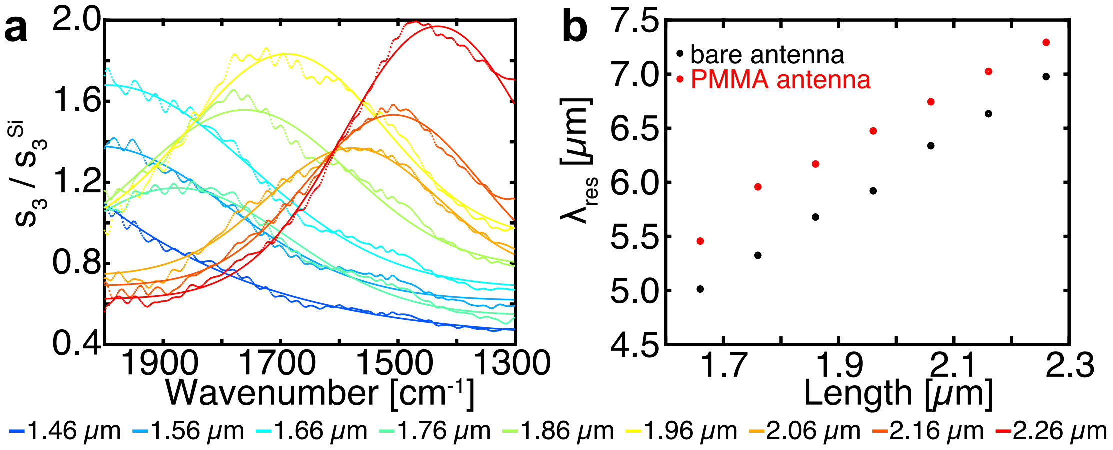

Figure A.12 (a) Gaussian fits to the bare antenna nano-FTIR amplitude spectra from Fig. 4.26a. **(b)** Extracted resonance wavelengths λ_{res} of the bare (black) and PMMA coated (red) antennas. The errorbars (95% confidence interval from fit) are about the size of the symbols.

A.16 Magnetic Nanostructure with and without Illumination

Figure A.13 displays cross-sections of the EMF (red and black traces) of the magnetic device with a DW present along with topography cross-sections (blue traces). Figure A.13a shows the cross-sections on the left side of the notch ($M^{\uparrow}$) whereas b shows the cross-sections on the right side of the notch ($M^{\downarrow}$). The cross-section was acquired with the QCL blocked (black traces) and opened (red traces). The traces (red) in which the light reached the tip show the typical gradient along the y_0-direction and the superimposed edge artifacts. Furthermore, the typical inversion of the gradient is observed when the magnetization switches from $M^{\uparrow}$ (Fig. A.13a, red trace) to $M^{\downarrow}$ (Fig. A.13b, red trace). When the QCL is blocked by a paper card (black trace) the gradient in the cross-sections vanishes and only the edge artifacts remain. This strongly suggests that the observed contrast in Figures 4.29 and 4.30 is of magneto-caloritronic origin.

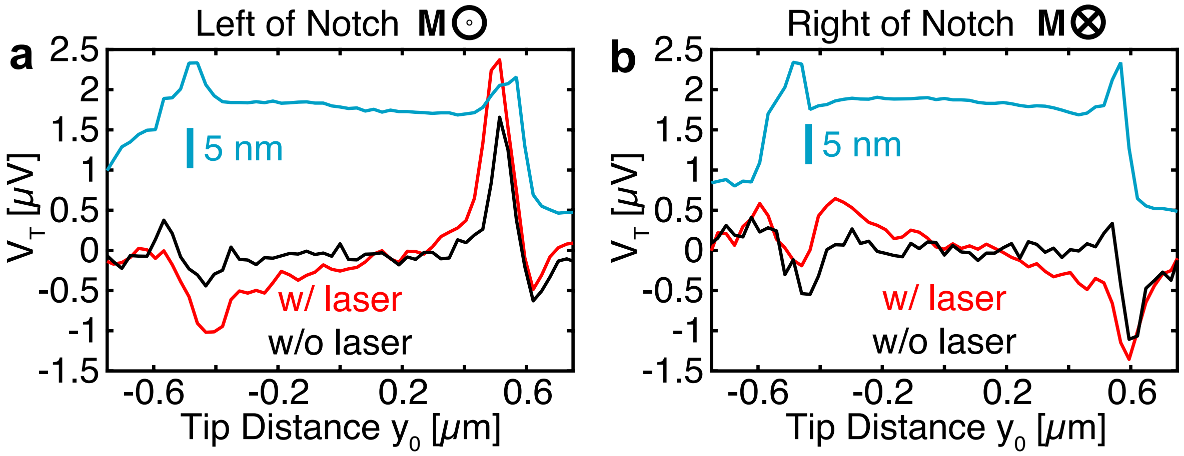

Figure A.13 EMF cross sections of the magnetic device with the laser blocked (black) and open (red), left of the notch ($M^{\uparrow}$) **(a)** and right of the notch **(b)** ($M^{\downarrow}$) when a DW is present. The topography cross-section is indicate by the blue line.

B

Appendix

Publications originating from experiments described in this thesis

[1] Pfitzner, E., Seki, H., Schlesinger, R., Ataka, K., & Heberle, J. Disc Antenna Enhanced Infrared Spectroscopy: From Self-Assembled Monolayers to Membrane Proteins. ACS Sensors, **2018**, 3, 984–991, DOI: 10.1021/acssensors.8b00139

[2] Pfitzner, E., Hu, X., Schuhmacher, H. W., Hoehl, A., Venkateshvaran, D., Cubukcu, M., Liao, J.-W., Auffret, S., Heberle, J., Wunderlich, J. & Kästner, B. Near-field magneto-caloritronic nanoscopy on ferromagnetic nanostructures. AIP Adv., **2018**, *submitted* (preprint available at ArXiv ID: 1808.10767)

Selbstständigkeitserklärung

Hiermit versichere ich für diese Dissertation mit dem Titel

Surface and Tip-Enhanced Infrared Spectroscopy in Life Science: Approaching the Single-Molecule Limit

alle Hilfsmittel und Hilfen angegeben zu haben und auf dieser Grundlage die Arbeit selbstständig verfasst zu haben. Ich versichere, dass diese Arbeit nicht schon einmal in einem früheren Promotionsverfahren angenommen oder als ungenügend beurteilt wurde.

Berlin, den 8.11.2018

Emanuel Pfitzner

Zusammenfassung

Infrarot (IR) Spektroskopie ist eine der leistungsfähigsten Methoden in den Lebenswissenschaften. Sie liefert auf nicht-invasive Weise Informationen über molekulare Struktur und Funktion. Jedoch reicht die Sensitivität und Ortsauflösung nicht aus, um einzelne Biomoleküle zu untersuchen. Oberflächen- und Spitzenverstärkte Spektroskopie nutzen die nanoskopische Lokalisierung von sowohl dem Messlicht als auch der Probe, um diese Defizite auszugleichen.Beugungsbegrenzte oberflächenverstärkte Methoden bieten hohe Verstärkungsfaktoren für die Spektroskopie an Ensembles von Biomolekülen, selbst in wässrigen Umgebungen, haben aber den Nachteil hoher Herstellungskosten. Im Gegensatz dazu bieten spitzenverstärkte Methoden noch höhere Sensitivitäten bis zu wenigen Hundert Molekülen sowie eine Ortsauflösung im Nanometerbereich, sind aber bis jetzt relativ langsam und benötigen getrocknete Proben.

In dieser Arbeit stelle ich diverse Ansätze vor, um Einzelmolekül-IR-Spektroskopie zu realisieren. Eine kosteneffiziente und reproduzierbare Methode für die Herstellung von Substraten für oberflächenverstärkte IR-Spektroskopie wurde entwickelt. Die resonanten scheibenförmigen Antennen ermöglichen die mikrospektroskopische Charakterisierung von sub-fmol ($< 10^{-15}$ mol entsprechend $\sim 10^9$ Molekülen) eines funktionellen Membranproteins. Darüberhinaus sind die vorgestellten Substrate kompatibel mit den Messbedingungen biologischer Proben. Oberflächenverstärkten Methoden mangelt es jedoch an Ortsauflösung, um einzelne Moleküle zu lokalisieren und zu detektieren.

Daher habe ich ein streuungsbasiertes optisches Rasternahfeldmikroskop (*s*SNOM) für nanoskopische IR-Bildgebung und -Spektroskopie entworfen und realisiert. Eine laterale Ortsauflösung von 30 nm wurde an proteinbeladenen Membranen erzielt und damit eine Sensitivität jenseits von zmol ($< 10^{-21}$ mol entsprechend ~ 600 Molekülen) erreicht. Die Aufnahmegeschwindigkeit wurde im Vergleich zu konventionellen Aufbauten um einen Faktor 20 verbessert, was zeitaufgelöste Studien an Biomolekülen im μs-Bereich ermöglicht. Die Kombination von plasmonischen Substraten und *s*SNOM führte zu keiner weiteren Verbesserung der Sensitivität und wirft die Frage nach alternativen Strategien auf.

Als Anwendung in den Lebenswissenschaften wurde die hier vorgestellte Nanobildgebung und -spektroskopie mittels *s*SNOM auf ganze Zellen des Archaeons *Halobacterium salinarum* (*H. salinarum*) angewandt. Dabei konnte eine homogene Proteinverteilung innerhalb der Zellwand nachgewiesen werden. Desweiteren konnte ich durch die Beleuchtung der Spitze in Totalreflexionsgeometrie zeigen, dass *s*SNOM in wässrigen Umgebungen möglich ist. Diese Experimente bilden die Grundlage für die Analyse von komplexeren Membransystemen in lebenden Zellen.

Das aufgebaute *s*SNOM wurde modifiziert, um die lokal erzeugte Wärme mittels des anomalen Nernst-Effekts auszulesen und dadurch die Bandbreite von spitzenverstärkten Methoden zu erweitern. Die magnetischen Domänen in einem ferromagnetischen Mikrobarren wurden beispielhaft lokalisiert. Des Weiteren kann diese Methode nicht nur auf antiferromagnetische Systeme angewendet werden, sondern bietet auch vielseitige Möglichkeiten für Nahfeld-IR-Spektroskopie.

Die hier vorgestellten Resultate bereiten den Weg für IR-Spektroskopie an einzelnen Biomolekülen durch die Kombination von Oberflächen-, Spitzenverstärkung und neuartigen spektroskopischen Detektionsmethoden.

Acknowledgements

Many persons essentially supported me during the experiments leading to this manuscript. First, I would like to thank Prof. Dr. Joachim Heberle for giving me the opportunity to perform a huge variety of experiments in his group. I appreciate his constant financial support and inventiveness in the past five years without which all the presented thoughts and experiments would not have come reality. Major support I got during my thesis from all people of the group 'Experimental Molecular Biophysics'. I would like to particularly express my gratitude to Dr. Kenichi Ataka for mentoring me, Dr. Hendrik Mohrmann and Dr. Moritz Senger for creative discussions and best critics, Bernd Schulz for solutions to electronic issues and Katerina Kanevche for her creative support during building the *s*SNOM and nanoFTIR setup. The most important person, though, was my lovely friend Julia. Without her constant care and extraordinary patience I would never got to finish this thesis in Berlin. There are several more persons I would like to thank for fruitful collaborations:

- Hirofumi Seki – was involved in conducting experiments and discussing results of the disc antenna arrays.
- Fucsia Crea – supplied the MACH-*Np*SRII sample at outstanding purity and helped interpreting the resulting spectra.
- Kirsten Hoffmann, Dorothea Heinrich and Dr. Ramona Schlesinger – all three provided highly pure samples of purple membrane and *Halobacterium salinarum* and helped in understanding the experimental results.
- Prof. Dr. Paul Fumagalli – for initial ideas and knowledge about near-field microscopy.
- Dr. Bernd Kästner and Dr. Joerg Wunderlich – both provided the ferromagnetic devices, helped interpreting the anomalous Nernst effect experiments and supplied theoretical support.
- Dr. Marta Autore, Dr. Saül Vélez and Prof. Dr. Rainer Hillenbrand – provided the rod-like antennas and collaborated in data acquisition and interpretation.
- Dr. Moritz Senger, Katerina Kanevche, David Ehrenberg, Federico Baserga, Dr. Hendrik Mohrmann, Dr. Sven T. Stripp – for proofreading my manuscript.